LANCASTER UNIVERSITY

Demagnetisation of Solid ^{3}He

&

Supercritical Superflow

by

Jakub Vonka

A thesis submitted in partial fulfillment for the

degree of Doctor of Philosophy

in the

Faculty of Science and Technology

Physics Department

February 2018

Declaration of Authorship

I declare that the work contained within this thesis is the authors own work and has not been submitted for the award of a higher degree at any other university.

The experiments described in this work are a colaborative effort of the Lancaster University Ultra Low Temperature Group. The author has designed and built the aerogel demagnetisation experiment and participated in the diagnostics of the encountered heating problem. The author also daily participated in running the Floppy Wire experiment, including data analysis.

Abstract

This work describes the efforts with two ultra low temperature experiments with superfluid ^{3}He as medium of interest. The experiments are mostly performed at temperatures below 200 µK, in the regime where superfluid quasiparticle excitations are ballistic.

Recently, a novel experimental tool has been built in Lancaster - a superconducting goalpost-shaped wire that can be moved trough the superfluid in oscillatory as well as in uniform linear motion. An object moving with high enough velocity that the excitation spectrum becomes gapless can create excitations at no energy cost and initiate the breakdown of the condensate - this limit is the well-known Landau velocity. In superfluid ^{3}He, flow around an oscillating body displays a very clear onset of such dissipation. However, with this experiment it was found that for a uniform linear motion there is no discontinuity whatsoever in the dissipation as the Landau critical velocity is passed and exceeded, entering a supercritical flow regime. This regime allows for studying the dynamics of the Andreev bound states on the surface of the wire. This work presents a recent experimental estimation of the relaxation time of the bound states and a description of the relaxation mechanism.

Next, the work describes the design and initial testing of a new experiment. Here a layer of solid ^{3}He formed on the surface of a large aerogel sample submersed in superfluid ^{3}He will be cooled down to below 100 µK in a double nuclear demagnetisation process. NMR on the solid ^{3}He will be used to search for a possible magnetic phase transition as well as to study superfluid ^{3}He virtually free of quasiparticle excitations. The work reports progress to the present state of the experiment and discusses setbacks due to a large unexpected heating which appeared during the demagnetisation of the copper stage.

Acknowledgements

Experimental low temperature physics is by its very nature a group effort and I wish to thank every member of the Lancaster Ultra Low Temperature group for their contribution.

First and foremost I would like to thank Dima Zmeev with whom I shared countless hours watching noisy lines that almost always did not do what we were hoping for, especially during our demagnetisation attemps. You have been not only an imense help but also great friend in lab as well as outside it, on the fells or in the pub.

Big thank you goes to my supervisors for guiding the work in the right direction and carefully proof-reading this thesis. First, to Shaun Fisher for his help during the initial stage of the aerogel demagnetisation experiment - you are solely missed. Next to Ian Bradley for his great advice and consulations when designing and building the experimental cell. Lastly, to Rich Haley for his insights on the data obtained with the Floppy Wire experiment, at all times positive guidance and motivation.

My thank you also goes to Tony Guénault for always being around to explain my often silly questions in such a simple manner that even I could most of the time eventually get it. Many thanks go to Roch Schanen especially for writing truly beautiful code that made the automatisation of a great part of our measurements possible, saving us many dull hours closed inside the Faraday cage. To you and Malcom Poole go my thanks for the tobacco I took from you during the long evenings in the lab and for many engaging conversations. Thanks also goes to George Pickett for his beautiful stylish figures and the trips to show us local history and, in the case of the gypsy fair, some culture too. I also wish to thank Maros, Matt, Andy and Theo for many very useful consultations and generally making the lab a much better place to work in. Big thanks to Alan Ward and Martin Stokes for their precise work when machining all the necessary pieces for the aerogel cell and always having a good joke ready.

My thanks go to other friends outside of the lab for making the time spent in Lancaster much nicer. Malen, Mike, Veronica, Ola, Max, Nabil, Natalie, Sergey, Oliver, Cici and Dimitris to name a few - we have done

many cool things together and I am grateful I have met you all. Also thanks to squash and tennis buddies for keeping me fit during this period.

One huge thanks goes to Valentina, who immediately became a friend for life. I honestly can not imagine how these four years would look like without you and to you also goes credits for introducing me to Moniek.

Moniek, thank you for being here for me all this time and changing me for the better. We have done so much together despite a long distance apart and I can not wait for what is awaiting us next in Switzerland.

Lastly, I want to thank my parents Dagmar and Peter for their loving and truly unconditional support.

Contents

List of Figures

List of Tables

Abbreviations

AC	**A**lternating **C**urrent
BEC	**B**ose-**E**instein **C**ondensate
DAQ	**D**ata **Acq**uisition
DC	**D**irect **C**urrent
DLCA	**D**iffusion-**L**imited **C**luster **A**ggregation
emf	Electro**m**otive **F**orce
HWD	**H**eight times **W**idth over **D**rive
ICTA	**I**nner **C**ell **TA**ntalum vibrating wire
NMR	**N**uclear **M**agnetic **R**esonance
OCTA	**O**uter **C**ell **TA**ntalum vibrating wire
QTF	**Q**uartz **T**uning **F**ork
VWR	**V**ibrating **W**ire **R**esonator

Chapter 1

Introduction

This work describes two experiments with superfluid ^{3}He at temperatures below 200 µK, well in the ballistic limit of thermal excitations. The experiments were performed within the Ultra Low Temperature Group of Lancaster University, using its extensive facilities of dilution refrigerators with nuclear demagnetisation cooling.

Initially, the aim of this work was to design and run a new experiment allowing for reaching ultra low temperatures by demagnetisation of solid ^{3}He formed on the surfaces of aerogel. The new experiment was designed, built and cooled down despite several setbacks such as a leaky dewar vessel, leaky inner vacuum space of the dilution unit and even a refurbishment of the laboratory. Unfortunately, the initial conditions for the demagnetisation of solid ^{3}He have not yet been reached. A massive source of heating during the demagnetisation of copper was encountered, which prevented us from sustaining superfluid inside the experimental volume. Despite large efforts with diagnostics, the origin of the heating has not been found even after the post-mortem of an irreversible cell disassembly. At this point, a series of time consuming tests of the individual parts would be necessary to identify the source of heating. Due to the limited time available, we shifted our attention to another experiment that utilises a novel oscillatory device named the Floppy Wire. In addition to oscillatory (AC) motion, this device allows one to study steady linear (DC) motion within superfluid ^{3}He

for the fist time. Prior to our efforts, a study of the Floppy Wire under DC motion led to the striking discovery of anomalously low dissipation at velocities exceeding the Landau critical velocity. Here we describe further measurements and validation of our model of the dissipation process.

1.1 Floppy Wire experiment

More than 60 years ago, L. D. Landau showed that below a certain velocity of superfluid flow, now known as the Landau critical velocity v_L, no excitations are created and the flow has no viscosity [1]. Below v_L, the excitations can not escape to the bulk due to an energy barrier. This energy barrier is reduced with velocity and reaches zero at v_L. Landau velocity should thus mark an onset of strong dissipation as the excitations can suddenly be created at no energy cost.

The value $v_L = 50\,\mathrm{mm\,s^{-1}}$ predicted for ^{4}He was confirmed experimentally with an exceptional agreement within 1.5 % by Ellis and McClintock [2] by measuring mobility of ions within the superfluid. Similarly in ^{3}He, the predicted value of $27\,\mathrm{mm\,s^{-1}}$ has also been confirmed by Ahonen et al. [3] with ion mobility measurements. However, multiple experiments in ^{3}He using mechanical resonators such as vibrating wire resonators (VWR) [4] and later quartz tuning forks (QTF) [5] found the onset of large dissipation already at a lower velocity close to $v_L/3$. An explanation was proposed by C. Lambert [6] that takes into account the suppression of the condensate energy gap on approaching the surface of the vibrating object.

The mechanical oscillators mentioned earlier do not usually allow for significant motion at frequencies other than their resonant frequency due to them typically having very large quality factors giving them a sharp resonance peak. Therefore a new measurement tool has been developed with a very low resonant frequency and a deliberately low quality factor. This device, the Floppy Wire, is a goalpost-shaped superconducting wire of a much larger size than devices typically used in studying motion in superfluid ^{3}He.

It allows for controlled arbitrary motion within superfluid, including steady DC motion.

Prior to the work described in this thesis, the group reported the absence of an onset of large dissipation at constant velocity as $v_L/3$ was exceeded [7]. Even more strikingly, no large heating was observed up to the highest velocity reached, more than four times the Landau critical velocity! A model was proposed that explains the surprising finding by considering the effective shielding of bulk superfluid from the wire by the surface excitations, so-called surface Andreev bound states [8]. The experiments described in this work aim to provide more evidence for the validity of this model and to test its predictions for the dissipation under acceleration.

1.2 Aerogel demagnetisation experiment

Using demagnetised copper as a coolant for superfluid ^{3}He only allows one to reach superfluid temperatures down to about 100 µK but not significantly lower. This is mainly due to the very large thermal boundary resistance between Cu and ^{3}He [9]. The effect of this resistance can be lessened by increasing the surface area available for thermal exchange by using fine Cu powder instead of Cu blocks [10], or by putting sintered silver powder on the copper surface [11]. Nevertheless, this improvement does not extend the accessible temperature range much further down in temperature.

Here, the proposed way to cool the superfluid further is by using a second stage of demagnetisation pre-cooled by the copper powder demagnetisation procedure. For the second demagnetisation we utilise the nuclear magnetic moment of solid ^{3}He that forms on the surfaces of most materials as a coating a few monolayers thick. Naturally, more solid ^{3}He means more cooling power so a material with a large surface area is very desirable. Aerogel is a highly porous stranded material made of inert silica glass with an immense ratio of surface area to volume, making it an ideal candidate for submersing in the superfluid.

The proof of concept of demagnetising solid ^{3}He on the surface of aerogel has already been successfully performed at Lancaster [12]. In those experiments, the lowest superfluid temperature measured was 113 µK and temperatures below 120 µK were maintained for several hours. It is very likely that the superfluid temperature in the near vicinity of the aerogel strands was even lower than that, with the elevated measured temperature being caused by a non-negligible heat leak from the copper demagnetisation stage near the thermometer.

The magnetisation signal, coming mainly from the solid ^{3}He, has been measured by nuclear magnetic resonance (NMR) methods in the 120 µK − 200 mK temperature range. The signal shows an unexpected decrease of magnetisation at the very lowest temperatures. It is speculated that this feature might be a signature of ferromagnetic ordering within the solid ^{3}He. The design and results of this experiment are described in Section 2.6.4.

One of the goals for the new experiment was to investigate the possibility of this magnetic ordering within the solid by studying signatures of NMR and heat capacity. Different from the previous experiment, the new cell contains a volume of superfluid completely shielded from the copper demagnetisation stage by colder aerogel, with extensive thermometry options allowing for better estimation of the superfluid temperature. The sample of aerogel is significantly larger in volume, resulting in a greater solid ^{3}He heat capacity which should cause a longer hold time at the lowest temperatures. Lastly, the aerogel sample contains a cavity in which ultra-cold superfluid can be studied using conventional NMR methods. Moreover, it was anticipated that it should be possible to create a Bose-Einstein condensate (BEC) of magnons within the cavity and investigate its decay and perhaps other properties not previously studied at such low temperatures [13].

1.3 Layout

Chapter 2 covers the fundamentals of ^{3}He physics relevant to the two experiments, mainly the basics of superfluid ^{3}He and the magnetic properties of solid ^{3}He. The principles of NMR are introduced and previous work on solid ^{3}He demagnetisation is described.

Chapter 3 briefly addresses the cooling techniques required in order to achieve superfluid ^{3}He in the ballistic regime of thermal excitations where all the described experiments were intended to take place.

Chapter 4 introduces the primary tools used in our study of superfluid ^{3}He physics - the mechanical oscillators. The fundamentals of mechanical resonance applied to the vibrating wires and quartz tuning forks are explained. The damping of superfluid ^{3}He and its relation to thermometry is also covered. Finally, the modes of operation of the oscillators commonly used in the experimental measurements are described.

Chapter 5 addresses the experiments with the Floppy Wire. First, the device and the techniques of achieving linear motion are described. The chapter then introduces previous findings with the Floppy Wire and attempts to explain them in the context of the posited dissipation model. The new experiments to verify the predictions for dissipation under acceleration follow, together with the temperature dependence of the observed dissipation. The chapter ends with measurements where the Floppy Wire was driven at a higher resonant mode.

Chapter 6 describes our efforts with the double demagnetisation experiment. The chapter first introduces the new experimental cell and the NMR setup. Initial calculations of the cooldown time and magnetic field profiles of the superconducting solenoids are also mentioned. The results of the cell testing and detailed diagnostics of the heating problem follows. The chapter ends with proposals for the future work necessary to identify the heating problem.

Chapter 7 gives a summary of the efforts described within this work and suggests possibilities for new findings in the near future.

Chapter 2

Background

This chapter aims to describe the fundamentals of ^{3}He physics relevant to the experiments in this work. First, some basics of superfluid ^{3}He are introduced together with the magnetic properties of solid ^{3}He. This is followed by an explanation of the basic principles of NMR used for detection of the superfluid and solid signals. Some relevant properties of aerogel are also reviewed. An overview of the previous findings with aerogel demagnetisation and motivation for the new demagnetisation experiment finalises the chapter.

2.1 Fermi liquid theory

In general, particles can be split into two categories depending on their total spin. Particles with zero or integer spin number are bosons while particles with non-integer spin are fermions. Protons, electrons and neutrons are all fermions with spin 1/2 and if these are bound together, as in the case of an atom, it is the total spin that determines its characteristics. Therefore, ^{4}He is a boson and ^{3}He is a fermion. Fermi liquid theory [14] is a simple theory that can be used to describe liquid ^{3}He to a good approximation at low temperatures before the transition to a superfluid state.

Fermions, unlike bosons, obey the Pauli exclusion principle which states that two fermions with equal spin projections can not occupy the same energy level. At $T = 0$, fermions gradually occupy the energy states starting from the lowest up to the Fermi energy E_F following a dispersion curve shown with a red line in Figure 2.1. The particle at the Fermi level can be described by a wavenumber $\boldsymbol{k}_F$ and momentum $\boldsymbol{p}_F$ related by

$$\boldsymbol{p}_F = \hbar \boldsymbol{k}_F \,, \tag{2.1}$$

while the Fermi momentum is related to the energy by

$$E_F = \frac{|\boldsymbol{p}_F|^2}{2m} \,. \tag{2.2}$$

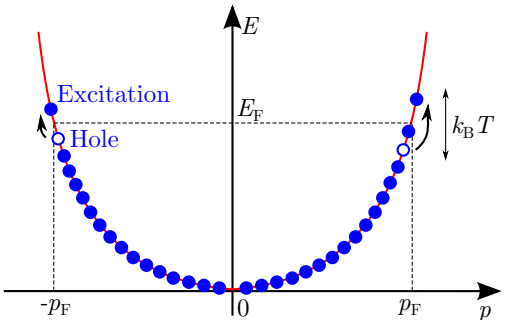

FIGURE 2.1: Dispersion relation for fermions is shown with a red line. At $T > 0$, some of the states in the region $k_B T$ from E_F get excited leaving a hole at their original energy state.

At temperatures $T > 0$, some of the fermions with energy close to E_F, move to a state above E_F. The empty state left behind is referred to as a hole. Reduction of the number of states below E_F is described by the Fermi-Dirac distribution function

$$f(E,T) = \frac{1}{e^{(E-E_F)/k_B T} + 1} \,. \tag{2.3}$$

The distribution function of an ideal Fermi gas when $k_B T \ll E_F$ is shown in Figure 2.2. It is clear that only the states close to E_F can be excited, while the states with lower energy form a non-interacting background.

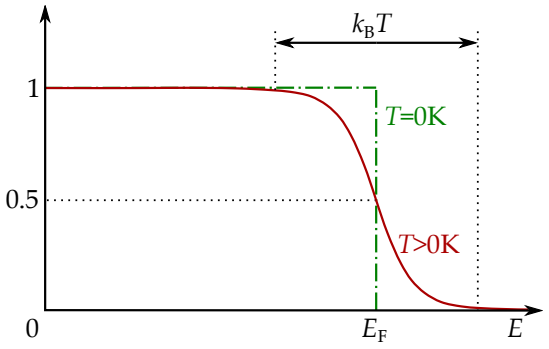

FIGURE 2.2: Fermi-Dirac distribution function for $T = 0$ and $T > 0$.

However, in liquid ^{3}He there are interactions that cause deviations from the ideal Fermi model. Due to interactions between ^{3}He nuclei, the movement of one ^{3}He atom causes the displacement of other atoms as well. One can treat this group movement as a new virtual object with *effective mass* m^* greater than that of the ^{3}He atom. This moving disturbance in the ^{3}He structure is called a *quasiparticle* and carries a spin projection of $\pm 1/2$. Because virtual quasiparticles are weakly interacting and follow Fermi statistics, they can be treated as a Fermi liquid using Landau Fermi liquid theory. Moreover, the new weak interaction also includes the magnetic coupling between quasiparticles allowing one to describe the spin interactions. The model is phenomenological with one quasiparticle corresponding to one ^{3}He atom with a parameter m^*. The weak interaction is described by an infinite set of Landau parameters, the most important of which can be obtained experimentally from measurements of heat capacity, sound velocity and magnetic susceptibility [15].

2.2 Superfluid ^{3}He

Even though the ^{3}He atoms obey the Pauli exclusion principle, a superfluid phase transition is still observed. To explain this phenomena, one can use the analogy with superconductivity explained by the BCS theory [16]. In superconductors, an electron interacts with the lattice, disturbing the lattice and in effect creating a phonon. A second electron can then interact with this phonon, effectively coupling the two electrons together. If this coupling

results in an attractive interaction, this reduces the overall energy and condensation is possible [17]. The coupling is strongest between electrons with opposite momentum, resulting in a *Cooper pair* with total spin number $S = 0$ and angular momentum $L = 0$ existing near the Fermi energy, commonly called *s-wave* pairing. These Cooper pairs are free to form a superconducting state.

The analogy of ^{3}He atoms with electron Cooper pairs is not perfect. ^{3}He atoms are neutral and nor is there a lattice to interact with. However, the Cooper mechanism is independent of the exact nature of the interaction. As long as the interaction is attractive, Cooper pairs can form. For ^{3}He, moving a magnetically polarized quasiparticle locally induces the opposite polarisation in the fluid. The locally modified field attracts another quasiparticle and causes a coupling between the two quasiparticles with parallel spin, creating a Cooper pair with $S = 1$, a *p-wave* pairing. Unlike electrons, ^{3}He quasiparticles are objects with significant size and thus can not collapse into the same point of space which is necessary to satisfy $L = 0$. Only the state with at least $L = 1$ is thus possible. This results in 9 different combinations of spin states $S_z = (-1, 0, +1)$ and angular momenta $L_z = (-1, 0, +1)$ (corresponding to spin combinations: $\uparrow\uparrow$, $\frac{1}{\sqrt{2}}[\uparrow\downarrow + \downarrow\uparrow]$, $\downarrow\downarrow$). The variety of states leads to the possibility of many superfluid phases, in which different states are dominant. At zero magnetic field and low pressures only the *B-phase* state is present in which all the states have equal population. All the measurements in this work were performed in this phase, so the following discussion refers to it only. Other phases can be achieved by increasing the magnetic field or by suppressing geometry to favour surface bound states.

Cooper pairs have a binding energy, which reduces their energy below E_F. This results in a rise in the density of states below and above E_F, forming an energy gap Δ - the energy required to break a Cooper pair and form two quasiparticles.

The excitation curve must thus change shape due the gap and is shown in Figure 2.3. It is convenient to move the origin of the energy axis to E_F

and mirror the part below E_F. Note that the mirrored part must be reflected again around the E axis in order to preserve the velocity directions. The original dispersion curve of the Fermi gas from Figure 2.1 is also shown by the red dashed line.

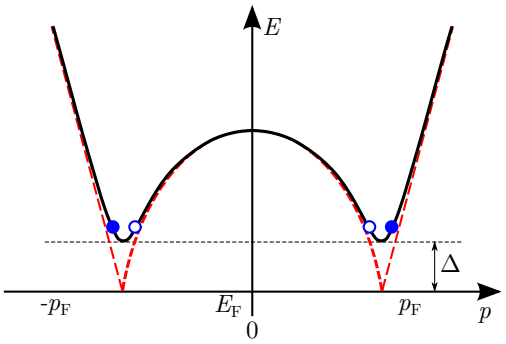

FIGURE 2.3: Dispersion curve for superfluid ^{3}He. Note the change of the origin of the energy axis to E_F. The transformed Fermi Distribution function from Figure 2.1 is shown with a dashed red line.

Each Cooper pair is described by a vector **k** (formed by two quasiparticles with **k** and **-k**) with its excitation energy

$$E\left(\mathbf{k}\right)_{\alpha\beta} = \sqrt{\xi^2 + |\Delta(\mathbf{k})|^2_{\alpha\beta}}\,, \tag{2.4}$$

where ξ is the excess kinetic energy $\xi = \frac{p^2 - p_F^2}{2m^*}$ and $\Delta(\mathbf{k})$ is the energy gap. α and β are the spin states of two quasiparticles, each with two possible values $\pm 1/2$.

In order not to deal with all combinations of spin states α and β, we can introduce a vector $\mathbf{d}(\mathbf{k})$ pointing in the direction of zero spin [18]. $\Delta(\mathbf{k})$ is then expanded by three symmetric 2×2 matrices $i\sigma_\mu\sigma_2$, $\mu = 1, 2, 3$, where σ_μ are Pauli matrices

$$\Delta(\mathbf{k})_{\alpha\beta} = \sum_\mu d_\mu(\mathbf{k})(\sigma_\mu i\sigma_2)_{\alpha\beta} = \begin{pmatrix} -d_1 + id_2 & d_3 \\ d_3 & d_1 + id_2 \end{pmatrix}\,. \tag{2.5}$$

2.2.1 Superfluid B-phase

In the B-phase superfluid the gap energy is isotropic and temperature dependent. The energy gap is greatest at 0 K limit and vanishes at the superfluid transition. The size of the energy gap at 0 K is [18]

$$\Delta(T \to 0) = \Delta_0 = 1.76 k_B T_c \,, \tag{2.6}$$

where T_c is the superfluid transition temperature and $T_c = 0.929\,\mathrm{mK}$ at 0 bar. Throughout this work, the low temperature limit is sufficient for every use and is referred to as Δ_0.

2.2.2 Mean free path and ballistic limit

Upon lowering the temperature, the quasiparticle mean free path ℓ greatly increases and we can demonstrate this change on the effect of fluid viscosity.

At low temperatures, ^{3}He is ideally pure and quasiparticle-quasiparticle and quasiparticle-wall scattering are the only mechanisms contributing to viscosity [19]. Above T_c, the viscosity of ^{3}He is that of a normal Fermi liquid - increasing with decreasing temperature as $1/T^2$, while $\ell \propto T^2$. The potentially confusing fact that the viscosity increases with decreasing mean free path becomes clarified when one realizes that ℓ is the momentum transfer length in the fluid. For example at 1 mK, $\ell = 0.08\,\mathrm{mm}$ and the dynamic viscosity is indeed very high: $\eta = 0.18\,\mathrm{kg\,s^{-1}\,m^{-1}}$ [20].

Below the superfluid transition, the scattering becomes limited even more as the number of quasiparticles rapidly falls with temperature. At $T = 100\,\mu\mathrm{K}$ the mean free path is on the order of a kilometre [21]. Considering that the usual experimental dimension is on the order of centimetres, it is clear that the previous scattering picture must be abandoned and one enters a *ballistic quasiparticle regime*. Here, quasiparticles rarely interact with each other and must equilibrate at the cell walls meaning that simple, intuitive kinetic theory can be used. In the narrow region where ℓ is comparable but still larger than the object dimensions one can fairly successfully use slip

corrections [22]. Our current understanding is limited in the intermediate temperature region, before quasiparticles can be considered to be fully in the ballistic regime. All the measurements presented in this work are well within the ballistic limit.

2.2.3 Quasiparticle conductance

For the calculations described later in this thesis it is important to estimate the maximum thermal energy transported by superfluid ^{3}He in the ballistic approximation.

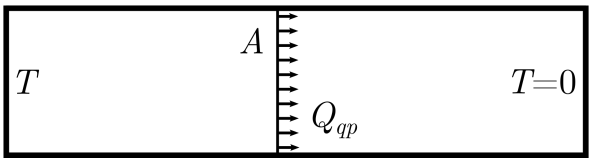

FIGURE 2.4: A model situation to estimate the conductance of ballistically scattered excitations. We consider a tube of ^{3}He of cross-sectional area A with temperature T at one end and $T = 0$ at the other.

Consider a situation as shown in Figure 2.4 where the ^{3}He is enclosed in a tube with a cross-sectional area A with temperature T at one end and $T = 0$ at the other. Since quasiparticles scatter ballistically, the flux of quasiparticles can be defined as

$$Q_{qp} = \frac{1}{2} A \left\langle n v_g \right\rangle \left\langle \varepsilon \right\rangle \ , \tag{2.7}$$

where n is the number density, v_g is the group velocity, $\left\langle n v_g \right\rangle$ is the quasiparticle flux and $\langle \varepsilon \rangle$ is the average energy of quasiparticles. The factor $\frac{1}{2}$ comes simply from the fact that we count only the quasiparticles travelling from left to right. The average energy of a quasiparticle is $\Delta_0 + k_B T$ [23], so we can write

$$Q_{qp} = \frac{1}{2} A \left\langle n v_g \right\rangle (\Delta_0 + k_B T) \tag{2.8}$$

and the problem reduces to estimating the quasiparticle flux $\left\langle n v_g \right\rangle$. It can be expressed as

$$\left\langle n v_g \right\rangle = \int_{\Delta_0}^{\infty} g(\varepsilon) f(\varepsilon) v_g(\varepsilon) \, \mathrm{d}\varepsilon \ , \tag{2.9}$$

where $g(\varepsilon)$ is the density of states and $f(\varepsilon)$ is the Fermi distribution of quasiparticles. One can transform the integral from energy space to momentum space via

$$g(\varepsilon)\,\mathrm{d}\varepsilon = g(p)\,\mathrm{d}p\ . \tag{2.10}$$

This transformation is useful because $\mathrm{d}\varepsilon = \frac{\mathrm{d}\varepsilon}{\mathrm{d}p}\,\mathrm{d}p = v_g\,\mathrm{d}p$ which gives

$$g(\varepsilon)v_g(\varepsilon) = g(p) = g(p_\mathrm{F})\ , \tag{2.11}$$

because in the low temperature limit all the excitations have a momentum close to the Fermi momentum p_F.

For low temperatures, the Fermi distribution from (2.3) can be simplified as

$$f(\varepsilon, T) = \frac{1}{e^{(\varepsilon - E_\mathrm{F})/k_\mathrm{B}T} + 1} \simeq e^{-\varepsilon/k_\mathrm{B}T}, \quad \text{for } \varepsilon \gg k_\mathrm{B}T\ . \tag{2.12}$$

Substituting into (2.9) we derive

$$\left\langle n v_g \right\rangle = g(p_\mathrm{F}) \int_{\Delta_0}^{\infty} e^{-\varepsilon/k_\mathrm{B}T}\,\mathrm{d}\varepsilon = g(p_\mathrm{F}) k_\mathrm{B} T e^{-\Delta_0/k_\mathrm{B}T}\ . \tag{2.13}$$

The last unknown is the density of states. In ^{3}He-B, the Fermi surface as well as the energy gap is isotropic. The Fermi surface thus forms a sphere in momentum space. The calculation of density of states can then be achieved by calculating the number of k states within the spherical shell of radius $|k|$. The derivation can be found in any solid state physics textbook (e.g. [24]), with the result given by

$$g(p_\mathrm{F}) = g(E_\mathrm{F}) v_\mathrm{F} = \frac{v_\mathrm{F}}{\pi^2} \left(\frac{2m}{\hbar^2}\right)^{3/2} \sqrt{E_\mathrm{F}}\ . \tag{2.14}$$

Finally, we insert the quasiparticle flux into (2.8) and obtain the relation for the heat flow

$$Q_{qp} = \frac{1}{2} A g(E_\mathrm{F}) v_\mathrm{F} k_\mathrm{B} T e^{-\Delta_0/k_\mathrm{B}T} \left(\Delta_0 + k_\mathrm{B}T\right)\ . \tag{2.15}$$

2.3 Two energy level system

As ^{3}He has spin $\frac{1}{2}$, solid ^{3}He is a good approximation to a two energy level system and its properties such as magnetisation, entropy or heat capacity can be derived using this simple model.

An atom of ^{3}He consists of an odd number of nuclei and thus each atom has a non-zero magnetic moment $\boldsymbol{\mu}$ along the nuclear angular momentum $\hbar\boldsymbol{I}$. The magnitudes of the two are related through the gyromagnetic ratio γ as

$$\boldsymbol{\mu} = \gamma\hbar\boldsymbol{I} \,. \tag{2.16}$$

In an external magnetic field $\boldsymbol{B}$ each atom has a corresponding magnetic energy

$$E = -\boldsymbol{\mu}\cdot\boldsymbol{B} \,. \tag{2.17}$$

Aligning the magnetic field along the z axis and combining (2.16) and (2.17) the magnetic energy is then

$$E = -\gamma\hbar I_z B \,, \tag{2.18}$$

where $\hbar I_z$ is the projection of angular momentum onto the direction of the magnetic field. In the case of ^{3}He, the situation is quite simple since I_z can only be either $+\frac{1}{2}$ or $-\frac{1}{2}$. The two states are labelled up ($\uparrow$) and down ($\downarrow$) as the nuclear magnetic moment is either parallel with the magnetic field ($\uparrow$) or anti-parallel ($\downarrow$).

This brings us to the two energy level system. When no external magnetic field is present, the energy of all states is E_0. However, once an external field is applied, the energy of the nuclei E_0 splits into two energy levels $E_0 \pm \mu B$ depending on the mutual orientation of the magnetic field and the nuclear magnetic moment. The splitting is known as the Zeeman effect [24] and is shown in Figure 2.5.

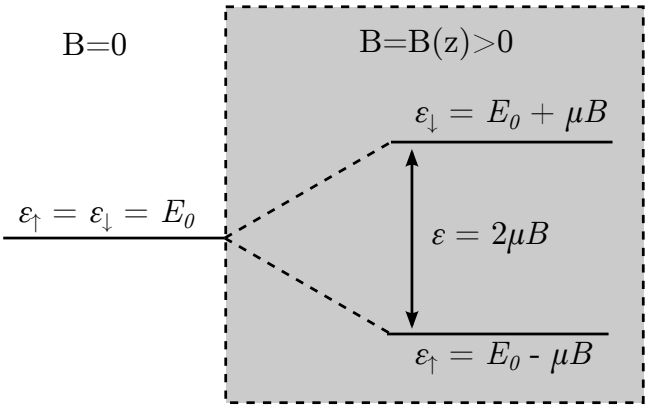

FIGURE 2.5: In the absence of an external magnetic field all atoms are in the energy state E_0. When a magnetic field in the direction of the z axis is applied, the energy level E_0 splits into two energy levels $E_0 \pm \mu B$.

The occupation of the states follows the Boltzmann distribution and the partition function for the two level system is given by

$$Z = \sum_j e^{-\varepsilon_j/k_B T} = e^{-\varepsilon_\downarrow/k_B T} + e^{-\varepsilon_\uparrow/k_B T} \ . \tag{2.19}$$

Using $\varepsilon = \varepsilon_\uparrow - \varepsilon_\downarrow$ we then obtain

$$Z = e^{-\varepsilon_\downarrow/k_B T}\left(1 + e^{-\varepsilon/k_B T}\right) \ . \tag{2.20}$$

The populations of the states are given by:

$$n_\downarrow = \frac{N}{Z} e^{-\varepsilon_\downarrow/k_B T} = \frac{N}{1 + e^{-\varepsilon/k_B T}} \ , \tag{2.21a}$$

$$n_\uparrow = \frac{N}{Z} e^{-\varepsilon_\uparrow/k_B T} = \frac{N e^{-\varepsilon_\uparrow/k_B T}}{e^{-\varepsilon_\downarrow/k_B T}\left[1 + e^{-\varepsilon/k_B T}\right]} = \frac{N e^{-\varepsilon/k_B T}}{1 + e^{-\varepsilon/k_B T}} \ , \tag{2.21b}$$

$$N = n_\downarrow + n_\uparrow \ . \tag{2.21c}$$

Now the population of the two states is expressed only in terms of the energy gap ε between them, instead of their individual energies, and the temperature. The fractional populations are plotted in Figure 2.6.

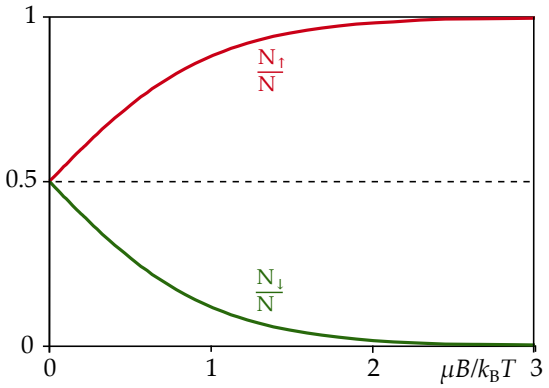

FIGURE 2.6: Fractional populations of the spin states. At low temperatures, most of the atoms are in the state with lower energy (↑), while with raising temperature the ↑ and ↓ states become equally populated.

The number of excess spin states is defined as the difference between the populations of ↑ and ↓ states

$$n_\downarrow - n_\uparrow = N\frac{1-e^{-\varepsilon/k_B T}}{1+e^{-\varepsilon/k_B T}} = N\tanh\left(\varepsilon/2k_B T\right) \ , \tag{2.22}$$

which relates to the magnetisation as

$$M = \left(n_\downarrow - n_\uparrow\right)\mu = N\tanh\left(\varepsilon/2k_B T\right)\mu = N\mu\tanh\left(\mu B/k_B T\right) \ , \tag{2.23}$$

substituting for $\varepsilon = 2\mu B$. In the case where $k_B T \gg \mu B$, we obtain Curie's Law with magnetisation inversely proportional to temperature

$$M = N\mu^2 B/k_B T \ . \tag{2.24}$$

The magnetic field contribution to the heat capacity can be found from the differentiation of magnetisation energy with respect to temperature assuming constant energy levels (i.e. constant magnetic field)

$$C = \left(\frac{\mathrm{d}E}{\mathrm{d}T}\right)_B = \left(\frac{\mathrm{d}M}{\mathrm{d}T}\right)_B B = \frac{N\mu\varepsilon B}{2k_B T^2}\operatorname{sech}\left(\frac{\varepsilon}{2k_B T}\right) \ . \tag{2.25}$$

Moreover, the entropy of the system can be derived using

$$S = k_B\frac{\partial\left(T\ln Z\right)}{\partial T} \ . \tag{2.26}$$

Inserting the partition function and simplifying we get [25]

$$S = Nk_B \left\{ \ln\left[1 + e^{-\varepsilon/k_B T}\right] + \frac{\varepsilon}{k_B T} \frac{e^{-\varepsilon/k_B T}}{\left[1 + e^{-\varepsilon/k_B T}\right]} \right\} . \tag{2.27}$$

When $k_B T \ll \mu B$, the first term is negligible and the entropy relation reduces to

$$S \approx \frac{N\varepsilon}{T} e^{-\varepsilon/k_B T} , \tag{2.28}$$

such that $S \to 0$ as $T \to 0$, satisfying the third law of thermodynamics.

At high temperatures when $k_B T \gg \mu B$, both terms are equal and we find $S = Nk_B \ln 2$ which corresponds to an equal number of spins $\uparrow$ and $\downarrow$ as in Figure 2.6.

When $k_B T > \mu B$, the system deviates from S_∞, the true value at infinite temperature, as

$$S = S_\infty - \text{constant} \cdot \frac{B^2}{T^2} . \tag{2.29}$$

This is a very helpful equation used to describe the adiabatic demagnetisation process mentioned in section 3.2.

2.3.1 Curie-Weiss mean field model

All the equations in the previous section 2.3 were derived assuming non-interacting spins. This is not always the case with ^{3}He and the spins need to be considered at least weakly interacting. The Curie-Weiss mean field model assumes that each spin is not only influenced by the external field B, but also by the field from neighbouring spins, which depends on the magnetisation. The resulting *effective field* has the form

$$B_{\text{eff}} = B + \lambda_W M , \tag{2.30}$$

where λ_W is the Weiss molecular field constant [24]

$$\lambda_W = \frac{k_B \Theta_C}{N\mu^2} \tag{2.31}$$

with Θ_C being the Curie-Weiss temperature. This is the temperature at which a significant portion of spins begin to enter the state with the same magnetic moment and the ensemble becomes ordered. NMR measurements on aerogel by Sprague et. al. estimated this to be $\sim 0.4\,\mathrm{mK}$ [26] and subsequently 0.48 mK was inferred by Fisher et. al. [12] at low pressures.

The magnetisation can be derived in the same way as that of the ideal non-interacting two level system [see (2.23)], giving

$$M = \mu N \tanh\left[\frac{\mu\left(B + \lambda_W M\right)}{k_B T}\right] . \tag{2.32}$$

This is a transcendental equation for M and can not be solved analytically. The equation can be however solved by standard numerical methods.

The effective field of solid ^{3}He at 200 µK in an external field of 130 mT is $\sim 700\,\mathrm{mT}$, which shows that the effect of spin interaction is significant and can not be neglected.

2.4 NMR principles and measurement

2.4.1 Basic principles of NMR

Nuclear magnetic resonance (NMR) is one of the key tools to study the magnetic properties of both solid and superfluid ^{3}He in the aerogel demagnetisation experiment. Therefore, the basic principles of this widely used technique are briefly explained in this section.

In section 2.3 we introduced the concept that an atomic nucleus with nuclear angular momentum produces a magnetic moment of magnitude described by the quantum mechanical equation (2.16).

The rate of change of angular momentum of a system of spins is equal to the torque that acts on it. For a single atomic nucleus we can write the gyroscopic equation

$$\hbar \frac{\mathrm{d}\boldsymbol{I}}{\mathrm{d}t} = \boldsymbol{\mu} \times \boldsymbol{B_0} , \tag{2.33}$$

or, using (2.16)

$$\frac{\mathrm{d}\boldsymbol{\mu}}{\mathrm{d}t} = \gamma\boldsymbol{\mu} \times \boldsymbol{B_0} \,. \tag{2.34}$$

For the system with only a single value of γ, we can sum up the individual magnetic moments of the spin ensemble in (2.34) and obtain the magnetisation

$$\frac{\mathrm{d}\boldsymbol{M}}{\mathrm{d}t} = \gamma\boldsymbol{M} \times \boldsymbol{B_0} \,. \tag{2.35}$$

If the magnetic field is aligned with the $\hat{\boldsymbol{z}}$-axis $\boldsymbol{B_0} = B_0\hat{\boldsymbol{z}}$, the solution to (2.34) is that the spins precess about this axis at the Larmor frequency f_L,

$$f_\mathrm{L} = \frac{\gamma B_0}{2\pi} \,. \tag{2.36}$$

In external magnetic field B_0, the angular momentum will adopt one of the allowed $(2I+1)/2$ orientations with respect to that field. In the case of ^{3}He with $I_z = \pm 1/2$, we arrive at the two level system, earlier described with the precession of spins as shown in Figure 2.7

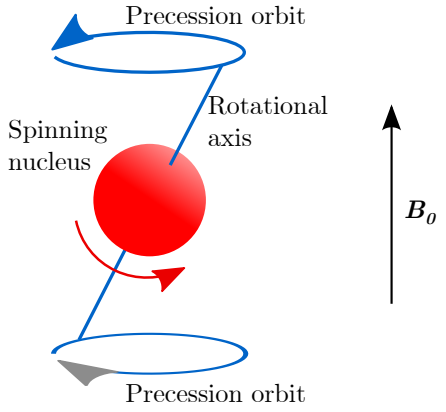

FIGURE 2.7: Schematic representation of a precessing spinning nucleus. The atomic nucleus with angular momentum $\boldsymbol{\mu}$ spins around its axis of rotation. In external magnetic field $\boldsymbol{B_0}$, the angular momentum will adopt one of the allowed orientations and the rotational axis will precess around the precession orbit.

In equilibrium at a given temperature, there will be a non-zero net ensemble average of spin magnetisation only along the $\hat{\boldsymbol{z}}$-axis of the form as in (2.23). If the net magnetisation component M_z is not in equilibrium, it

returns to equilibrium at a rate proportional to the difference from M_0

$$\frac{\mathrm{d}M_z}{\mathrm{d}t} = \frac{M_0 - M_z}{\tau_1} \,, \tag{2.37a}$$

where τ_1 is the so-called *longitudinal relaxation time* which describes the time it takes for the spin system to come to thermal equilibrium with the atom and the surrounding atoms.

Similarly, assuming a static magnetic field $\boldsymbol{B_0} = B_0\hat{\boldsymbol{z}}$, the magnetisation components M_x and M_y are not zero, and they will decay exponentially to zero since in equilibrium $M_x = M_y = 0$, so that

$$\frac{\mathrm{d}M_x}{\mathrm{d}t} = \frac{-M_x}{\tau_2} \,, \tag{2.37b}$$

$$\frac{\mathrm{d}M_y}{\mathrm{d}t} = \frac{-M_z}{\tau_2} \,, \tag{2.37c}$$

where τ_2 is called *transverse relaxation time* which describes the decoherence of the transverse nuclear spin magnetisation.

We can take into account the spin-lattice and spin-spin interactions described by (2.37) and adjust the equation of motion (2.35) to arrive at a set of *Bloch equations* describing the decay of magnetisation

$$\frac{\mathrm{d}M_z}{\mathrm{d}t} = \gamma \left(\boldsymbol{M} \times \boldsymbol{B_0}\right)_z + \frac{M_0 - M_z}{\tau_1} \,, \tag{2.38a}$$

$$\frac{\mathrm{d}M_x}{\mathrm{d}t} = \gamma \left(\boldsymbol{M} \times \boldsymbol{B_0}\right)_x - M_x/\tau_2 \,, \tag{2.38b}$$

$$\frac{\mathrm{d}M_y}{\mathrm{d}t} = \gamma \left(\boldsymbol{M} \times \boldsymbol{B_0}\right)_y - M_y/\tau_2 \,. \tag{2.38c}$$

The underlying mechanism of NMR is the measurement of the change of population of energy levels. This is done by the application of a second oscillating field $\boldsymbol{B_1}$ perpendicular to $\boldsymbol{B_0}$. As mentioned in the previous Section 2.3, the difference between two energy levels relates to the magnetic moment μ and external magnetic field B_0 . This energy can be assigned a

frequency of the electromagnetic field

$$\Delta_0 E = 2\mu B_0 = \hbar f \ . \tag{2.39}$$

The energy levels are fixed in every spin, corresponding to a fixed and unique Larmor frequency f_L from (2.36). Only when the frequency of the field $\boldsymbol{B_1}$ is equal to f_L, the atoms can absorb energy and shift to the higher energy state. Equation (2.36) is thus the fundamental condition for magnetic resonance absorption.

2.4.2 Pulsed NMR measurement

We create the static field $\boldsymbol{B_0}$ along the $\hat{z}$-axis with the *NMR solenoid*. Another smaller pair of coils is placed around the sample to create a transverse magnetic field $\boldsymbol{B_1}$ perpendicular to $\boldsymbol{B_0}$, see Figure 2.8.

To deflect the magnetic moment from the equilibrium position, a short pulse of alternating field $\boldsymbol{B_1}$ is applied. The frequency of the field is the Larmor frequency f_L shown in (2.36). The pulse brings energy hf_L and changes the population of the spin states towards higher energies. Moreover, for the duration of the pulse when both $\boldsymbol{B_0}$ and $\boldsymbol{B_1}$ are present the magnetisation rotates about the axis of the resulting effective field $\boldsymbol{B} = \boldsymbol{B_0} + \boldsymbol{B_1}$. This creates non-zero components of magnetisation M_x and M_y, see Figure 2.9. Two decay processes are present. The spin-spin interaction cancels out the coherent precession of spins along $\hat{z}$-axis, reducing M_x and M_y to 0 (Figure 2.9 b). The spin-orbital interaction flips the spins back to the equilibrium distribution and thus increases M_z (Figure 2.9 c).

The same coil that produces $\boldsymbol{B_1}$ is used to detect the decaying signal after the pulse. Precessing magnetisation in the x-y plane induces currents in the coil and τ_2 and M_0 can be estimated from the decaying signal. This coil needs to resonate at f_L, so there must be a capacitive element in addition to the inductance of the coil to achieve the right resonance frequency of the *RLC* circuit. In our experiment two pairs of coils were used to measure

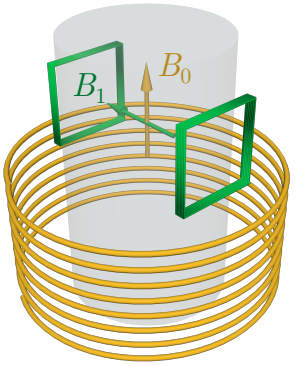

FIGURE 2.8: Orientation of $\boldsymbol{B_0}$ and $\boldsymbol{B_1}$ fields.

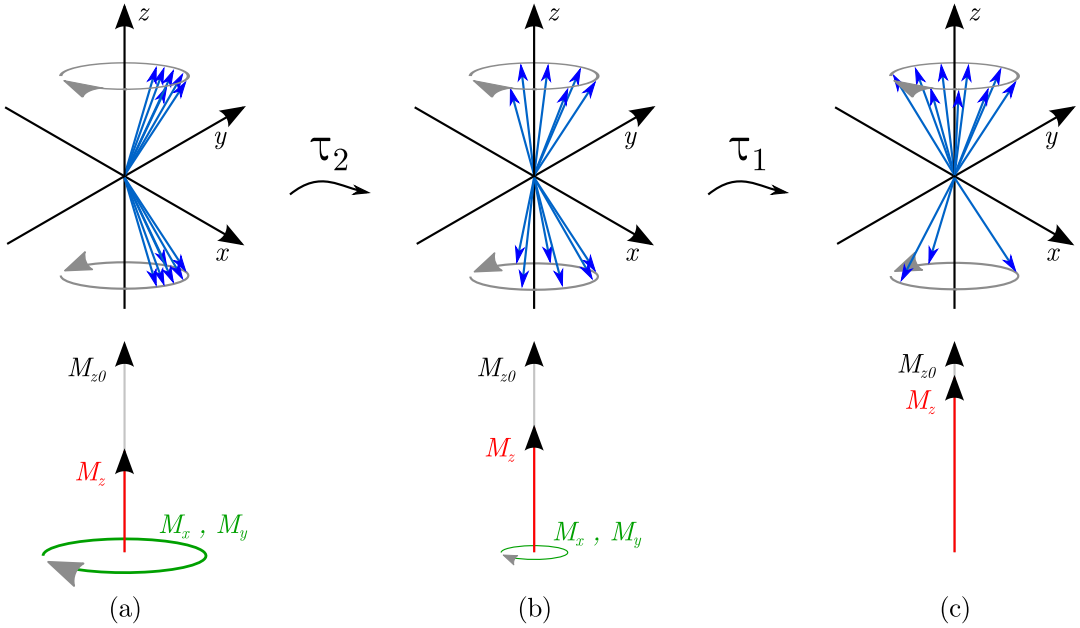

FIGURE 2.9: Schematic representation of precessing spins. (a) The situation shortly after applying $\boldsymbol{B_1}$ pulse. (b) After τ_2 the precession of spins along the z-axis is no longer coherent, $M_x = M_y \to 0$. (c) After τ_1 the equilibrium distribution of spin up-down orientations is reached again, $M \to M_0$.

NMR in two different sections of the sample. The pairs of coils are in an orthogonal arrangement to reduce inductive coupling between them. Our NMR setup is described in Section 6.5.

2.5 Bose Einstein condensation of magnons

The study of Bose Einstein Condensation (BEC) of magnons at ultra-low temperatures was one of the main goals of the aerogel demagnetisation

experiment. The topic is only briefly mentioned here, because the unexpected heating problems (examined in Chapter 6) prohibited reaching temperatures low enough for the formation of the magnon condensate. Comprehensive information about magnon BEC can be found in the recent review chapter by M. Bunkov and G. E. Volovik [13], or in the PhD thesis of P. Heikkinen [27].

At temperatures below about 0.2 T_c in superfluid ^{3}He, a pulse of NMR excitation can generate a coherently precessing spin state with a lifetime as long as 1000 s. This precession can be explained in terms of Bose Einstein condensation of spin waves - *magnons*. Magnons are the quanta of magnetic excitations in a magnetically ordered group of magnetic moments. At a potential minimum and low enough temperature, magnetic moments of individual ^{3}He atoms can spontaneously synchronize their phase of precession. The formation of the condensate is truly spontaneous as the system the can be excited by a frequency very different from the resulting coherent signal, even by white noise [28].

The potential minimum along the $\hat{z}$ axis is achieved by a shallow magnetic field minimum created by a small coil (mentioned in Section 6.4.3). The potential minimum is formed naturally along the radial direction of the cavity. In the middle of the cavity the vector of orbital momentum is oriented along the external magnetic field in the vertical direction. However, near the edge of the container the orbital momentum must be perpendicular to the surface. The potential trap is demonstrated in Figure 2.10. It is unclear however, whether the trap will fully form inside the aerogel cavity of our experimental cell as the direction of the orbital momentum along the aerogel cavity boundary is still an open question, that we hoped to investigate.

Amongst the many other opportunities that the study of magnon BEC might offer, the condensate allows for the determination of the temperature of the superfluid inside the aerogel cavity. Since there is no mechanical

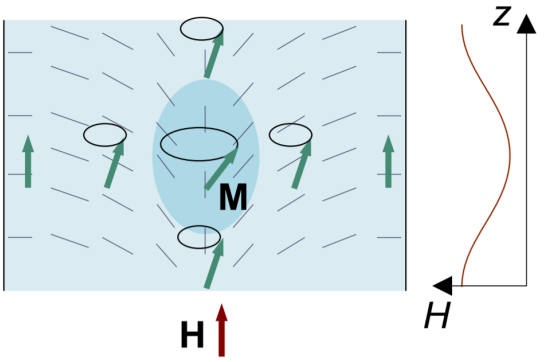

FIGURE 2.10: A schematic representation of a magneto-textural potential minimum forming a magnon BEC. In the vertical direction, the condensate is trapped by a magnetic field minimum created by a small pinch coil. The trap is formed radially by the direction of the orbital momentum vector. Far from the container walls it is aligned vertically, along the external magnetic field. However, the vector is perpendicular to the cell wall in its near vicinity. Figure taken from [13].

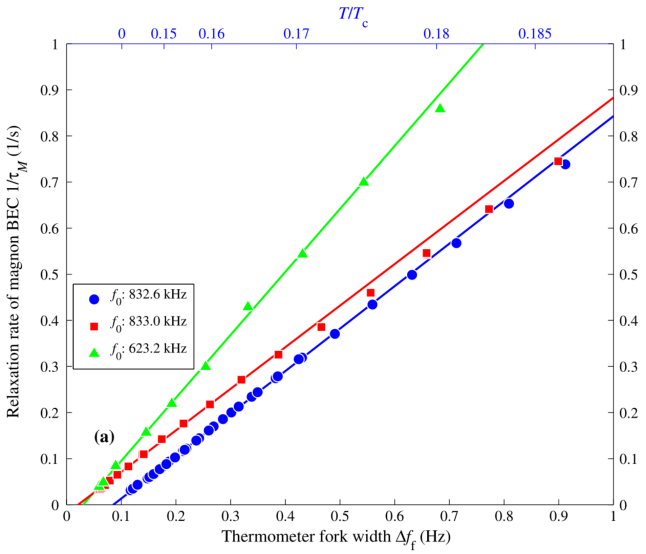

FIGURE 2.11: Decay time of a magnon BEC shows linear dependence on the resonant width of the tunning fork inside the cell up to $T \simeq 0.165\, T_c$, making it a suitable thermometer at very low temperatures. Figure modified from [29].

oscillator thermometer inside the cavity, it is actually the only way to determine the local temperature. Heikkinen et al. [29] have shown that below $\sim 0.175\, T_c$ the decay time of magnon precession depends linearly on the resonant width of the tuning fork inside the cell, see Figure 2.11. As will be shown in Section 4.4.2.1, the fork width depends on the quasiparticle density ρ_q, allowing for the calculation of the temperature using $\rho_q \propto e^{-\Delta_0/k_B T}$.

2.6 Aerogel

2.6.1 Properties of aerogel

Aerogel is an extremely porous material consisting of randomly interconnected $Si0_2$ strands only a few nanometres thick. This fragile structure is achieved by supercritical drying of silicon dioxide in solvent when the solvent is vented above the critical point. The goal is to remove the solvent from the aerogel without creating a two-phase system with capillary forces that would otherwise crush the aerogel structure. The process follows a path similar to that shown in Figure 2.12. The solution is heated up and pressurized above the critical pressure and temperature of methanol ($p_c = 81\,\text{bar}$ and $T_c = 512\,\text{K}$). Then the chamber is slowly depressurized to atmospheric pressure and allowed to cool down while maintaining the solvent in the gas phase. The sample used in our experiment was manufactured by the Low Temperature Group at Northwestern University, and their fabrication process is described in more detail in [30].

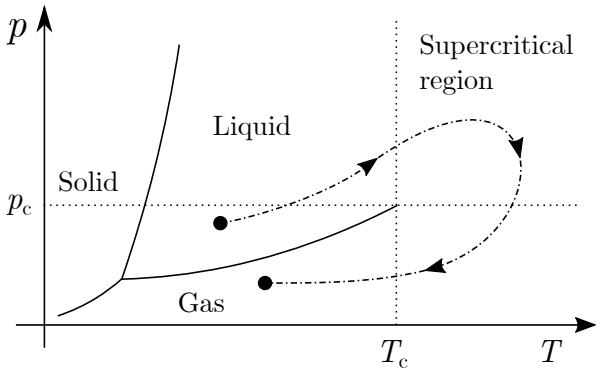

FIGURE 2.12: Supercritical drying procedure

The percentage porosity of aerogel is defined as

$$P = 100(1 - \rho_a/\rho_{Si0_2}) \,, \tag{2.40}$$

where ρ_a is the aerogel density and $\rho_{Si0_2} = 2.20\,\text{g}\,\text{cm}^{-3}$ is the density of silicon dioxide [13].

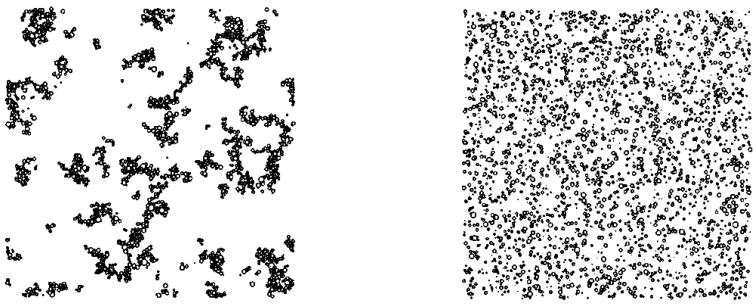

(a) (b)

FIGURE 2.13: (a) Projection of 30 nm thick 98 % aerogel simulated using DCLA model. (b) Projection of the same aerogel slice simulated with a random arrangement of strands. The DCLA model in (a) is in good agreement with small angle X-ray scattering experimental data and thus gives a better insight on the internal structure of aerogel. Figure taken from [36].

In this work, $P = 98\,\%$ aerogel was used, the same porosity that has been used in many previous experiments [31–33]. Porto and Parpia [34] stated the typical diameter of aerogel strands to be 50 Å with a broad spectrum of strand separation ranging from 25 up to 1000 Å. This is due to the fact that the strands tend to produce smaller clusters. Diffusion-limited cluster aggregation (DLCA) numerical models show this clustering and the results are in good agreement with small angle X-ray scattering experiments [35]. One such DLCA study of Porto and Parpia [36] is shown in Figure 2.13. This study also addresses the estimation of the average pore size and geometrical mean free path of quasiparticles inside aerogel ℓ_a as a function of porosity

$$\ell_a = 1.76 \left(1 - \frac{P}{100}\right)^{-1.1} , \tag{2.41}$$

which relates directly to the mean free path of the ballistic quasiparticles inside aerogel.

Numerous studies on 98 % aerogel suggest that the three most important length scales have the values listed in Table 2.1.

TABLE 2.1: Generally accepted values of the three different length scales of 98 % aerogel [13].

Average cluster diameter	3–5 nm
Correlation length	40–80 nm
Geometrical mean free path	120–170 nm

2.6.2 Transition of ^{3}He to superfluid in aerogel

The superfluid transition of ^{3}He is greatly suppressed in aerogel, as has been shown experimentally with torsional oscillators [34, 37], acoustic spectroscopy [38, 39], NMR [26] and transport measurements [40]. The suppression is present because the geometrical mean free path is of the same order of magnitude as the coherence length of thermal excitations, which is thus limited. The transition temperature differs between experiments and even between aerogel samples of the same porosity. This is probably due to the diversity of aerogel samples and different methods of manufacturing them. Porto and Parpia [34] didn't observe any superfluid transition below 2.4 bar down to the lowest temperature 0.35 mK, and at higher pressures they reported a similar pressure dependence as that in bulk, though shifted by $\sim$ 0.5 mK towards lower temperatures. They also reported a different superfluid fraction than in the bulk. Sprague et al. [26] didn't observe any superfluid transition below 12.9 bar down to 0.9 mK. Fisher et al. [40] observed the first sign of superfluidity around 7 bar and 0.5 mK in 150 mT.

2.6.3 Magnetisation of solid ^{3}He on aerogel strands

As for many materials, several atomic layers of solid ^{3}He are formed on the surfaces when immersed in liquid ^{3}He and exhibit the Curie-Weiss magnetisation described in Section 2.3.1. Since solid ^{3}He is only a few nm thick and lacks a regular crystalline lattice, the term "solid-like" ^{3}He is more adequate. Nevertheless, in this thesis the layer is often referred to as solid ^{3}He for simplicity. The total magnetisation M is then the sum of both solid magnetisation M_s and that of the liquid M_l between aerogel pores. M_l is constant with temperature, while $M_s \sim 1/T$. The specific surface area of aerogel is

extremely high ($\sim$ 1000 $m^2\,g^{-1}$) and thus the solid component dominates the magnetisation at the lowest temperatures. At the highest temperatures the magnetisation of solid ^{3}He is insignificant, so the liquid contribution is dominant. In order to study only the superfluid NMR signal, aerogel is often coated with several non-magnetic layers of solid ^{4}He [41, 42]. Recently, an extensive NMR study was conducted by Colin et. al. [42] in order to study the solid ^{3}He layer across a wide range of pressures. They observed a monotonic increase in the solid fraction and a decrease in the Curie-Weiss temperature with pressure - a sign of the growth of disordered solid, see Figure 2.14.

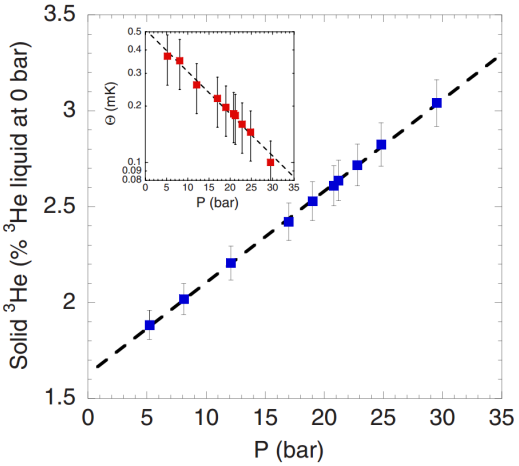

FIGURE 2.14: Linear rise of the amount of solid growing on aerogel and the linear decrease of the Curie-Weiss temperature Θ_C with pressure suggests the growth of disordered solid ^{3}He. Figure taken from [42].

2.6.4 Previous work in Lancaster

Previous work in Lancaster studied the magnetisation and heat capacity of solid ^{3}He on aerogel at the lowest temperatures well below 1 mK [12] with an experimental cell shown in Figure 2.15. The experiment aimed to verify the method of demagnetisation of solid ^{3}He in order to reach ultra-cold superfluid ^{3}He. Our new experiment described in Chapter 6 shows much similarity to this early work, results of which serve as motivation for further study of the phenomena revealed.

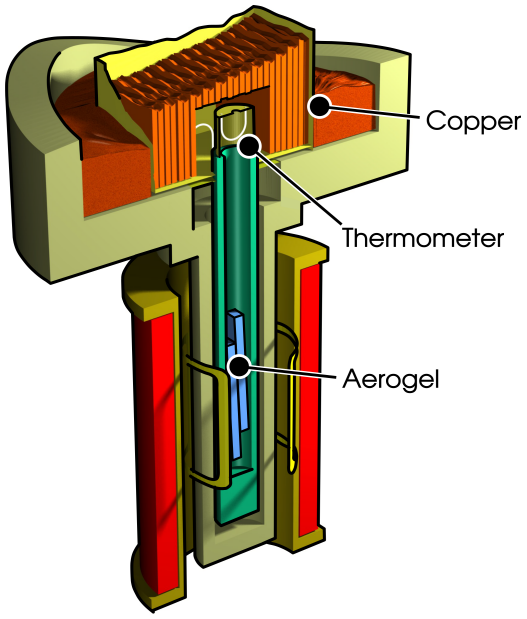

FIGURE 2.15: Schematic representation of the first aerogel demagnetisation experiment. Note the large distance between the thermometer and the aerogel. Modified from [12].

The aerogel sample immersed in superfluid ^{3}He was precooled to 200 µK in a magnetic field of 100 mT and subsequently demagnetised. The time dependence of the superfluid ^{3}He temperature during and after demagnetisation is shown in Figure 2.16. First, note that the final temperature of superfluid ^{3}He is independent of the final magnetic field. In this experiment, the vibrating wire thermometer was placed near the copper powder demagnetisation stage that remains at $\sim$ 200 µK which thus introduces a constant heat leak, see Figure 2.15. The solid ^{3}He, and perhaps the superfluid surrounding it, is probably much colder than the limiting measurement of $\sim$ 113 µK. When demagnetising to lower magnetic fields below 9 mT, a kink in the warmup curves was observed. Here, the warmup rate decreases significantly, suggesting either an increase in the heat capacity of the system or the existence of a latent heat, both signatures of a possible phase transition.

Utilising standard pulsed NMR methods, the group measured the total magnetisation of the system during a 6-day long warmup after demagnetising to 33.3 mT, see Figure 2.17. At the highest temperatures, down to $\sim$ 70 mK, the magnetisation of the Fermi liquid is the only contribution (shown with a blue line). Below this temperature, the solid ^{3}He dominates

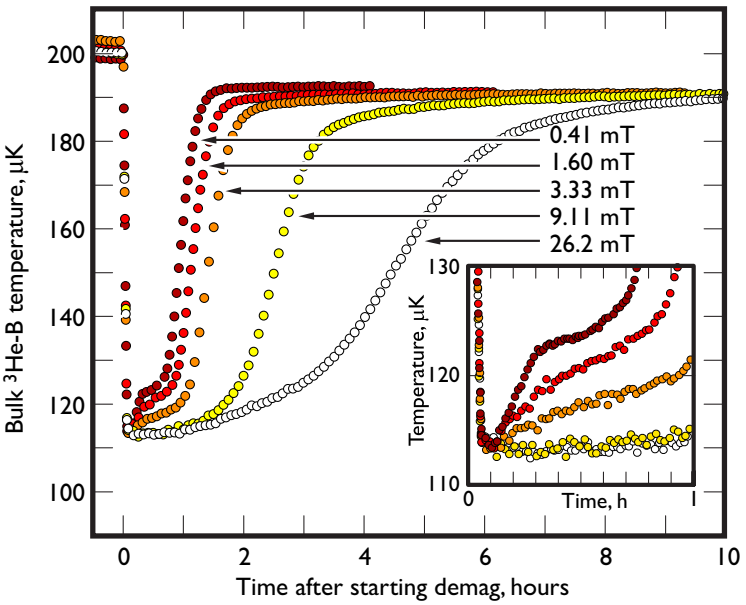

FIGURE 2.16: Evoltion of superfluid ^{3}He temperature after aerogel demagnetisation. The lowest temperature 131 μK is independent of final field, suggesting the solid ^{3}He temperature is much colder, see the text. Note the kink on warmup curves when demagnetising to magnetic fields below 9 mT. Figure taken from [12].

the total magnetisation with excellent agreement to the Curie-Weiss model described in Section 2.3.1 with Curie-Weiss temperature $\Theta_C = 0.48\,\text{mK}$ (shown with a red line). Below 1 mK, the solid ^{3}He spin system is nearing saturation and the Curie-Weiss model is no longer applicable. The measured magnetisation at lowest temperatures below 130 μK, shown in the insert of Figure 2.17, reveals two interesting features. First, the observed increase in magnetisation below $\sim$ 130 μK is probably an artefact of thermometry. The quasiparticle thermal conductance (derived in Section 2.2.3) rapidly drops with temperature, causing a decoupling of solid the ^{3}He temperature and the temperature measured by the vibrating wire thermometer in the vicinity of the copper demagnetisation stage. Without this decoupling, the magnetisation would probably follow the linear extrapolation of the higher temperature data shown by the green line. A more striking feature is the drop of magnetisation at the lowest measured temperatures. Since solid ^{3}He works as a refrigerant and can only warm up monotonically after the demagnetisation, the feature can not be of thermal origin. Bradley et. al. speculate that this can be an indication of anti-ferromagnetic ordering within the solid.

Similar ordering has been observed within bulk solid ^{3}He at much higher magnetic field and temperature (0.4 T and 1 mK [43]) and is of theoretical interest (bulk solid ^{3}He [44] and 2D solid ^{3}He films [45]). The same dataset is also shown in Figure 2.18 in order to highlight the well-followed $\sim 1/T$ dependence of Curie Weiss solid as well as to show the Curie Weiss temperature Θ_C by extrapolation to zero magnetisation.

The main advantage of using solid ^{3}He over copper for cooling the superfluid is the 'fast exchange mechanism'. Thanks to this mechanism, ^{3}He atoms move freely between the solid and liquid phases, contributing to better thermalisation. This mechanism manifests itself as a merging of liquid and solid NMR signature at low temperatures [46]. It not clear however, to what extent this mechanism is present at ultra-low temperatures. J. Pollanen et al. report an onset of decoupling of solid ^{3}He spins from the superfluid at around 1.2 mK [47]. Nevertheless, the Lancaster experiment has shown that solid ^{3}He can be successfully demagnetised to efficiently cool superfluid down to at least 113 µK.

Our experimental setup described in Chapter 6 builds on previous findings and introduces a few improvements. Further cooling is perhaps possible with better shielding from the heat load from the warmer nuclear demagnetisation stage and by studying the superfluid in the vicinity of the aerogel sample. Moreover, the possible anti-ferromagnetic transition in solid ^{3}He requires further investigation. A larger amount of aerogel will increase the solid ^{3}He NMR signal and better shielded thermometry might resolve the heat capacity signature during this magnetic ordering. The introduction of a cavity inside the aerogel should allow for the study of superfluid free from any heat load and directly cooled by solid ^{3}He.

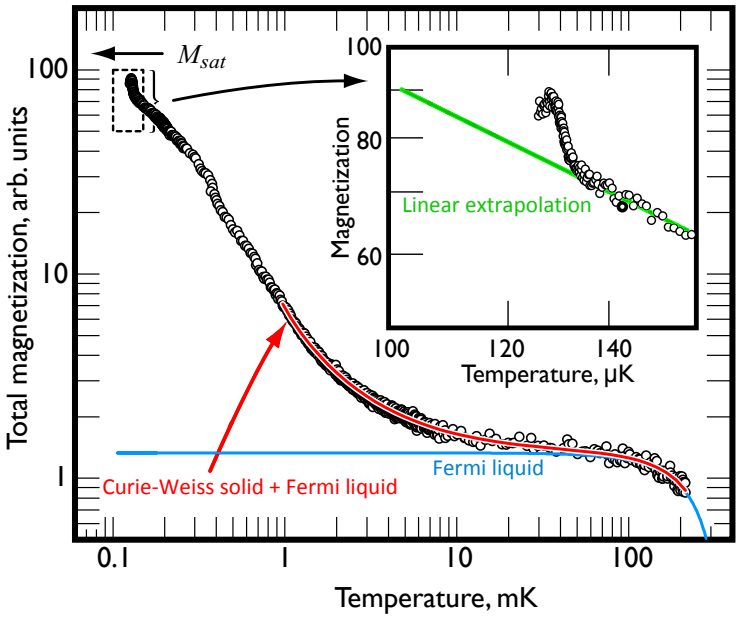

FIGURE 2.17: Temperature dependence of solid and superfluid ^{3}He magnetisation measured on a warmup after demagnetisation to 33.3 mT. Figure modified from [12].

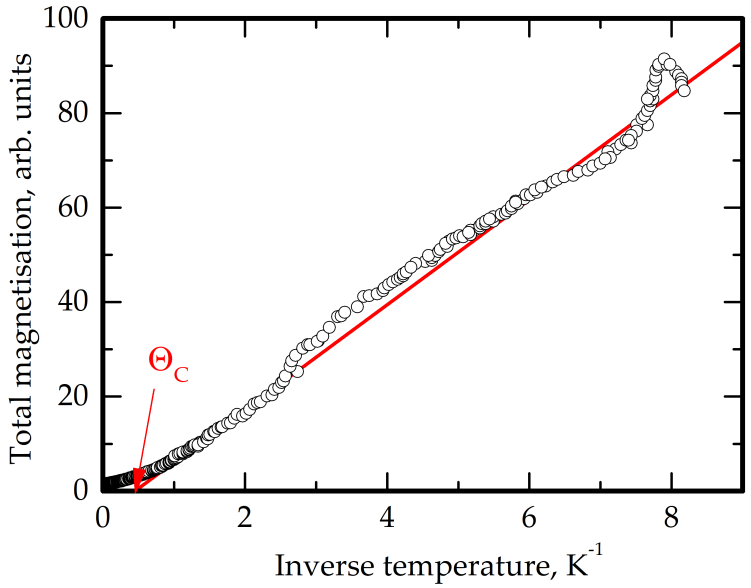

FIGURE 2.18: The identical dataset as in Figure 2.17 plotted with inverse temperature. The Curie Weiss law $\sim 1/T$ dependence of magnetisation is clearly valid for the intermediate temperature range. The Curie Weiss constant Θ_C can be estimated by extrapolation to 0. At high temperatures the curve deviates from the straight line as the Fermi liquid contribution to total magnetisation becomes larger than diminishing Curie Weiss solid contribution. At low temperatures, the rise of magnetisation is probably an artefact of measurement as explained in the text. However, the sudden decrease in magnetisation at the lowest of temperatures can not be assigned to measurement artefacts and hints towards possible anti-ferromagnetic ordering within the solid.

Chapter 3

Refrigeration

This chapter addresses the refrigeration techniques that are used for the work presented in this thesis. Only a brief overview will be given as descriptions of these techniques as well as their technical realisation are readily available in the literature [11, 48].

3.1 Dilution refrigeration

Dilution refrigeration has been very successfully and extensively used in low temperature physics as it is the only continuous cooling technique to cool down below 0.3 K. The principle of operation is based on the spontaneous phase separation of a ^{3}He-^{4}He mixture to form a ^{3}He-rich phase (the concentrated phase - almost pure ^{3}He) and a ^{3}He-poor phase (the dilute phase - only 6 % of ^{3}He). This separation occurs at around 870 mK and is present to the lowest temperatures. ^{3}He gas can be preferentially extracted by continuous pumping on a dilute liquid-gas phase boundary at a temperature of about 0.5 K by a pump. This is most commonly done by a pump external to the cryostat at room temperature [49], though internal cryopumping can also be implemented [50]. The ^{3}He can thus be re-liquefied and reintroduced to the concentrated phase, creating a non-equilibrium concentration across the phase boundary. As the entropy of the dilute phase is

larger than that of the pure phase, any ^{3}He moving across the phase boundary into the dilute phase, driven by the non-equilibrium concentration gradient, creates entropy. As described by the second law of thermodynamics, this requires heat $\Delta Q = T\Delta S$. The heat ΔQ needed for this dilution, is the useful power of the refrigerator.

The dilution refrigerator is used to precool the nuclear demagnetisation stage, Section 3.2, down to about 7 mK (further precooling, though possible, would require unreasonably long waiting times). After reaching the base temperature, the demagnetisation unit is thermally disconnected from the dilution unit to allow further single-shot cooling down to the μK temperature region. The description of the dilution refrigerator used for this experiment can be found in [51].

3.2 Adiabatic nuclear demagnetization

To cool down further than about 2 mK made possible by the state of the art dilution refrigerators, adiabatic nuclear demagnetisation is often used. In our case, as well as in many others, copper is used as the refrigerant to be demagnetised. Many other materials with nuclear magnetic moment could be used, for example $PrNi_5$ [52, 53]. Nevertheless, copper is readily available, pure, easy to work with and relatively inexpensive. Moreover, in the solid form copper has low internal magnetic field. In case of a fine copper powder this field increases significantly, though this can be beneficial in certain applications as discussed in Section 6.1.

Similarly to Section 2.3 we start with the partition function Z. For a nucleus with magnetic moment I there are $2I + 1$ sub-states labelled m, where $m = I, I-1, \ldots -I$. The partition function is then

$$Z = \sum_{m=-I}^{I} \exp\left(-\varepsilon_m / k_B T\right) \ . \tag{3.1}$$

The entropy S of such system can be again derived using (2.26) and we obtain a similar result as for the two level system in (2.29)

$$S = n\left[k_{\mathrm{B}} \ln\left(2I+1\right) - \frac{\lambda_n B^2}{2\mu_0 T^2}\right] , \tag{3.2}$$

where n is number of moles and λ_n is molar nuclear Curie constant

$$\lambda_n = \frac{N_{\mathrm{A}} I(I+1)\mu_0 \mu_N^2 g^2}{3k_{\mathrm{B}}} . \tag{3.3}$$

For copper the situation is slightly more complicated since there are two stable isotopes ^{63}Cu and ^{65}Cu with relative abundances of 69 % and 31 % respectively. Both have $I = 3/2$ and thus 4 non-equally populated energy levels. However, the principle outlined here stays the same. We can plot the dependence of entropy on temperature in high and low magnetic field using (3.2) as in Figure 3.1. The total entropy needs to be adequately averaged with respect to the population of both isotopes and all energy levels. The line from point A to B represents precooling in high magnetic field, in

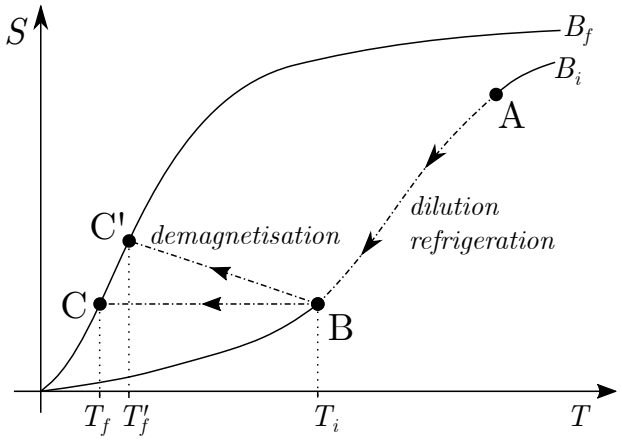

FIGURE 3.1: A schematic representation of a path followed during precooling and demagnetisation. Copper refrigerant is precooled with the dilution refrigerator in high magnetic field B_i (path A→B) until the base temperature T_i is reached. Subsequently, the thermal connection with the dilution unit is broken and the field is reduced from B_i to B_f, following the path B→C and reaching T_f. However, the process of demagnetisation is not ideal so realistically the sample reaches the point C′ at a slightly elevated temperature T_f'.

our case by dilution refrigeration. At point B the demagnetisation stage is

thermally disconnected from the dilution refrigerator via a superconducting heat switch and the magnetic field is slowly reduced. In a system with no external heat leak and very slow magnetic field change, the increase of entropy would be very small and temperature T_f would be reached. However, in real life, the external heat leak causes system to follow the path $B \rightarrow$C′ with final temperature $T_f' > T_f$.

From (3.2) it is evident that if the system is isolated and entropy is kept constant, the temperature must decrease proportionally with decreasing magnetic field and we come to a simple equation

$$T_f = T_i \frac{B_f}{B_i} \,. \tag{3.4}$$

This suggests that if we demagnetise to zero final field, the final temperature would also be zero, thus violating the second law of thermodynamics. The field is actually a superposition of the external magnetic field B and internal interaction magnetic field from the neighbouring nuclei B' (around 0.3 mT for copper).

$$T_f = T_i \cdot \frac{\sqrt{B_f^2 + B'^2}}{\sqrt{B_i^2 + B'^2}} \,. \tag{3.5}$$

The situation is similar to the effective field in the Curie-Weiss model described in Section 2.3.1.

The initial field in our case is 8 T and we demagnetise down to about 30 mT, which is the magnetic field required for NMR measurements at our designed frequency of 1 MHz. This should result in the reduction of temperature by a factor of 260, but in reality this is lower. Equation (3.5) assumes the refrigerant is always in thermal equilibrium with ^{3}He and that there is no external heat leak into the system, which is naturally not the case. To get at least close to the internal thermal equilibrium the rate of change of magnetic field should be kept low and thus the demagnetisation is usually carried out on a timescale of several hours overnight. Moreover, one can not neglect the entropy of the ^{3}He itself, with $S_{He} \propto T$. The proportionality

in (3.2) becomes

$$S \propto \frac{B^2}{T^2} + T \ , \tag{3.6}$$

agreeing with the line B→C′ in Figure 3.1. The low rate of change also reduces losses by eddy currents induced in copper which manifest as a heat leak with $\dot{Q} \propto \dot{B}^2$.

In our experiment the copper demagnetisation is used to precool the aerogel sample with a layer of solid ^{3}He with local initial magnetic field of 150 mT. This field will be reduced to 30 mT cooling the sample further. There is no need for a heat switch at this stage, because quasiparticle conductance rapidly drops below 140 µK and thus the heat contact with copper quickly becomes negligible. The aerogel demagnetisation stage is discussed in more detail in Chapter 6.

Chapter 4

Mechanical Oscillators

Mechanical oscillators serve as our primary tool in ^{3}He experiments, not only to measure the temperature of the superfluid. Conventional resistance thermometers are inaccurate at microkelvin temperatures due to the large thermal boundary resistance between the fluid and the thermometer in addition to significant self-heating. The method of probing the superfluid directly by measuring the damping of a mechanical oscillator has proven to be a superb tool at ultralow temperatures thanks to the elimination of thermalisation problems as well as having a relatively low heat load.

The standard vibrating devices present in the experiments described in this thesis are Vibrating Wire Resonators (VWR) and Quartz Tuning Forks (QTF). This chapter describes the basic principles of their operation and the underlying mechanism of the fluid damping.

4.1 Oscillator fundamentals

An oscillating device can be modelled as a simple mass m_0 on a spring with spring constant k driven at angular velocity ω by a periodic force $F = F_0 e^{i\omega t}$. The mass also experiences a restoring force $-\omega_0^2 x$ coming from the spring and a damping force $-\lambda \dot{x}$ from the fluid. Note that we assume a damping force that is linearly dependent on the velocity, which is true for

low velocities. For such a system we can write an equation of motion

$$m_0\ddot{x} + \lambda\dot{x} + m_0\omega_0^2 x = F_0 e^{i\omega t} \,, \tag{4.1}$$

where ω_0 is the natural frequency of the oscillator

$$\omega_0 = \sqrt{\frac{k}{m_0}} \,. \tag{4.2}$$

In the case of an oscillator submersed in a fluid, the damping term λ is not sufficient to describe all fluid effects. Extra mass m_0' is added to the mass of the oscillator m_0 to take into account the fluid dragged by the oscillator as well as the effect of the backflow around it

$$m = m_0 + m_0' \,. \tag{4.3}$$

Naturally, we expect harmonic motion for the velocity

$$\dot{x} = \dot{x}_0 e^{i\omega t} \,. \tag{4.4}$$

We can substitute this particular solution into the equation of motion (4.1), solve for $\dot{x}_0$ and obtain a complex Lorentzian function for the velocity amplitude

$$\dot{x}_0 = \frac{F_0 i\omega}{-\omega^2 m + i\omega\lambda + k} \,, \tag{4.5}$$

which can be split into real and imaginary components with $\mathrm{Re}(\dot{x}_0)$ being the in-phase velocity of the object

$$\mathrm{Re}(\dot{x}_0) = \frac{F_0\omega^2\lambda}{\omega^2\lambda^2 + \left(\omega^2 m - k\right)^2} \,, \tag{4.6a}$$

$$\mathrm{Im}(\dot{x}_0) = \frac{F_0\omega\left(k - \omega^2 m\right)}{\omega^2\lambda^2 + \left(\omega^2 m - k\right)^2} \,. \tag{4.6b}$$

The frequency dependence of both components is plotted in Figure 4.1. At resonance, the velocity of the oscillator is maximum and $\mathrm{Re}(\dot{x}_0)$ will

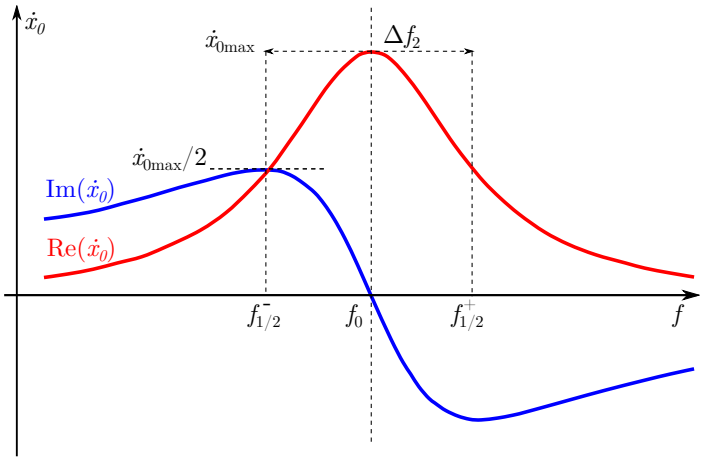

FIGURE 4.1: Frequency dependence of real (red) and imaginary (blue) components of velocity around resonance.

reach its maximum value. The condition

$$\omega^2 m - k = 0 \,, \tag{4.7}$$

must apply, leading to a resonance frequency

$$\omega' = \sqrt{\frac{k}{m}} = \sqrt{\frac{k}{m_0 + m_0'}} \,. \tag{4.8}$$

Moreover, at maximum when $\omega^2 m - k = 0$ we get

$$\mathrm{Re}(\dot{x}_0) = \frac{F_0}{\lambda} \,. \tag{4.9}$$

The shift in frequency from an oscillator in vacuum to the one damped by liquid is then

$$\Delta f_1 = \frac{\omega - \omega'}{2\pi} = \frac{1}{2\pi}\left(\sqrt{\frac{k}{m_0}} - \sqrt{\frac{k}{m_0 + m_0'}}\right) \,. \tag{4.10}$$

The imaginary component of velocity reaches a maximum when $\mathrm{Re}(\dot{x}_0)$ is at half of its maximum value. This occurs at a frequency $\omega_{1/2}$, which can be found by solving

$$\omega_{1/2}^2 \lambda^2 + \left(\omega_{1/2}^2 m - k\right)^2 = 0 \,, \tag{4.11}$$

The width of resonance at half height is then the difference between the two roots of the quadratic equation (4.11),

$$\Delta f_2 = \frac{\omega_{1/2}^{+} - \omega_{1/2}^{-}}{2\pi} = \frac{\lambda}{2\pi m} \,. \tag{4.12}$$

Substituting into (4.9) and realizing that $\max\left[\mathrm{Re}(\dot{x}_0)\right]$ is the velocity at maximum resonance v_0, we get

$$\Delta f_2 = \frac{F_0}{2\pi v_0 m} = \frac{F_0}{2\pi v_0 \left(m_0 + m_0'\right)} \,. \tag{4.13}$$

For the steadily driven oscillator such as our case, the rate of energy loss relative to the stored energy in the oscillator is described by the Q factor, often called the 'quality' of the resonance

$$Q = \frac{f_0}{\Delta f_2} \,. \tag{4.14}$$

Lower the energy dissipation, higher the Q factor and longer longer the ring down time of the oscillator.

Lastly, we introduce a useful fundamental property of the resonance called 'Height times Width over Drive' (HWD). The value is independent of temperature and represents the area under the resonance curve. It is often used to describe the 'strength' of the resonance

$$\mathrm{HWD} = \frac{v_0 \Delta f_2}{F_0} = \frac{1}{2\pi m} \,. \tag{4.15}$$

4.2 Vibrating wire resonators

One of the most simple resonators to make is a vibrating wire. The device is sensitive down to $\sim 100\,\mu\mathrm{K}$ in ^{3}He [54] and has been used extensively by the Lancaster Group [40, 55, 56]. The resonator consists of a superconducting wire bent to form a semicircular loop with both ends firmly glued to a base plate. A constant magnetic field $\boldsymbol{B}$ is applied perpendicular to the plane of the wire. The wire resonates when alternating current is applied at a

frequency corresponding to the natural frequency of the loop due to the electromagnetic force

$$\boldsymbol{F} = \boldsymbol{B} \times \boldsymbol{I} \cdot D \,, \tag{4.16}$$

where D is the spacing between the legs of the wire and $\boldsymbol{I}$ is the driving current

$$I = I_0 e^{i\omega t} \,. \tag{4.17}$$

The motion of the wire is detected through the induced Faraday voltage

$$V = \frac{\mathrm{d}\left(\boldsymbol{B} \cdot \boldsymbol{A}\right)}{\mathrm{d}t} \,, \tag{4.18}$$

where the area of the semi-circular loops is $A = \pi D^2/8$ and the angular frequency of the wire is $\omega = 2\dot{x}^2/D$. The rate of change of the area is naturally $A\omega$. The magnetic field is static along the $\hat{\boldsymbol{z}}$-axis, so the induced voltage is given as

$$V = \frac{\pi}{4} B D \dot{x} \,. \tag{4.19}$$

Combining (4.13), (4.16) and (4.19), the HWD parameter of the VWR can be obtained

$$\mathrm{HWD}_{\mathrm{VWR}} = \frac{V_0 \Delta f_2}{I_0} = \frac{B^2 D^2}{8m} \,. \tag{4.20}$$

4.3 Quartz tuning forks

Another widely used [57–59] resonator is the quartz tuning fork (QTF). Unlike the VWR, forks do not require an external magnetic field to operate. The QTF is like a regular tuning fork but much smaller and made from a single quartz crystal wafer. Quartz is a piezoelectric material, so when the fork is driven by an alternating potential, the potential difference causes a stress. This stress leads to charge separation and an alternating current proportional to the time derivative of the displacement is induced

$$I = a\dot{x} \,, \tag{4.21}$$

with a proportionality constant a, named the fork constant. At resonance, the response of the force to the driving voltage as

$$F_0 = \frac{aV_0}{2} , \tag{4.22}$$

where the coefficient $1/2$ is a convention taking into account that the dissipation comes from both legs of the fork. In contrast to a VWR, the driving force of the QTF is expressed in terms of voltage V and the displacement in terms of induced current I. We can express the tuning fork HWD parameter using the values of current and voltage at resonance as

$$\mathrm{HWD_{TF}} = \frac{I_0 \Delta f_2}{V_0} . \tag{4.23}$$

Inserting (4.13), (4.21) and (4.22) we can express the $\mathrm{HWD_{TF}}$ in terms of fork constant a and the effective mass

$$\mathrm{HWD_{TF}} = \frac{a^2}{4\pi \left(m_0 + m_0'\right)} . \tag{4.24}$$

Blaauwgeers et. al. [59] derived the effective mass of one leg in vacuum as

$$m_0 = 0.24267 \rho_\mathrm{q} \mathcal{L}\mathcal{W}\mathcal{T} , \tag{4.25}$$

where $\mathcal{L}$, $\mathcal{W}$ and $\mathcal{T}$ are fork dimensions shown in Figure 4.2 and ρ_q is the density of quartz ($\rho_\mathrm{q} = 2.659\,\mathrm{g/cm^3}$).

4.4 Damping of the oscillators

Now, after descriptions of the mechanical objects, the fluid contribution can be introduced. The fluid damping of ^{3}He can be described in two different limiting regimes. First, the hydrodynamic regime, apparent at higher temperatures, is a mixture of normal ^{3}He viscous and hydrodynamic damping. This description is successful both in the normal phase of ^{3}He and, using

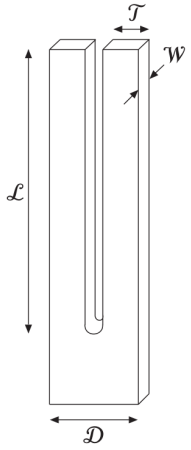

FIGURE 4.2: Tuning fork dimensions. Figure taken from [59].

the two fluid approach, in the high temperature superfluid B-phase of ^{3}He, although corrections for finite mean free path effects are necessary [60].

Below 0.3 T_c, damping can no longer be described in terms of local parameters such as viscosity and one enters the ballistic regime. Here the system is modelled as dilute gas of quasiparticles interacting with the oscillator. The following sections briefly describe both regimes.

4.4.1 Hydrodynamic regime

When the oscillator is immersed in a fluid, the resonant frequency decreases from the vacuum value $f_{0\mathrm{vac}}$, while the width of the resonance increases from the vacuum value $\Delta f_{2\mathrm{vac}}$. The effect can be described in terms of the oscillator mass enhancement with two contributions: fluid backflow around the moving object and viscous drag. We recall the effective mass from (4.3)

$$m = m_0 + m_0' = m_0 + \beta \rho_{\mathrm{He}} V + B \rho_{\mathrm{nf}} S \delta \,, \tag{4.26}$$

where ρ_{He} is the density of helium, ρ_{nf} is normal fluid density, S is the surface area of the oscillator, β and B are the geometrical factors of order of unity [61], and δ is the viscous penetration depth, describing the thickness of the fluid layer which is affected by the oscillator motion [62]. The fluid velocity exponentially decreases with distance x away from a moving object

with velocity v_0 as

$$v(x) = v_0 e^{-x/\delta}. \tag{4.27}$$

The momentum clamped to the oscillator can be expressed as

$$p = \int_0^\infty \rho v(x)\, \mathrm{d}x = \rho v_0 \delta \ . \tag{4.28}$$

The penetration depth is given by

$$\delta = \sqrt{\frac{\eta}{\pi f \rho_{\mathrm{nf}}}} \ . \tag{4.29}$$

4.4.2 Ballistic regime

At temperatures below $0.3\, T_c$, the mean free path of quasiparticles exceeds the cell dimensions. This ballistic limit means we have to model the system as a dilute gas of quasiparticles interacting with the oscillator.

Imagine a paddle with surface area A being dragged through this gas of n quasiparticles, each moving at group velocity v_g with Fermi momentum p_{F}. The paddle will experience a drag force F in the opposite direction to its velocity. On a reflection, each quasiparticle exchanges momentum $2p_{\mathrm{F}}$ with the paddle. The drag force can then be calculated from the difference in the total rate of momentum exchange between the front and back side of the paddle

$$F = \dot{p}_{\mathrm{front}} - \dot{p}_{\mathrm{back}} = \frac{1}{2} A \left\langle n \left(v_g + v \right) \right\rangle 2p_{\mathrm{F}} - \frac{1}{2} A \left\langle n \left(v_g - v \right) \right\rangle 2p_{\mathrm{F}} = 2Anvp_{\mathrm{F}} \ , \tag{4.30}$$

where v is the velocity of the paddle. However, the calculations deviate from experiment significantly. In reality the paddle experiences a force 3 orders of magnitude larger than that of the equation (4.30). It is apparent that a more complex mechanism takes place.

Our simple kinetic argument neglects the superfluid velocity field around the moving paddle. As the paddle moves, there will be some liquid moving together with it at the close proximity of the paddle. The liquid far away

from the paddle will be at rest with the container walls. We can perform a Galilean transformation from this reference frame, where a quasiparticle with group velocity v_g becomes $v_g + v$ in the proximity of the paddle. The stationary dispersion diagram shown in Figure 2.3 will modify, since all the states gain energy $p_F v$ as shown in Figure 4.3 [63].

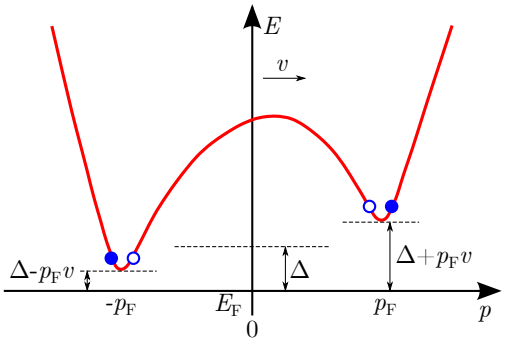

FIGURE 4.3: Dispersion curve for the fluid moving with velocity v in the reference frame of the bulk superfluid.

The simple scattering process described previously is still valid between the moving fluid and the paddle since in their frame of reference they are both stationary. The collision of quasiparticles with the paddle is elastic, exchanging momentum $2p_F$ with the paddle. Both holes and excitations can keep their character after scattering, since there are states available with opposite momentum.

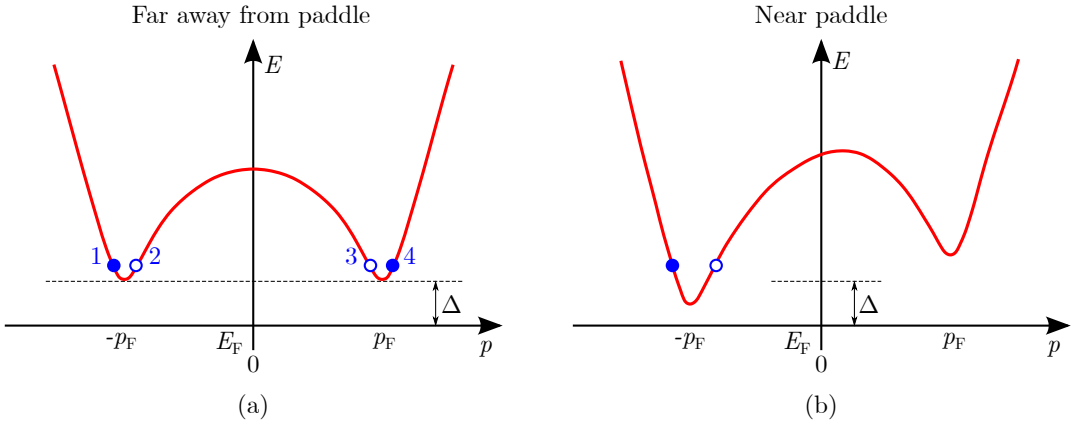

FIGURE 4.4: Dispersion curves of the superfluid (a) away from and (b) near the paddle. The bulk states away from the paddle from the $-p$ side of the dispersion curve are free to enter the moving superfluid near the paddle surface. The distant states from the $+p$ side must be retro-reflected back into the bulk.

The situation is different in between the stationary and the moving fluid as shown in Figure 4.4. The quasiparticle 1 and the quasihole 2 coming from bulk superfluid are free to enter the moving superfluid as there are states available. These quasiparticles can then scatter from the paddle as described previously. Quasiparticle 3 and quasihole 4 however can not enter the moving superfluid as there are no states available with their energy and momentum. Quasiparticle 4 can only be retro-reflected back, but since its energy must be converted, it will be reflected as a quasihole with the almost exact opposite momentum. The same principle in reverse applies for a quasihole 3. Note that there is a momentum difference between 3 and 4 as shown in Figure 4.4, but this effect is negligible compared to the momentum exchange with the paddle $2p_{\mathrm{F}}$. The retro-reflection of an opposite type of excitation is called *Andreev reflection* with analogy to a similar process on the boundary between normal state material and a superconductor.

The imbalance caused by only some particles being able to scatter on the paddle is the cause of the increased damping. Excitations travelling towards the front of the paddle are free to scatter with it and exchange momentum. On the other hand, holes in front of the wire must be Andreev-reflected becoming quasiparticles with very little momentum exchange. Similarly, quasiparticles behind the wire get Andreev-reflected while holes are free to scatter. The normal small imbalance between the momentum transfers from quasiparticles (or quasiholes) in front and behind the moving object is no longer possible, leading to the enhanced damping.

We can quantify this damping the force by calculating the force per unit area of each branch of the dispersion curve. For branches 1 and 2 all the quasiparticles are free to scatter from the paddle, thus we can write the force per unit area as

$$F_{1,2} = 2p_{\mathrm{F}} \left\langle n v_g \right\rangle \ , \tag{4.31}$$

where $\left\langle n v_g \right\rangle$ is the average quasiparticle flux derived in (2.13)

$$F_{1,2} = 2p_{\mathrm{F}} g(p_F) k_{\mathrm{B}} T e^{-\Delta/k_{\mathrm{B}}T} \ . \tag{4.32}$$

In the case of branches 3 and 4, only the excitations with energies above $\Delta + p_F v$ are able to reach the paddle. We can no longer simply use $\langle n v_g \rangle$ but instead

$$F_{3,4} = -2p_F g(p_F) \int_{\Delta + p_F v}^{\infty} e^{-E/k_B T} \, \mathrm{d}E = -2p_F \langle n v_g \rangle e^{-p_F v / k_B T} \, . \tag{4.33}$$

The force responsible for the damping is naturally the sum of the force contributions

$$\begin{aligned} F &= F_{1,2} + F_{3,4} \\ &= 2p_F \langle n v_g \rangle - 2p_F \langle n v_g \rangle e^{-p_F v / k_B T} \\ &= 2p_F \langle n v_g \rangle \left[1 - e^{-p_F v / k_B T} \right] \, . \end{aligned} \tag{4.34}$$

For low velocities, we can use the Taylor series for e^x and obtain

$$F = 2p_F \langle n v_g \rangle \frac{p_F v}{k_B T} \tag{4.35}$$

while at large velocities the damping force is constant

$$F = 2p_F \langle n v_g \rangle \, . \tag{4.36}$$

4.4.2.1 Thermometry in ballistic regime

In practice, measurements fulfil the low velocity criterion. Our derivation of the drag force on the paddle was limited to one dimension. Now, to include the geometry of the object and the behaviour of the flow around it, an extra proportionality constant γ on the order of unity is introduced

$$F = 2A\gamma \langle n v_g \rangle \frac{p_F^2 v}{k_B T} \, . \tag{4.37}$$

Recalling the equation of motion of a driven damped harmonic oscillator (4.1), the term $-\lambda v$ was used to describe the damping force. From the solution of this equation of motion the width at half height Δf_2 was shown

in (4.12) to be

$$\Delta f_2 = \frac{\lambda}{2\pi m} = \frac{F_{\text{damping}}}{2\pi m v} \,. \tag{4.38}$$

Substituting (4.37) we get

$$\Delta f_2 = \gamma' \frac{p_F^2 \langle n v_g \rangle}{k_B T \left(m_0 + m_0'\right)} \,, \tag{4.39}$$

where γ' is a combination of multiple previous geometrical constants

$$\gamma' = A\gamma\lambda\pi \,. \tag{4.40}$$

The pre factor γ' is very difficult to measure directly, because the damping force is changing dramatically with temperature and any small uncertainty in the temperature scale gives rise to great uncertainty in γ'. Based on bolometer measurements [64] it was estimated as $\gamma' = 0.28$ for a 4.5 µm thick vibrating wire. Calibrating against such a wire, γ' was found to be 0.62 for a 32 kHz quartz tuning fork [5].

Expressing the quasiparticle flux as in (2.13) we obtain

$$\Delta f_2 = \gamma' \frac{p_F^2 g(p_F)}{\left(m_0 + m_0'\right)} e^{-\Delta/k_B T} \,. \tag{4.41}$$

It is convenient now to gather all the parameters that do not depend on temperature into a new constant

$$\gamma'' = \frac{\gamma' p_F^2 g(p_F)}{m_0 + m_0'} = \frac{\gamma' p_F^2 g(p_F)}{m} \,. \tag{4.42}$$

The model is almost complete, but we must not forget the intrinsic damping arising from internal mechanical losses in the wire or quartz. This damping is always present and in principle it can be measured in vacuum when no other damping is present. In practice however, we often use the value when immersed in superfluid when $T \to 0$ as at the lowest achievable temperatures the other damping contributions are small. The internal

mechanical losses add an extra intrinsic width component into (4.41) as

$$\Delta f_2 = \Delta f_{2\text{vac}} + \gamma'' e^{-\Delta / k_\text{B} T} \ . \tag{4.43}$$

Rearranging for T we get to the final expression to estimate temperature from the measured width at half height

$$T = \frac{\Delta}{k_\text{B} \ln\left(\frac{\gamma''}{\Delta f_2 - f_{0\text{vac}}}\right)} \ . \tag{4.44}$$

In this derivation we did not include damping caused by the acoustic emission. The acoustic damping is present, however in our frequency rang the effect is very small and can easily be neglected.

4.4.2.2 Width parameter

Because the change in resonant width of the oscillator $\delta\Delta f_2$ depends on temperature, when comparing power at different temperatures it is of more appropriate to use the quantity called the width parameter W [65]

$$W = \delta\Delta f_2 \cdot T \cdot (\Delta_0 + k_\text{B} T) \ . \tag{4.45}$$

For a steady state, the width parameter is proportional to the dissipated power in the volume of a bolometer.

4.5 Velocity enhancement factor

The flow of any object through a fluid creates a flow pattern with a certain velocity profile which strongly influences the drag force. Flow patterns are governed by the object's geometry, and in case of our oscillators assuming a simple infinitely long smooth cylinder is sufficient for most applications. The full potential flow derivation from Navier Stokes equations for incompressible, non-viscous fluid can be found in any fluid dynamics handbook [66], and the resulting flow pattern is shown in Figure 4.5. The moving

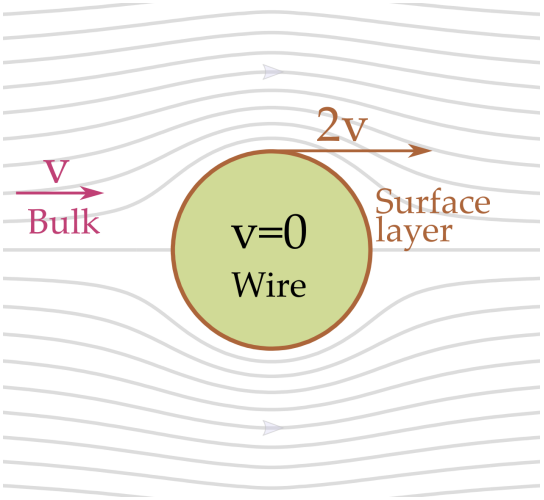

FIGURE 4.5: Potential flow of non-viscous fluid around a cylinder in a moving frame of reference. Note the points of maximum flow velocity in the surface layer.

frame of reference is used in which the cylinder is stationary and the fluid far from the cylinder moves at velocity v. The figure shows that the velocity profile along the surface layer of the cylinder is not homogeneous. The maximum velocity is reached in the plane perpendicular to the flow and crosses the middle of the cylinder with $v_{max} = 2v$. This point of maximum velocity is important because it dominates the dissipation processes as we will see in Section 5.

4.6 Circuit diagrams

The electrical circuit diagram necessary to measure a vibrating wire is shown in Figure 4.6. The input AC signal comes from an Agilent Technologies 33220 signal generator. In the case of VWRs, the generator is connected to a home made 'drive box'. The box consists of series of resistors (1 MΩ, 100 kΩ, 10 kΩ, 1 kΩ and 100 Ω) to vary the drive current. Moreover, there is a fixed 6:1 step-down transformer to break earth loops and reduce the drive voltage. The signal then travels to the device after which, with the exception of tantalum wires, the induced electromagnetic field is amplified by a 30:1 step-up transformer on the 4 K plate. The signal is detected by a Stanford

Instruments SR830 phase sensitive lock-in amplifier synchronised with the generator.

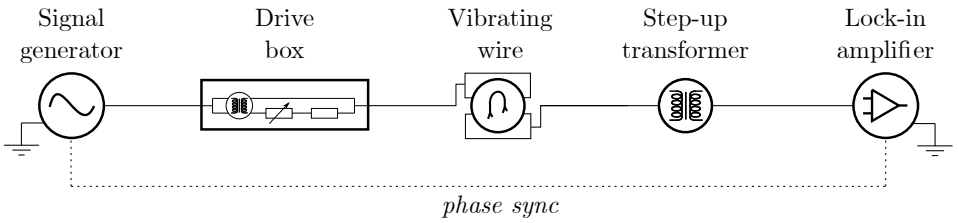

FIGURE 4.6: Simplified electrical circuit schematic of a typical vibrating wire resonator.

The QTF setup is quite similar to that of the VWR, see Figure 4.7. The signal from the generator is attenuated at room temperature by a 60 dB or 80 dB attenuator, depending on the desired drive amplitude. The resulting current is amplified and converted to voltage at room temperature by a Stanford Instruments SR570 high bandwidth current pre-amplifier. Similarly to VWRs, the amplified signal goes to a lock-in amplifier phase-locked with the generator.

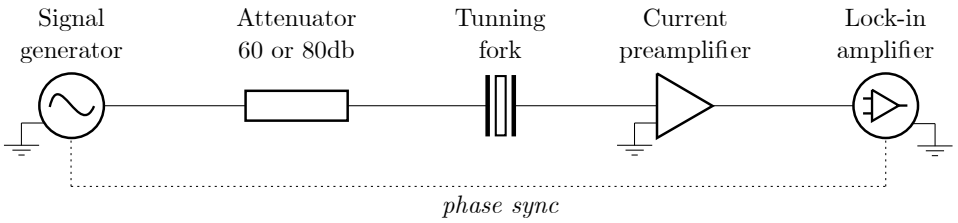

FIGURE 4.7: Simplified electrical circuit diagram of quartz tuning fork.

The wiring down the cryostat differs depending on the device. Generally, tuning forks are more sensitive to noise and stray capacitances, thus coaxial cables with the outer shield grounded are used down to mixing chamber plate. From there, the coaxial cable is changed for a pair of superconducting wires twisted together. One is grounded while the other carries the signal. For the top tuning fork (see Section 6.2), superconducting leads twisted together were used to reduce the number of required coaxial lines, since the sensitivity of this probe was already reduced due to an unexpectedly large resonance width. VWR's generally do not require the use of

coaxial cables for wiring inside the cryostat, so twisted pairs of superconducting wires are used instead.

4.7 Modes of operation

The oscillating objects can be measured in various ways depending on the level of accuracy required and the acquisition time. The following section describes the three most common modes of operation and shows their pros and cons.

4.7.1 Frequency sweeps

The frequency sweep is the most often used mode of operation of the mechanical oscillator. The frequency of the alternating current is changed while its amplitude is held constant. Plotting the induced signal one obtains the Lorentzian shape of the resonance similar to that shown in Figure 4.1. Resonance parameters such as resonant frequency, width at half height and the height of the resonance are obtained by fitting the in-phase and out-of-phase curves. The HWD of the drive is then calculated and stored. The non-resonant background signals (from capacitive/inductive coupling and crosstalk) are also determined from the fits. The background signals are usually remeasured in zero magnetic field at the end of the demagnetisation cycle for more accurate post-run analysis and thermometry. A LabVIEW^{TM} data acquisition program controls the sweep, the acquisition and real-time analysis of the sweep. This program processes the curves, stores the parameters and uses them in feedback to adjust the next sweep. In order to get an accurate fit, the range of the sweep should not be smaller than about three times the width of resonance. Around 200 points per sweep is usually sufficient for a good fit. The time between each point of the sweep is set to be no shorter than the intrinsic response time of the oscillator τ in order to avoid ringing

$$\tau = \frac{1}{\pi \Delta f_2} \, . \tag{4.46}$$

Ideally, waiting times per point as long as 3τ to 5τ are preferable. As mentioned earlier in Section 4.1, the τ is proportional to the the Q factor of resonance

$$\tau = \frac{Q}{\pi f_0} \,. \tag{4.47}$$

4.7.2 Amplitude sweeps

Once the resonant frequency is known, an amplitude sweep can be performed. During such a sweep, the amplitude of the driving signal is changed and the response of the device is recorded. The driving signal is kept at the resonant frequency of the device during the sweep. This is done by minimizing the ratio of the out-of-phase to in-phase components of the signal. This procedure requires good knowledge of the non-resonant background, which must be obtained beforehand with the previously mentioned off-resonance frequency sweeps in zero magnetic field.

Figure 4.9 shows the typical curve obtained from an amplitude sweep of the tuning fork. Three distinct regimes are apparent. Firstly, at the lowest drives i.e. at lowest velocities, the damping of the oscillator increases linearly with velocity. Increasing the drive, the response of the wire becomes non-linear as it enters Andreev regime mentioned in Section 4.4.2. Lastly, above a certain drive amplitude corresponding to a critical velocity $v_c \approx 9\,\mathrm{mm\,s^{-1}}$ [67], the oscillator begins to break Cooper pairs surrounding the wire and the damping dramatically increases. The new damping arises because at v_c the dispersion curve in proximity of the oscillator is tilted enough (recall Figure 4.3) so that the Cooper pairs can break without any extra energy, see Figure 4.8.

- creating quasiparticles that scatter into the bulk superfluid. This is the so called Landau critical velocity v_L, predicted by Landau [1] already in the early days of forming superfluid helium theory. The mechanism of dissipation resulting in a critical velocity is the main focus of the experiments described in Section 5.

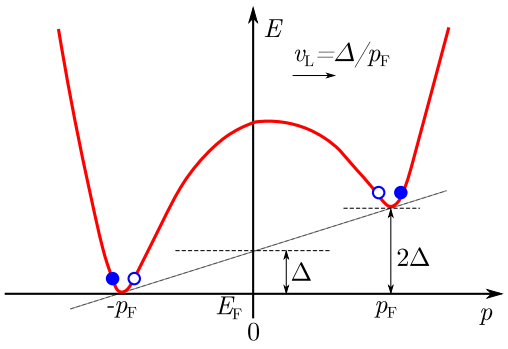

FIGURE 4.8: The dispersion curve for the fluid moving at Landau critical velocity v_L.

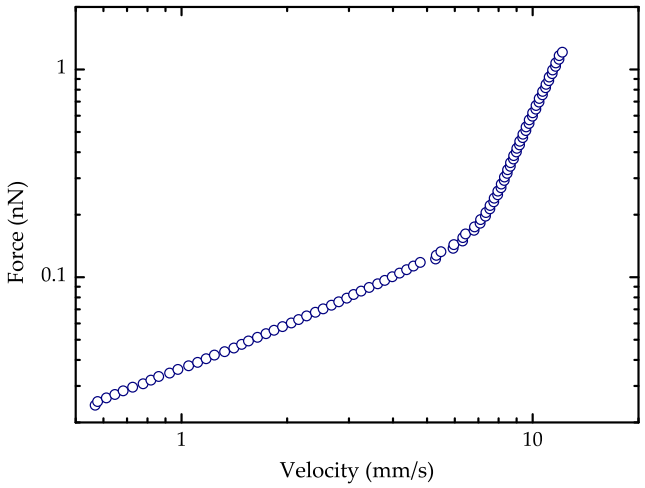

FIGURE 4.9: An example of velocity dependence of a damping force for a quartz tuning fork.

4.7.3 Resonance tracking

Sweeping the full frequency range of the oscillator gives the most accurate measurement, but sometimes the properties of the fluid are changing too rapidly to be observed accurately with the slow full sweep. The resonance tracking technique is appropriate for these situations where the oscillator is driven at its resonant frequency with fixed amplitude and the parameters of the resonance are determined from the height of the signal. We can track the changing frequency with a similar feedback loop to the one used for amplitude sweeps. Readings can be taken at much faster rates with about one second per measurement compared to at least $\sim$ 60 s required for the full sweep [68]. However, similarly to the amplitude sweep, a well

characterised background signal is crucial for these measurements and post-run analysis is required.

Chapter 5

Floppy Wire Experiment

The Floppy Wire is a unique instrument allowing for uniform linear (DC) movement of a macroscopic object through superfluid ^{3}He for the very first time. The device is based on a method for moving a wire through solid ^{4}He pioneered by Berent and Polturak [69]. The Floppy Wire has been built in Lancaster [70] and has already produced unexpected discoveries when studying superfluid dissipation under DC motion [7]. A model explaining the observed anomalously small dissipation was proposed and the aim of the following experiments was to verify it.

This chapter first introduces the device and the means to achieve uniform linear motion. An overview of previous results with the device and an explanation of the proposed dissipation mechanism follows. The new experimental data on the frequency dependence of the dissipation as well as on the dissipation during various accelerations of the wire is shown and discussed in detail. The experiment with the driving the Floppy Wire at a higher frequency overtone is also mentioned, though the results are inconclusive.

5.1 Device

The Floppy Wire is essentially a VWR with much heavier mass and lower quality factor. Thanks to the larger size of this object, it allows for a large

range of motion and a variety of measurement modes described below.

The Floppy Wire is placed at the top of the inner cell of the 'Lancaster style' nuclear demagnetisation stage mentioned in Section 6.1 and is fully immersed in superfluid ^{3}He.

Unlike a traditional VWR, the Floppy Wire is goalpost-shaped and of much larger size, with a leg spacing of 9 mm and leg length of 25 mm. The wire itself is much thicker too: single-core NbTi wire with an outer diameter of 137 µm was used. Copper cladding and Formvar electric insulation surrounding the superconducting core was not removed in order to strengthen the wire as well as to increase its mass, decrease the resonant frequency and Q factor. $Q \simeq 5500$ was previously measured in vacuum at a temperature of a few mK [71], about two orders of magnitude lower than that of the standard quartz tuning fork [72].

As shown in Figure 5.1, a set of copper detection coils are wrapped around the outer cell on the same level as the wire's crossbar. The two coils are wound in the opposite direction. A small high frequency (96.4 kHz) probe signal added to the Floppy Wire drive current is then picked up by the coils. This signal has a frequency very far away from the resonance so it does not interfere with the motion measurements. The strength of the detection signal depends on the distance between the coils and the wire, and is used to determine the position of the wire inside the cell to an accuracy better than 0.5 mm. The detection coils also allow for determining the velocity of the wire by differentiation of the position, however poor signal to noise ratio of this method does not allow for accurate measurements. A less noisy signal can usually be obtained from measuring the induced voltage on the wire itself in the traditional manner discussed in Chapter 4. For this reason, in the experiments described in this chapter the detection coils were not used for anything else other than position calibration.

A schematic representation of the Floppy Wire electrical setup is shown in Figure 5.2. The setup shares similarities with the VWR setup shown in Figure 4.6, but is a little more complicated. The wiring can be split into

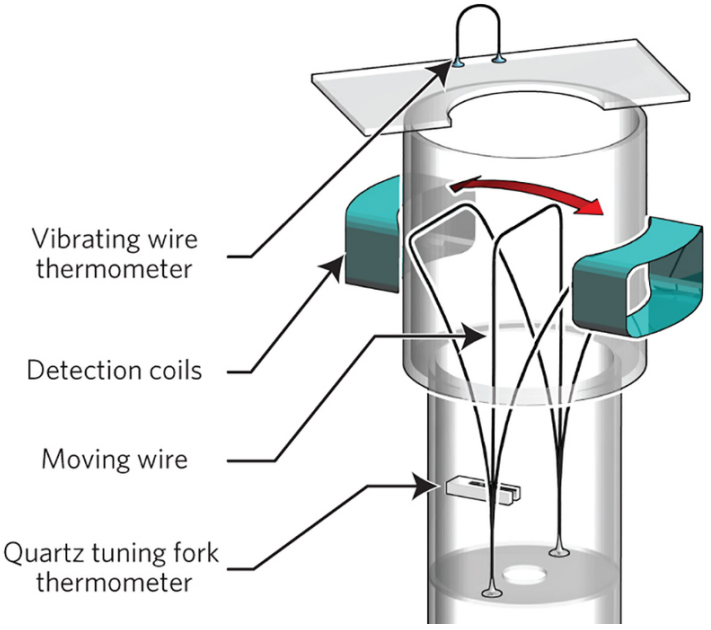

FIGURE 5.1: The Floppy Wire device and part of the experimental volume. The Floppy Wire is immersed in superfluid ^{3}He and placed in a magnetic field oriented along the vertical axis. A set of detection coils wrapped around the cell can detect the position of the wire with a generated emf. A quartz tuning fork and vibrating wire thermometers are placed in the vicinity of the wire and are used to measure the thermal response of the condensate.

two distinct parts. The first AC part used for frequency sweeps is almost identical with a VWR, with a signal generator feeding AC pulses through a drive box to the Floppy Wire. The wire response signal is measured with a phase synchronised lock-in amplifier directly, without a step-up transformer as in the case of a VWR. The step-down transformer present in the VWR drive box is also missing, as it is not necessary to reduce the signal strength. (Moreover, the very low resonant frequency of the Floppy Wire of about $\sim 66\,\mathrm{Hz}$ limits the use of transformers anyway.)

DC measurements are performed with a separate set of leads due to the higher currents required. The leads are copper down to the 4 K flange and superconductors below. This setup also allows for driving the Floppy Wire in AC mode around an equilibrium position other than 0 A corresponding to the middle of the cell. The AC signal from the low frequency signal generator can be simply added on top of the DC offset signal from the DC power supply.

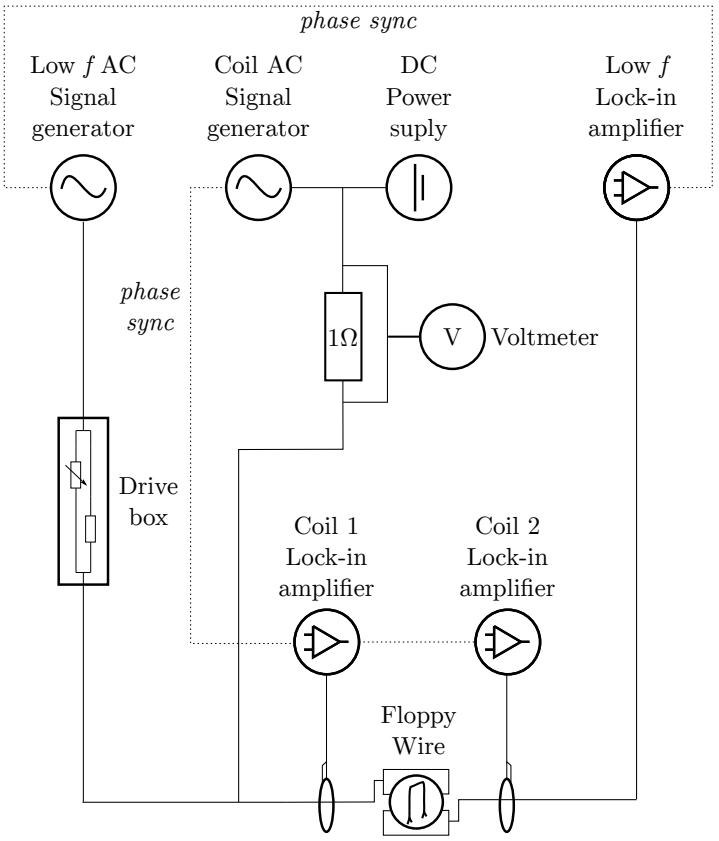

FIGURE 5.2: Simplified electrical circuit diagram of the Floppy Wire device.

Two thermometers in the vicinity of the Floppy Wire were used to determine the drag force exerted on it (the method is introduced in Section 5.3). Both thermometers are connected in a standard setup described in Section 4.6 with their output signals pre-amplified by the low noise current and voltage amplifiers (Stanford Instruments SR570 and SR560 respectively). The output of the lock-in amplifiers from the thermometers is measured by a fast data acquisition setup (DAQ) using a sample rate of 20 000 samples/s.

5.2 Uniform motion

Achieving uniform motion is crucial for the Floppy Wire experiments. Since the fluid damping is low, avoiding transient oscillations is not straightforward. The method used to drive the oscillator was originally developed by Dmitry Zmeev (also independently by Roch Schanen) to ensure uniform

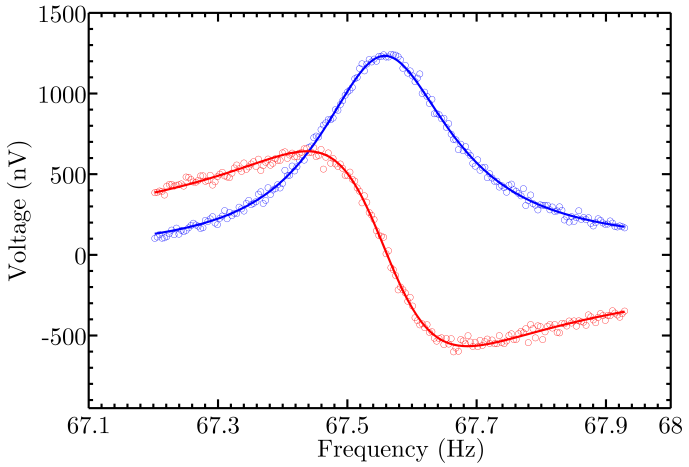

FIGURE 5.3: Floppy Wire frequency sweep around the fundamental mode of resonance at 173 µK in a magnetic field of 132 mT. The plot shows the in-phase and out-of-phase components of measured voltage. The full line shows fits of the Lorentzian curves to determine the characteristics of the resonance.

motion of a grid to generate turbulence in ^{4}He [73]. The same method can be applied to a Floppy Wire and is described in the following section.

5.2.1 Equation of motion

The Floppy Wire motion can be described by the equation of motion

$$F(t) = m\ddot{x}(t) + \lambda\dot{x}(t) + m\omega_{\text{vac}}^2 x(t) \ , \tag{5.1}$$

where F is the time-dependent driving force, λ is the damping term and ω_{vac} is the resonant frequency in vacuum. The force relates to a drive current I simply as

$$F = BIl \ , \tag{5.2}$$

where B is the intensity of the external magnetic field and l is the length of the Floppy Wire crossbar (9 mm).

A successful ramp is achieved when the Floppy Wire is moved from the initial equilibrium position to another equilibrium position at distance d at a uniform velocity v without any overshoot or transient oscillations. Previous efforts have shown that simply increasing the driving current I

linearly leads to strong oscillations [74]. The origin of such oscillations is in the discontinuity of the first and second derivatives of the driving force in the beginning and the end of the ramp pulse. Such oscillation can be strongly reduced by controlling the driving force so that $\ddot{x}(t)$ is smooth at all times.

We can illustrate the method on a simple ramp moving the Floppy Wire over distance d at constant velocity v. We choose the time dependence of position as follows

$$x(t) = \begin{cases} vt_{\text{acc}}(1 - \frac{t}{2t_{\text{acc}}})(\frac{t}{t_{\text{acc}}})^3, & 0 < t \leq t_{\text{acc}} \\ vt, & t_{\text{acc}} < t \leq t_3 - t_{\text{acc}} \\ d - vt_{\text{acc}}(1 - \frac{t}{2t_{\text{acc}}})(\frac{t}{t_{\text{acc}}})^3, & t_3 - t_{\text{acc}} < t \leq t_3\ , \end{cases} \tag{5.3}$$

where t_{acc} is the acceleration time to velocity v as well as the deceleration time to stop the Floppy Wire . The chosen $x(t)$ results in a parabolic and continuous acceleration profile $\ddot{x}(t) \sim t^2$. This profile shows no transient oscillations when driving a vibrating grid [73] and is just as effective for our case. The absence of oscillations is apparent on the emf signature of the Floppy Wire during a short burst pulse as shown in Figure 5.4b.

5.2.2 Fork constant calibration

In order to derive the force from measurements of the displacement $x(t)$, knowing the spring constant k of the Floppy Wire is necessary. First, we can calibrate the displacement by slowly increasing the DC drive current through the Floppy Wire and measuring the response of the pick-up coils as shown in Figure 5.4a. An emf is induced in the pickup coils due to the small high frequency signal added on top of the DC drive current. When the coil signal stops increasing the Floppy Wire has hit the cell wall and can move no further.

Alternatively, when an AC signal close to the resonant frequency is added to a DC offset, the Floppy Wire oscillates around its new equilibrium

position and its velocity can be estimated from the emf across the wire. On increasing the DC offset, once the cell wall is reached the emf vanishes as the Floppy Wire is no longer able to move, see Figure 5.4b. Both methods are consistent in determination of the touching voltage.

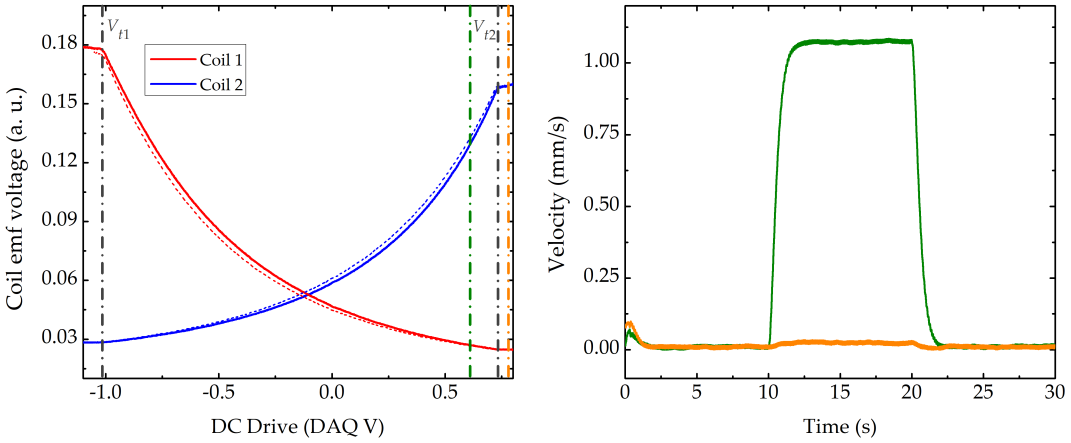

FIGURE 5.4: Calibration of the Floppy Wire wire position within the cell. a) The emf of the pickup coils as the wire is moved across the cell. When the emf stops increasing the cell wall was reached. b) Alternatively, the emf of the Floppy Wire wire directly related to its velocity can be measured. The plot shows the induced voltage at two positions near the wall and touching the the wall.

The process is repeated on both sides of the cell. Since the displacement of the top of the wire is small compared to the Floppy Wire's leg length, we assume it to be linear with applied current. Knowing the cell dimensions, the total distance between the both wall positions is $d = 12.1\,\mathrm{mm}$. The spring constant is then

$$k(B) = \frac{V_{t1} + V_{t2}}{d}\,, \tag{5.4}$$

where V_{t1} and V_{t2} are touching voltages shown in Figure 5.4a.

The calibration was performed at 80 mT (1 A in the main magnet, corresponding to $\mathrm{HWD}_0 = 5.025 \times 10^4\,\mathrm{nV\,Hz/mV}$ for the Floppy Wire resonance) leading to $k_0 = 0.29\,\mathrm{mm/V}$. The spring constant linearly depends on the magnetic field strength, thus for a different external field we write

$$k(B) = 0.29\,\mathrm{mm/V} \cdot \sqrt{\frac{\mathrm{HWD}(B)}{5.025 \times 10^4\,\mathrm{nV\,Hz/mV}}}\,. \tag{5.5}$$

This calibration was used for all the experiments in this work with the exception of Figure 5.7 which dates prior to this calibration.

5.2.3 Resulting driving force

We have introduced the desired profile of displacement as well as the estimation of the spring constant k. We can now rewrite the driving force from (5.1) in the form

$$F = k\,\frac{\ddot{x} + 2\pi\Delta f_2 \dot{x} + (2\pi f_0)^2\, x}{(2\pi f_0)^2}\,. \tag{5.6}$$

Before every set of ramps it is necessary to perform a Floppy Wire frequency sweep to determine the three temperature and magnetic field dependent parameters that influence the driving force: width of resonance Δf_2 and resonant frequency f_0 for the force equation (5.6) and the HWD parameter to determine spring constant in (5.5). An example of a calculated drive voltage together with the expected Floppy Wire position and velocity is shown in Figure 5.5.

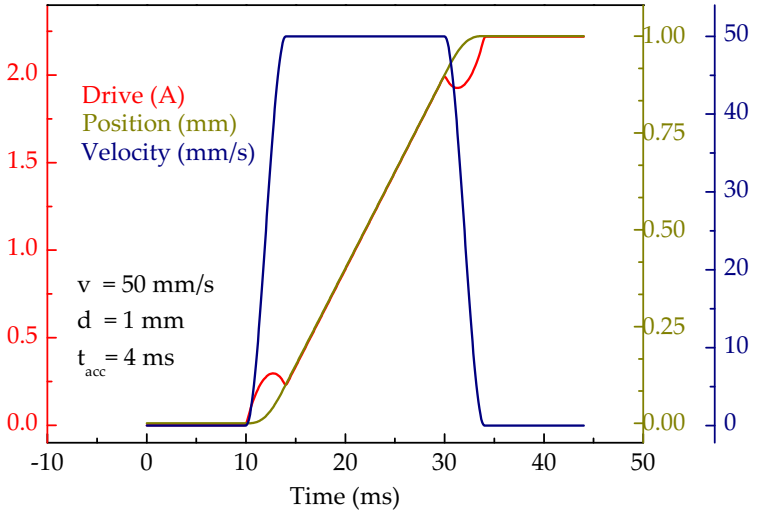

FIGURE 5.5: Calculated driving voltage to move the Floppy Wire by 1 mm at constant velocity of 50 mm s^{-1}. The expected time dependence of position and velocity are also shown.

5.3 Thermal response to Floppy Wire motion

Unfortunately, past efforts to measure the damping force exerted on the Floppy Wire directly with the pick-up coils from the lag of its position behind the driving force proved to be unsuccessful [75]. Since this lag is very small, the signal to noise ratio did not allow the position to be resolved with enough resolution to be of any use.

Therefore, a different method of determining the damping force indirectly has been developed. We can infer the dissipation from the increase in quasiparticle density measured by two nearby thermometers. As shown in Figure 5.1, there is a quartz tuning fork (called TF_2) placed just under the Floppy Wire as well as a NbTi vibrating wire (called $\mu\mu\mu_1$ and with wire diameter 4.5 µm). The $\mu\mu\mu_1$ wire is used as the main thermometer due to the better quality of the signal. The analysis of the response of the TF_2 signal produces a similar result, albeit with a lower signal-to-noise ratio. Dissipation due to movement of the Floppy Wire generates quasiparticles which results in an increase of the resonant width of both thermometers. Figure 5.6 shows a typical width change due to Floppy Wire movement for the $\mu\mu\mu_1$ probe. In fact, in all the following figures where the change of resonant width is shown, $\mu\mu\mu_1$ signal was used.

We measure the resonant width at high sample rate as described in Section 4.7.3, and use the width change as a measure of total dissipation. The signal before the pulse is averaged to determine the width before the pulse and subtracted from the maximum width during or after the pulse. A parabolic fit around the maximum is performed in order to reduce the noise of the signal.

Unfortunately, we can not consider this to be a direct bolometer measurement as only a fraction of the total dissipated power is captured by the thermometers. We believe that most of the quasiparticles created by the Floppy Wire motion get absorbed by the silver sinter above the wire or travel into the bottom of the experimental tailpiece. Nevertheless, even though this makes it impossible to determine the quantity of dissipated

heat precisely, it is reasonable to assume that the dissipation seen by the thermometers depends linearly on the unknown total dissipation. An attempt to calibrate the setup in order to estimate the dissipated energy is mentioned in Section 5.5.1.

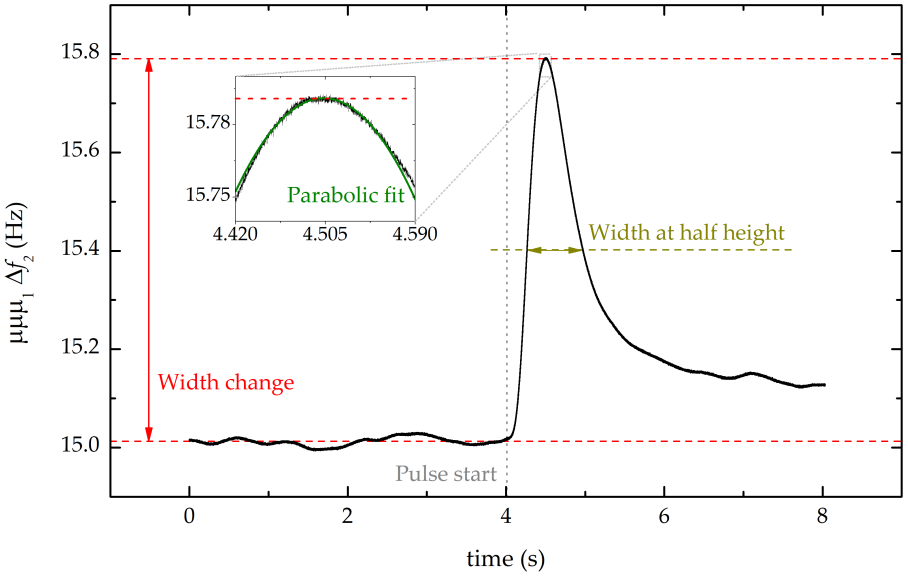

FIGURE 5.6: Resonant width response of the $\mu\mu\mu_1$ vibrating wire to a brief motion of the Floppy Wire. The motion of the wire generates quasiparticles which result in a resonant width change of the vibrating wire thermometer.

5.4 Previous results

The experiments described in this chapter are built upon the work previously undertaken on the same setup which led to a surprising result - a stable superfluid flow above the Landau critical velocity. This section serves as a brief introduction to the phenomena, more details can be found in a recently published report by Bradley et. al. [7].

When an amplitude sweep is performed with the Floppy Wire, it shows a characteristic dependence of damping force on velocity similar to other oscillators as described in Section 4.7.2. The initial low-velocity linear regime changes to non-linear due to thermal Andreev scattering (the transition velocity to non-linear regime strongly depends on temperature). A sudden

onset of large dissipation follows when velocity reaches the critical velocity $v_c \simeq 9\,\mathrm{mm\,s^{-1}}$. We call this a pair-breaking process because above this velocity the wire is able to create excitations - broken Cooper pairs.

However, to great surprise, the situation is noticeably different for the case of steady DC motion as shown in Figure 5.7. There is no onset of strong dissipation observed at $9\,\mathrm{mm\,s^{-1}}$. Even more interestingly, no strong damping is observed even as the Landau critical velocity $v_L = 27\,\mathrm{mm\,s^{-1}}$ is reached and exceeded. This is a truly fascinating discovery and to our knowledge nothing similar has been observed in any other condensate.

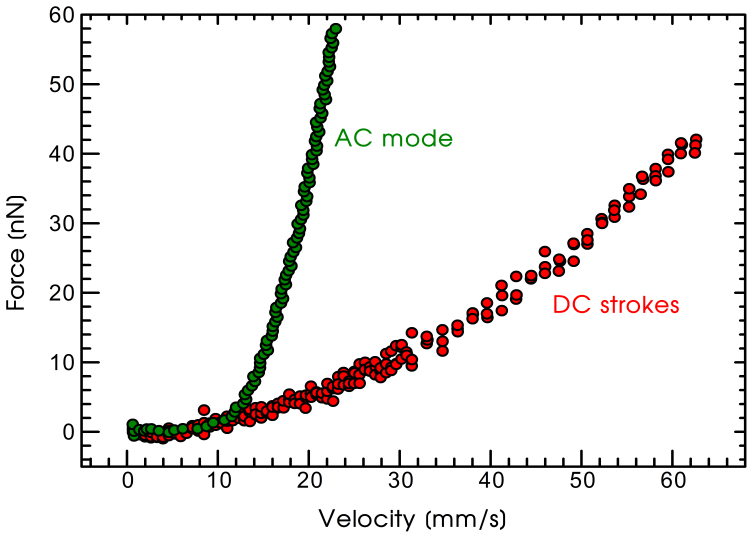

FIGURE 5.7: A striking difference in dissipation between oscillatory motion and motion at constant velocity. Figure modified from [75].

5.4.1 Model of pair-breaking dissipation

Bradley et al. [7] suggest a model that explains the dissipation without ruling out the Landau critical velocity - only making it inapplicable for linear motion. As mentioned in Section 4.7.2, when the superfluid flow reaches v_L, quasiparticles can be created at no energy cost which leads to breakdown of the superfluid. Therefore, there must be a mechanism preventing the new quasiparticles created at the surface of the Floppy Wire from escaping to the bulk when the wire exhibits constant linear motion.

In Figures 5.8 to 5.12 we draw the dispersion curves for the bulk superfluid far from the Floppy Wire as well as for the superfluid at the wire's surface. We use the moving frame of reference in which the Floppy Wire is stationary and the fluid far from the wire is moving at velocity v. As shown in Section 4.5, the maximum velocity in the surface layer is $2v$ and we choose to focus our discussion on this point as it will dominate the dissipation process. We also choose $T = 0$ for simplicity of discussion. The described mechanism of dissipation at elevated temperatures remains unchanged, but the process becomes more complicated as other means of dissipation become available. Figure 5.8 shows the dispersion curves when the Floppy Wire is stationary, a familiar bulk dispersion curve (identical to the one in Figure 2.3) and a surface state dispersion curve. The surface states are known as Andreev bound states [8] (or surface bound states) and are gapless. The suppressed energy gap of these states can be seen on the signature of specific heat [76] as well as thermal conductivity [40]. The effective shielding of bulk superfluid from the wire by these surface states is the key to the explanation of the dissipation during linear motion.

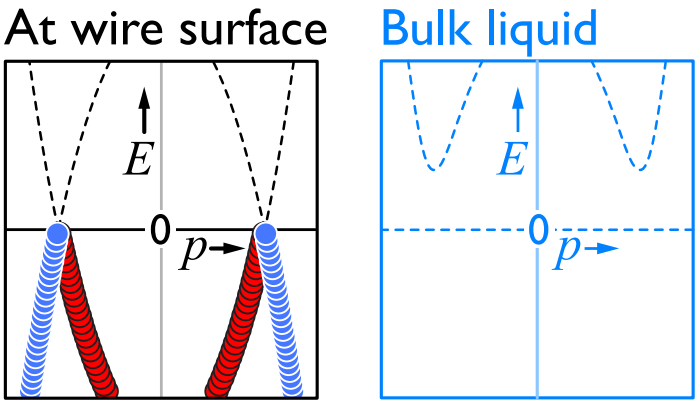

FIGURE 5.8: Dispersion curves of the superfluid excitations in the bulk as well as on the Floppy Wire's surface (quasiparticles shown in red, quasiholes in blue). The wire is at rest. At $T = 0$, the energy gap of the surface states reduces to 0.

As mentioned earlier, with increasing velocity the dispersion curve tilts as all the states gain momentum, see Figure 5.9. Note that the dispersion curve of the surface states tilts more as the relative velocity is greater there than in the bulk. Since the surface excitations are believed to be mobile

and can scatter along the wire's surface, they can exchange momentum with the wire. Some states from the $-p$ branch can exchange momentum and move to the positive branch of the dispersion curve - we call this a *cross branch process*. The moving excitation populates the $+p$ side of the dispersion curve, leaving an empty state at the $-p$ side.

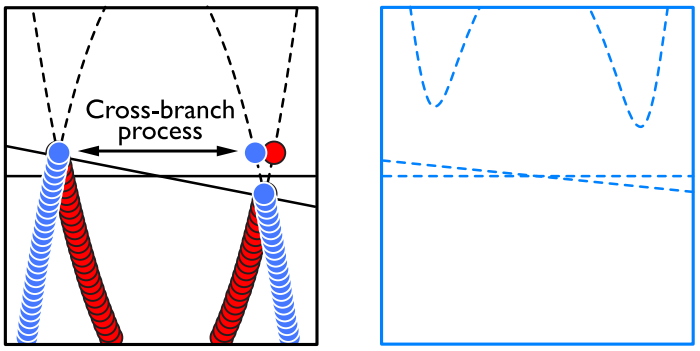

FIGURE 5.9: The dispersion curves start to tilt as the wire moves. The surface states can exchange momentum with the wire and jump from the $-p$ branch to $+p$ branch of the dispersion curve. We call this the *cross-branch process*.

At constant velocity the states eventually come to equilibrium as shown in Figure 5.10. The excited states that got to the $+p$ side with the cross-branch process can thermalise with the Floppy Wire and lose some of their energy. However, if $v > v_L/3$ the state that has just undergone a cross-branch process has enough energy to escape into the bulk as demonstrated in Figure 5.11. This possibility arises first when the minimum of the $+p$ side of the bulk dispersion curve becomes level in the energy with the maximum energy of the surface states excitations: $v = v_L/3$. This *escape process* into the bulk requires no extra energy and is responsible for the dissipation since the quasiparticle escapes from the wire and carries energy and momentum away.

The model predicts that the dissipation only happens when the velocity of an object is changing and the amount of created heat depends on the relation of the acceleration/deceleration time scale to the time scale of the cross-branch and escape processes. At constant velocity, the number of excitations allowed to undergo the escape process will become depleted. This

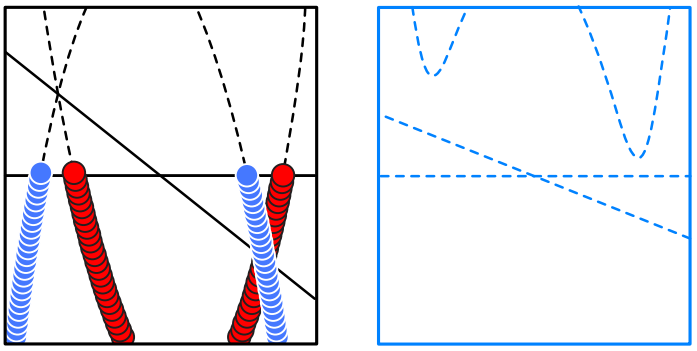

FIGURE 5.10: If the wire moves at constant velocity or changes its velocity too slowly, the surface excitations come to equilibrium through the cross branch processes.

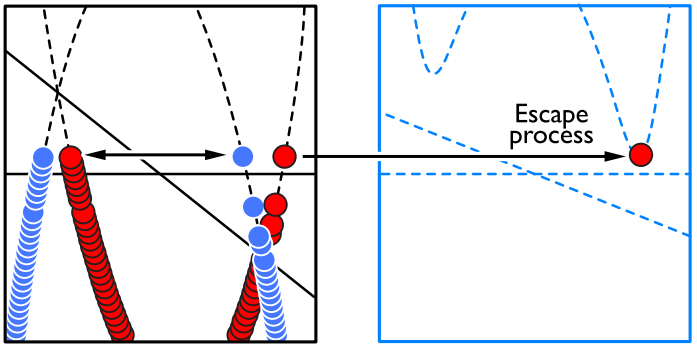

FIGURE 5.11: When $v > v_L/3$, the excited surface states from the $+p$ branch can escape to the bulk at no energy cost. This *escape process* represents the dissipation.

has never been observed in AC motion, because the wire is being accelerated at all times.

The time constant of the cross-branch process must be of the right magnitude to allow these processes to take place. If the cross-branch process was happening too fast, the $-p$ and $+p$ branches would quickly come to equilibrium, forbidding the escape process as shown in Figure 5.10. On the other hand, cross-branch jumps that were too slow would result in only a very few excitations available for escaping to the bulk from the $+p$ branch and thus contributing to dissipation. The following experiments in this chapter were developed to estimate the time scale of this momentum exchange process.

Before moving on, let us finally examine the movement of the wire from a stationary state to a velocity greater than the Landau critical velocity. As

the wire starts accelerating, some excitations can escape to the bulk when $v > v_L/3$ (Figure 5.12 a). As the velocity exceeds $v_L/3$, more and more states are allowed to undergo the escape process, increasing the escape probability and thus the dissipation during the acceleration (Figure 5.12 b). As the wire is accelerated past the full Landau velocity v_L, a new escape process becomes available. Some surface excitations in the $-p$ side of the dispersion curve can now escape to the $-p$ bulk branch directly (Figure 5.12 c). Nevertheless, this only causes a steady slow rise of dissipation as the escape probability grows. Once a steady velocity is reached, no matter how high, the excitations capable of escaping into the bulk will eventually deplete themselves and the dissipation process will stop. During deceleration this process inverts, giving rise to a burst of heat as the wire is brought to rest.

5.5 Frequency dependence of dissipation

The first obvious phenomenon to investigate after looking at Figure 5.7 is the frequency dependence of the AC amplitude sweeps. At some low frequency, one would expect that the dissipation signature of the oscillatory motion must begin to resemble the DC case.

Using the standard method of amplitude sweep for off-resonance frequencies with the Floppy Wire is not feasible due to significant overheating of the cell. The amount of heat dissipated by the Floppy Wire is larger than what the cold silver sinter can absorb and it is thus impossible to reach a steady state. Without fulfilling the equilibrium condition it is not feasible to compare the amount of heating at various frequencies. Coming back to the amplitude sweep shown in Figure 5.7, at the highest velocities the conditions for the AC mode are also non-equilibrium and the plot only demonstrates that the heating is much greater in the AC mode. However, one should not draw conclusions from the exact slope of the AC curve at highest velocities as it is not an equilibrium measurement.

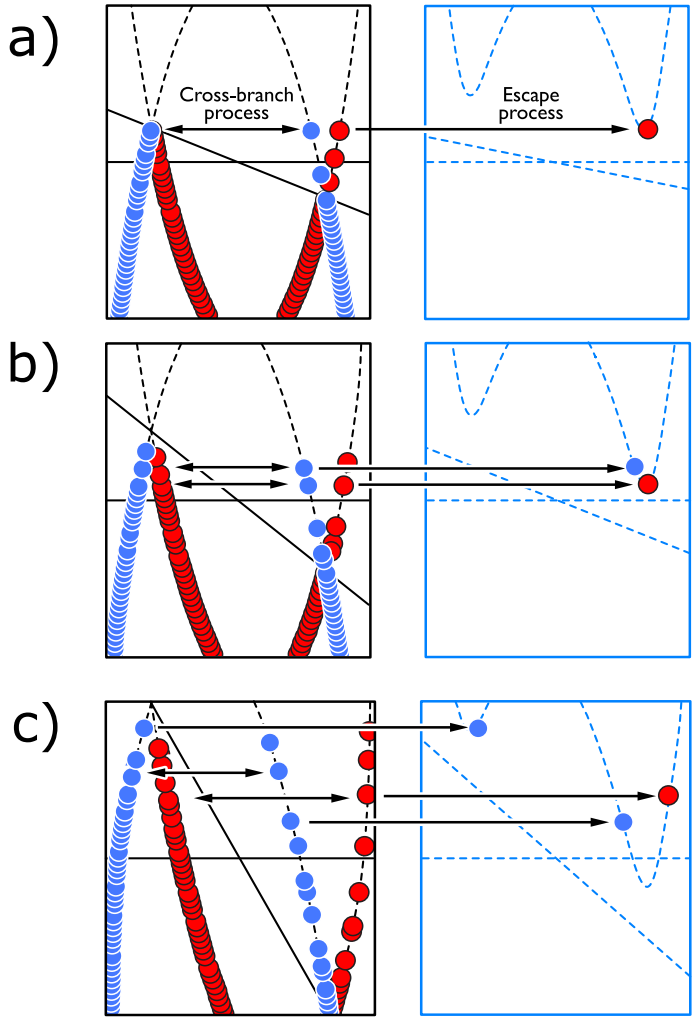

FIGURE 5.12: Mechanism of dissipation for linear motion when the velocity exceeds v_L. (a) When $v > v_L/3$, the first surface excitations can undergo the escape process. (b) As the wire accelerates further, more and more states can undergo the escape process and contribute to dissipation. (c) As wire accelerates past v_L, a new escape process into the $-p$ side of the bulk dispersion curve becomes available. Nevertheless, there is no sudden onset of large dissipation, only a slow steady rise due to increased escape probability.

For this reason we used another approach of driving the wire only for a short period of time. We created a series of bursts by driving the Floppy Wire at a specific frequency for a limited time duration and measured the thermal response with the thermometry in the vicinity of the wire. An example of such burst is shown in Figure 5.13. A typical burst duration that we used was 10 s, in order to give a large enough thermal signal without overheating the experimental volume. We were unable to run bursts at the

resonant frequency without significant ringing due to the high quality factor of the resonance. However, it is possible to perform bursts a few Hz away from the resonance without any sign of ringing on the emf signal.

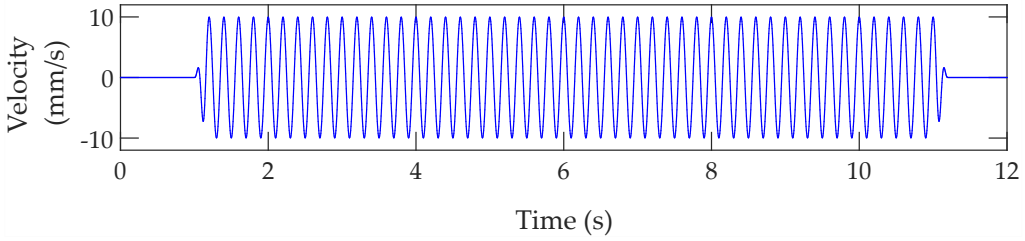

FIGURE 5.13: An example of a burst driving signal. The Floppy Wire undergoes periodic motion for a duration of 10 s, here with 10 mm s^{-1} maximum velocity and frequency of 5 Hz.

The measured frequency dependence of the dissipation below and above the resonant frequency in the range 20–90 Hz is shown in Figure 5.14. We observed no significant change in the dissipation for frequencies less than 30 Hz from the resonant frequency $f_0 \simeq 67$ Hz. Unfortunately, we came to believe that this heating was not caused by the motion of the wire per se, but by the movement of trapped magnetic flux lines inside the superconducting core of the Floppy Wire. Heat dissipation during unpinning of the trapped magnetic flux inside the type II superconductor such as our NbTi wire is a well known phenomena [77]. During magnetisation, magnetic flux lines penetrate the superconductor and are held there by a binding energy. The energy is released with the change of external magnetic field, dissipating into the superfluid. Similarly, as in our case, when the superconductor is moved in magnetic field the dissipation occurs [78].

The effect of flux jumps must depend on the current through the Floppy Wire. Further away from the resonance, more drive current is necessary to obtain the oscillatory motion of the burst, which results in more extra dissipation. Figure 5.15 shows linear dependence of measured heating on the drive current supplied to the Floppy Wire. More drive current results in more frequent flux jumps and extra dissipation. Moreover, the fact that the dissipation is magnetic field dependent is difficult to explain by any other mechanism than movement of magnetic flux lines.

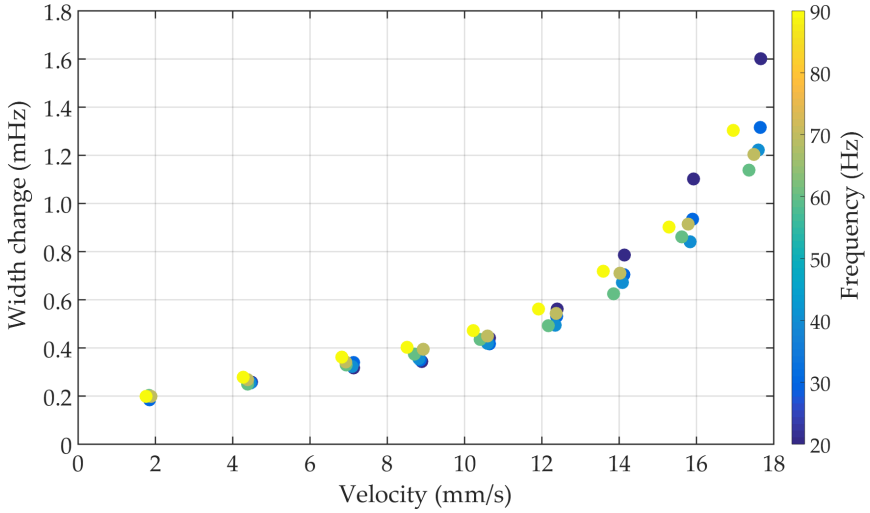

FIGURE 5.14: Frequency dependence of dissipation during bursts with the Floppy Wire. We observe no significant change of dissipation in frequency range 20–90 Hz - well above and below the resonance at $\sim$ 67 Hz. The first slight increase occurs for frequencies about 30 Hz away from the resonance. We believe this because of unpinning of the magnetic flux lines as the drive current increases with distance from the resonance frequency. The width change is measured with the $\mu\mu\mu_1$ vibrating wire. The same thermometer wire is used in all the measurement in this chapter.

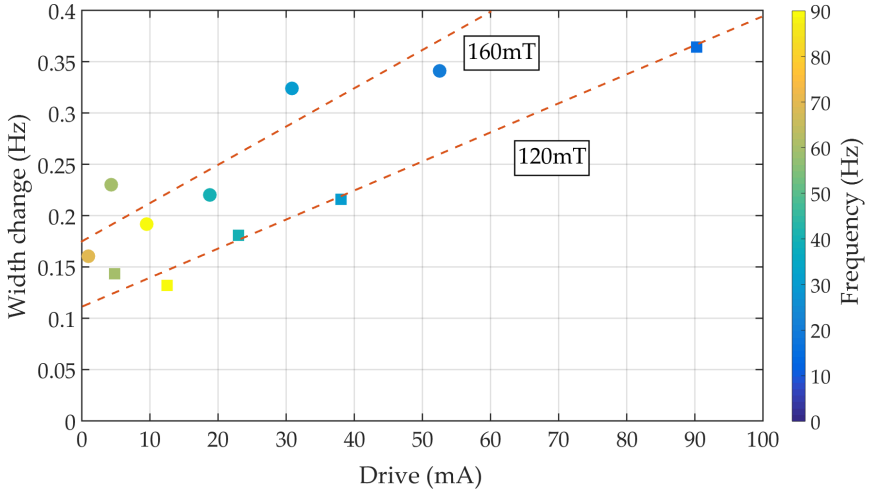

FIGURE 5.15: The linear dependence of drive current on the amount of dissipation suggests an effect of heating due to magnetic flux jumps inside the superconducting Floppy Wire. Higher drive current supplied to the wire results in stronger flux jumps and extra dissipation. The magnetic field dependence of the dissipation is another argument in favour of this effect.

5.5.1 Estimation of dissipated energy

In order to get a quantitative insight on the dissipation during bursts, we attempted to estimate the amount of dissipated energy through the process. Unfortunately, we cannot treat the experimental volume as a bolometer. This is mainly due to the near proximity of the cold silver sinter to the Floppy Wire - not all quasiparticles leaving the Floppy Wire during bursts contribute to the change of the resonant width of the VWR thermometer.

However, we can relate the heat 'seen' by the thermometers to the heat known to be dissipated during an amplitude sweep of the Floppy Wire. At resonance, the amount of dissipated energy is a product of the force exerted on the wire F, the velocity of the wire v and the duration of the movement δt

$$E = Fv\delta t \ . \tag{5.7}$$

Inserting the time of the burst duration as δt, we can match the dissipated energy during the amplitude sweep with that of the burst at a frequency close to resonance. As mentioned earlier, performing bursts at resonance is not feasible so we performed a series of 60 Hz bursts with varying velocity. We assume the dissipation during a burst at 60 Hz will be comparable to that of the burst at resonance.

Knowing the velocity during bursts from the emf, we matched the change in width of the 60 Hz bursts with the energy dissipated by the Floppy Wire during amplitude sweep for the same velocity. We are aware that this calibration is far from exact due to the frequency difference between the bursts and the amplitude sweep. Nevertheless, it should give us a ballpark estimation. As will be shown in Figure 5.16, we estimate the dissipated energy to be about 5 nJ for a 10 s burst at 10 mm s^{-1}.

5.5.2 Wall signal subtraction

To check that the heating was truly caused by the motion of the wire, we ran two series of pulses: a set of regular bursts in the superfluid near the middle

of the cell and another identical set when the Floppy Wire was touching the cell wall. As can be seen in Figure 5.4, the emf shows that the wire does not move when touching the cell wall. The second series therefore serves as a background measurement of any heating not caused by movement of the Floppy Wire and can be subtracted from the heating measured near the middle of the cell.

5.5.3 Results for low frequencies

Finally, we present the velocity dependence of dissipated energy for low frequencies. We used the energy calibration mentioned earlier and also subtracted the background signal of the burst when the Floppy Wire was touching the cell wall. Figure 5.16 shows the resulting dissipated energy for low frequency pulses. We focused on frequencies below 20 Hz as we have seen no significant change in dissipation in the higher frequency range, as shown in Figure 5.14. As expected, we observe slow deviation from 60 Hz pulses as the frequency lowers due to increasing drive current. Moreover, as the frequency lowers the distance the Floppy Wire travels at given velocity increases. This also contributes to the heating caused by flux jumps. We conclude that there is no decrease in the dissipated energy down to about 20 Hz, below which our measurements are inconclusive due to magnetic flux jumps.

5.6 Study of dissipation during acceleration

5.6.1 Pulse types

More insight into the dissipation mechanism can be gained by modifying the simple constant velocity ramp pulse. The dissipation model states that all excitations are released during the acceleration/deceleration phases and the amount of heating depends on the magnitude of acceleration. We thus ran a series of pulses shown in Figure 5.17. The wire was quickly accelerated

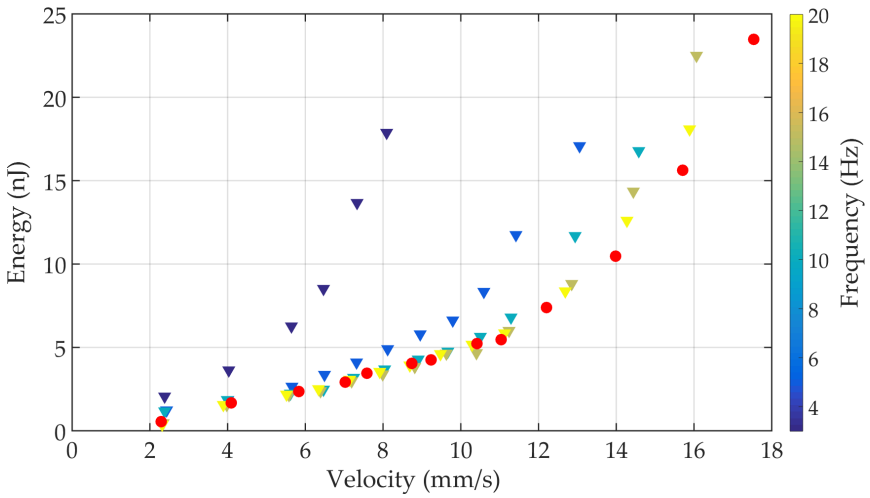

FIGURE 5.16: The dissipated energy as seen by the $\mu\mu\mu_1$ wire for low frequency bursts below 20 Hz. The increase heating with lowering of frequency is caused by movement of the magnetic flux lines inside the superconducting core of the Floppy Wire.

for a time t_{acc} to a steady velocity v and decelerated again to rest when a distance $d/2$ had been covered. After waiting a time t_{wait} the wire was then driven further through the cell volume (*up-up pulse*), or returned to the initial position (*up-down pulse*). The second stages used the same velocity profile, resulting in the same total covered distance d in both cases.

Another type of pulse shown in Figure 5.17 is the so called *half pulse*. The wire is not accelerated again after being stopped, undergoing only half of the total distance d. The acceleration profile is identical to that of the standard pulses with half as many accelerations. Therefore, if the bolometer method and the energy calibration are valid in our setup, we should observe half the width change on the probe wire $\mu\mu\mu_1$ and on the tuning fork TF_2.

5.6.2 Discovery and explanation

Figure 5.18 shows the waiting time dependence of the heating for the up-up and up-down pulses. We observe a notable difference in heating for the short waiting times and no difference for waiting times longer than about 30 ms. The difference in heating at short waiting times is our latest discovery and it allows us to gain new insights into the time constants involved in the dissipation process.

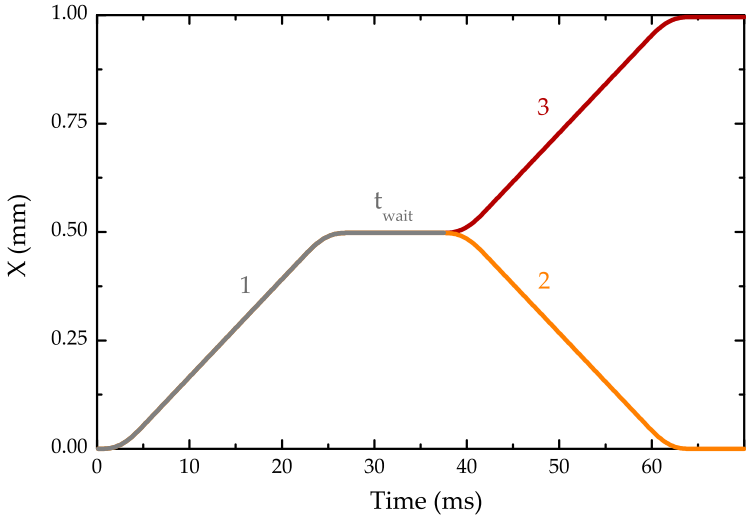

FIGURE 5.17: Three position profiles used in the experiment. The Floppy Wire is accelerated to a steady velocity and brought to rest after a distance $d/2$ is covered. After a certain waiting time t_{wait} the wire is either moved to the original position (1+2: *up-down pulse*), or moved once further with the same velocity profile (1+3: *up-up pulse*). During a *half pulse* the wire is not accelerated again after t_{wait} (profile 1 only).

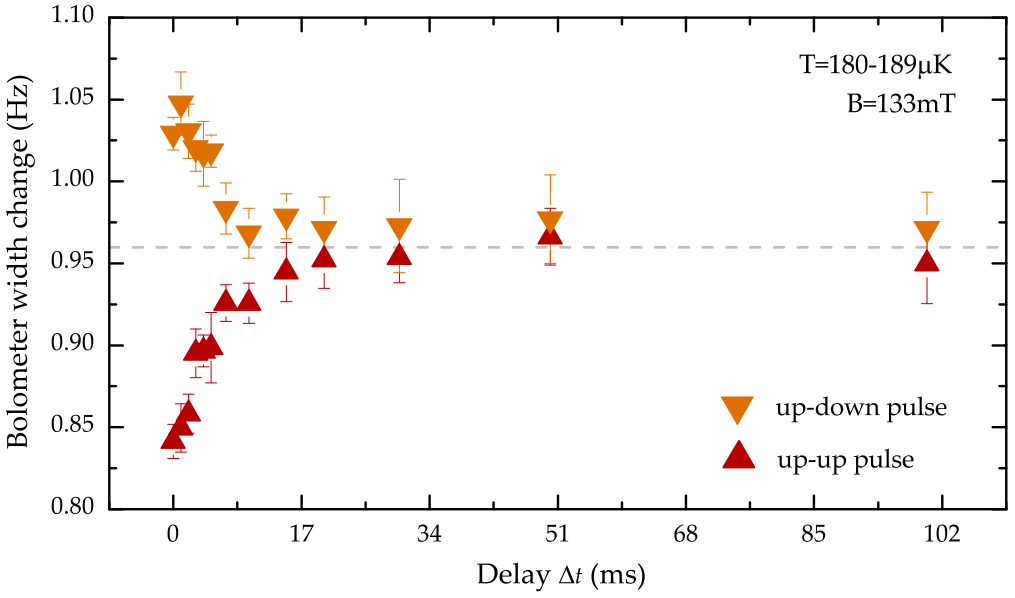

FIGURE 5.18: Waiting time dependence of the relative dissipation for the up-up ($\triangle$) and up-down ($\triangledown$) pulses. See the text for the explanation of the observed difference between the two types of pulses at short waiting times.

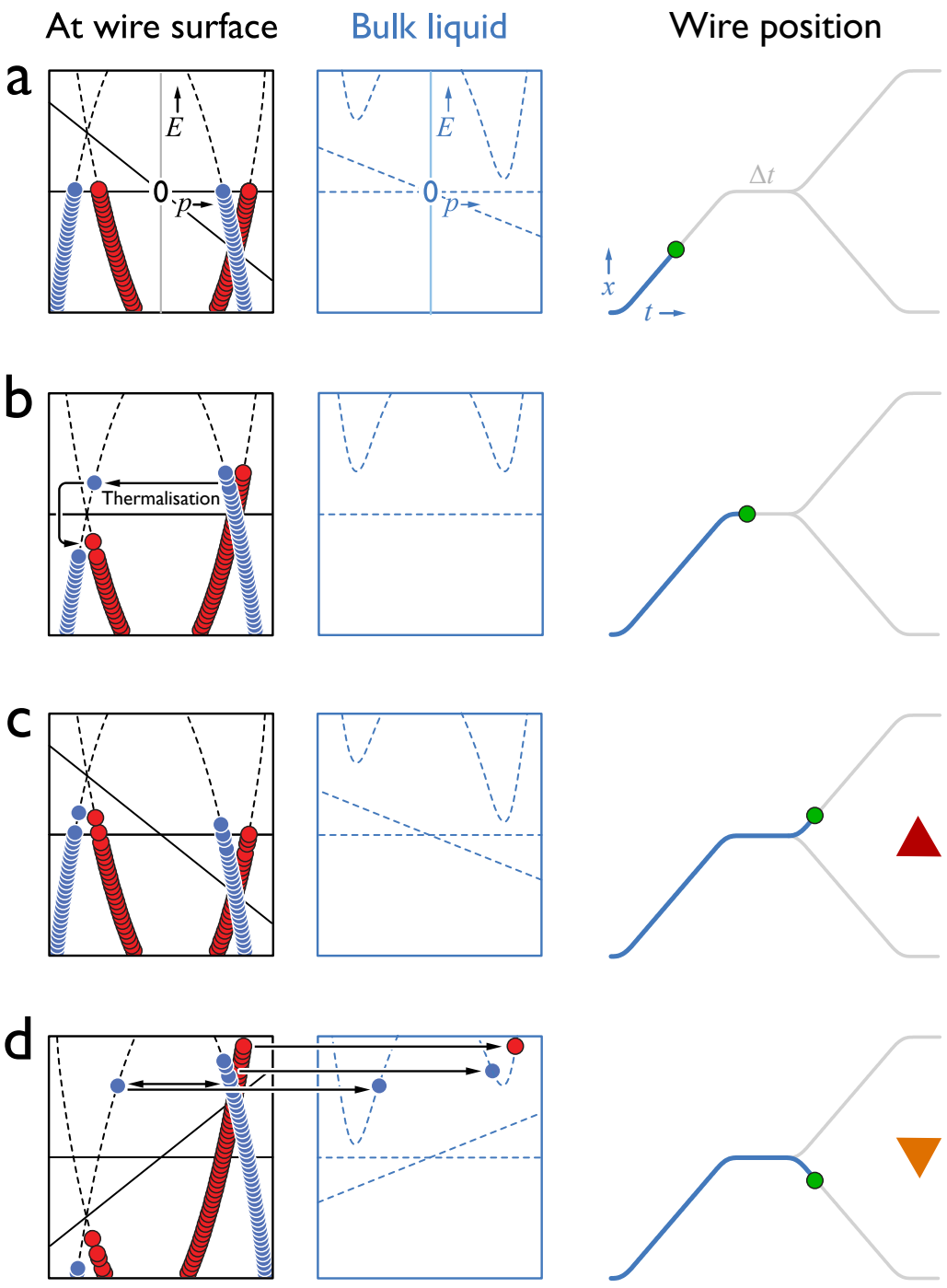

FIGURE 5.19: Mechanism of dissipation for the Floppy Wire under acceleration. (a) The wire is moving at constant velocity, the distribution of surface states is equalised and there is no more dissipation. (b) The wire is suddenly brought to a standstill. After the initial dissipation due to deceleration, the surface states attempt to re-equalize population in $-p$ and $+p$ branches. We call this a *thermalisation process*. (c) The wire is accelerated again in the same direction as before. The states that did not have time to thermalise during standstill do not contribute to dissipation. (d) The wire is accelerated in the opposite direction. More dissipation is observed, because more states are promoted to higher energy and can escape to the bulk.

In order to explain the measurements we return to the dissipation model described earlier and demonstrate it with the diagram shown in Figure 5.19. When the wire moving at a steady velocity (Figure 5.19a) is decelerated to a standstill and immediately accelerated again, the total dissipation will be less than if the wire was kept still for a longer period of time. When the wire is kept still for a very short time period, the surface excitations do not have enough time to undergo cross-branch processes and reach equal population in both $-p$ and $+p$ branches characteristic of the zero velocity dispersion curve, see Figure 5.19b. When the wire is quickly accelerated back to its original velocity, the excitations that have not undergone this thermalisation process can not contribute to dissipation as shown in Figure 5.19c.

A similar argument can be used for the dissipation when the movement of the Floppy Wire is quickly reversed. When the direction of velocity is changed suddenly, the surface excitations that did not thermalise to zero velocity equal population are elevated to higher energy and gain the means to escape to the bulk, see Figure 5.19d. Naturally, both cases should result in the same amount of dissipation when the waiting time t_{wait} is sufficiently long to allow all surface states to thermalise at zero velocity. Basically, at long waiting times the dissipation consists of four equal and independent contributions from two accelerations and two decelerations.

5.6.3 Experimental details

Due to the ever-present heat leak, the cell temperature is usually slowly rising during the measurements. Thermal damping grows with increasing temperature, creating an unwanted width change due to reasons other than the acceleration profile. We can compensate for this effect by running a half pulse prior to every type of pulse and subtract double the width change due to the half pulse. The result is a change in the width that is insensitive to the thermal damping.

The slight decrease of the height of the dissipation peak at very long t_{wait} can be contributed to having a pulse duration too long compared to the time

constant of the bolometer. The effect is clearly apparent in Figure 5.20 where two up-up signals for $t_{\text{wait}} = 30\,\text{ms}$ and $100\,\text{ms}$ are shown. At $100\,\text{ms}$ part of the heat gets absorbed by the sinter before the pulse is finished. The height of the peak is thus lower than expected while the width of the pulse slightly increases. One could argue that the integral of the signal would be a more appropriate measure, however it is difficult to estimate the baseline for integration - the cell does not fully recover after the signal and the width increases slightly. The product of width at half height times the height of the signal can be used, but it only introduces more scatter.

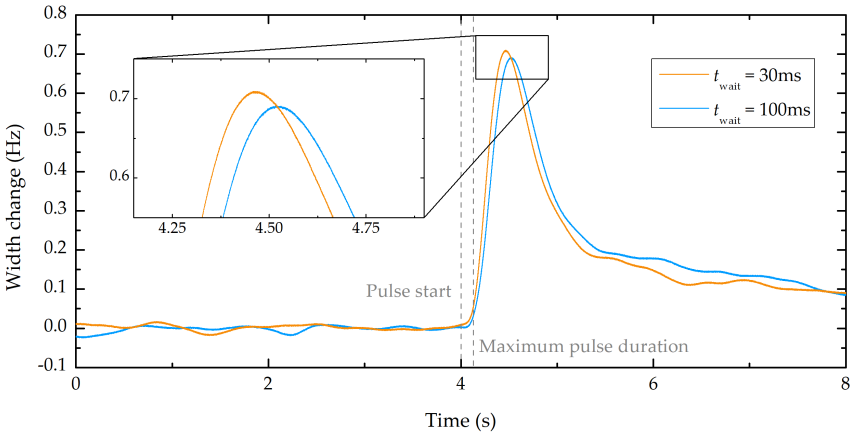

FIGURE 5.20: An example of long waiting time pulses of $t_{\text{wait}} = 30\,\text{ms}$ and $100\,\text{ms}$ pulses (average of 12 pulses each). The amount of dissipated heat during the pulse should be virtually identical for such a long t_{wait}. The reduction of observed heating for $t_{\text{wait}} = 100\,\text{ms}$ is attributed to the absorption of heat by the cold silver sinters during the pulse period.

Qualitatively, the measured data match well with the dissipation model, increasing our confidence in its validity. The result is robust and we do not believe it can be explained by flux jumping or other issues encountered earlier. We observed the same splitting for short t_{wait} in various magnetic fields, temperatures and positions inside the cell. Since the resonant frequency varies slightly with the position of the Floppy Wire (within 1 %), observing consistent difference in heating for short t_{wait} rules out the possibility of higher resonant modes influencing the result. We have also found the difference in heating when stopping at positions other than half way, though the interpretation of the results is slightly more complicated.

5.6.4 Variation of pulse parameters

We can modify various parameters of the pulse and observe the effect on the heating. When decreasing the maximum velocity, we observe a decreasing difference between the pulses at short t_{wait} as well as a smaller total amount of dissipation, see Figure 5.21. This can be explained simply by fewer surface states participating in the dissipation process as less of them are promoted to higher energy during acceleration.

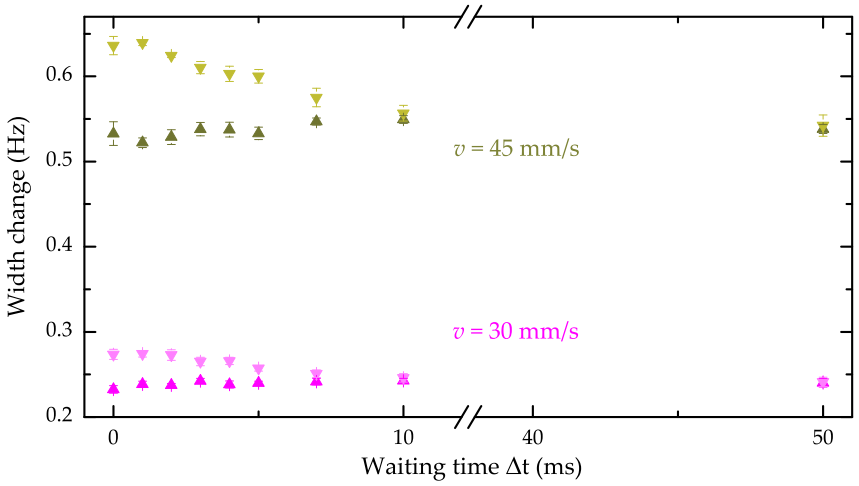

FIGURE 5.21: Increasing the velocity of the pulses changes the total amount of dissipation as well as increases the difference between heatings for short t_{wait}. However, the relaxation time remains the same as far as we can tell from the data.

When increasing the time of acceleration and deceleration, not only the total amount of dissipation decreases but also the difference between the two pulses vanishes earlier, see Figure 5.22. Slower acceleration gives the surface states more time to equilibrate before reaching energy sufficiently high to escape into the bulk.

Even though we can vary the pulse parameters, the available range is rather small. The first major limitation is the maximum travel distance of $\sim 1\,\text{mm}$, due to significant magnetic flux jumping at longer distances. Even though the total travelled distance is the same for up-up and up-down pulse, the maximum displacement of the Floppy Wire is twice as large for the up-up pulse, resulting in higher flux jump dissipation. The effect tends to be more pronounced at lower velocities where the total dissipation due to

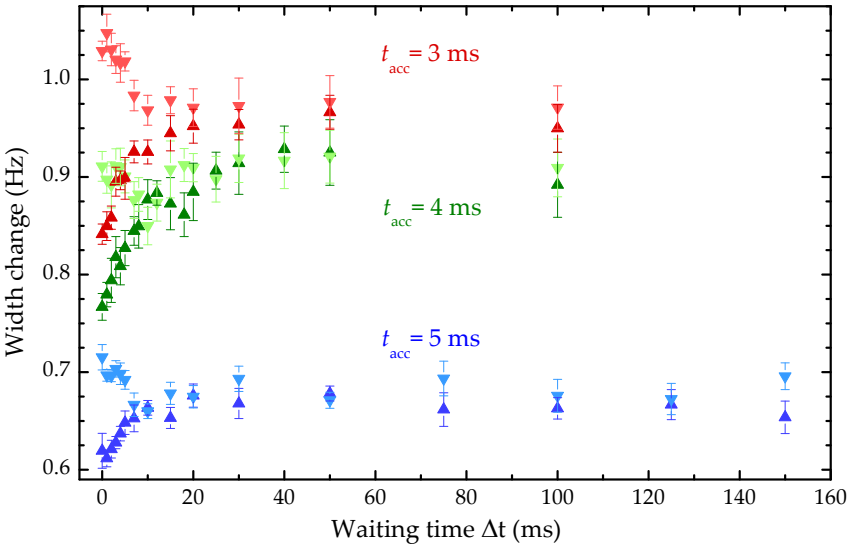

FIGURE 5.22: Shorter acceleration times t_{acc} result in increased amount of dissipation. Moreover, the time constant of dissipation increases with faster acceleration.

acceleration is lower. We are also limited by the maximum acceleration. At very small t_{acc}, the unwanted higher resonant modes of the Floppy Wire start to get excited. The excitation of the 445 Hz overtone is clearly visible on the Fourier transform of the Floppy Wire emf as shown in Figure 5.23.

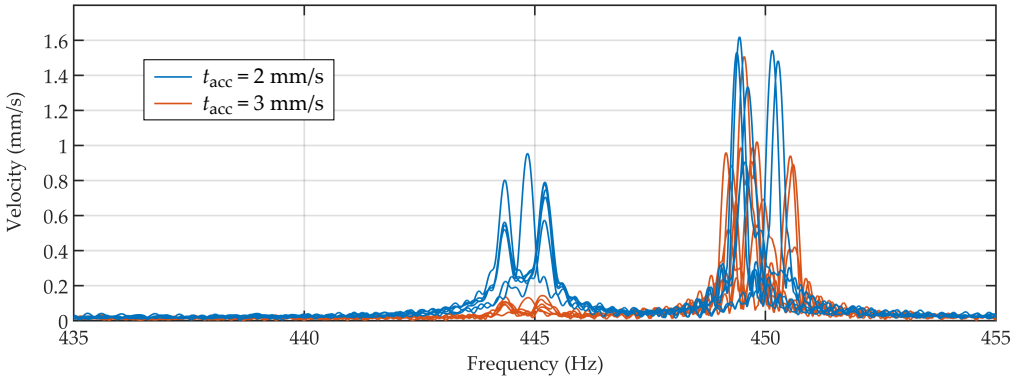

FIGURE 5.23: Fourier Transform of the emf of the Floppy Wire. The Floppy Wire has a higher mode of resonance with a frequency of about 445 Hz. The figure shows the emf footprint around this frequency for two sets of pulses differing only in the acceleration time t_{acc}. The emf clearly shows that the higher resonant mode is excited when the wire is accelerated too hard. The peaks at 450 Hz are due to 50 Hz mains interference.

5.6.5 Temperature dependence of dissipation

An obvious question to ask is what is the temperature dependence of dissipation. The answer can give us more insight into the dissipation process and into how the surface excitations that escape to the bulk refill again. We performed a series of identical sets of ramp signals similar to the one shown in Figure 5.18 at various temperatures in the range 140–240 µK. Each set is an overnight measurement with every pulse type averaged about 20 times to minimise the noise. The slow temperature increase during overnight measurement is always less than 12 µK. We can plot the difference in heating between the up-up and up-down pulses as shown in Figure 5.24. As before, we see a difference between the pulse types for short waiting times which eventually vanishes for longer t_{wait}. We fitted an exponential curve $Ae^{-x/\tau}$ to extract the time constant τ of this decay.

Figure 5.25 shows the temperature dependence of the extracted time constant from each set of pulses. Even though the scatter of the data is very large, we can conclude that the dependence on temperature, if there is any, is very weak. This result suggests that the surface states on the wire are not refilled from the superfluid after escaping to the bulk. In this temperature range the density of available thermal excitations in the bulk increases more than 20 times. If the bulk thermal excitations were responsible for refilling the surface states, we would expect a much stronger temperature dependence. We are thus led to speculate that the refilling happens perhaps via the legs of the Floppy Wire from the surrounding cell walls as such process should be temperature independent, see the conclusions of this chapter and Figure 5.28.

5.7 Higher modes of resonance

We have seen that the time constant for replenishing of the surface states on the Floppy Wire is about 4 ms. It is thus natural that we observe large dissipation when driving the wire above v_{L}, because the time of one cycle

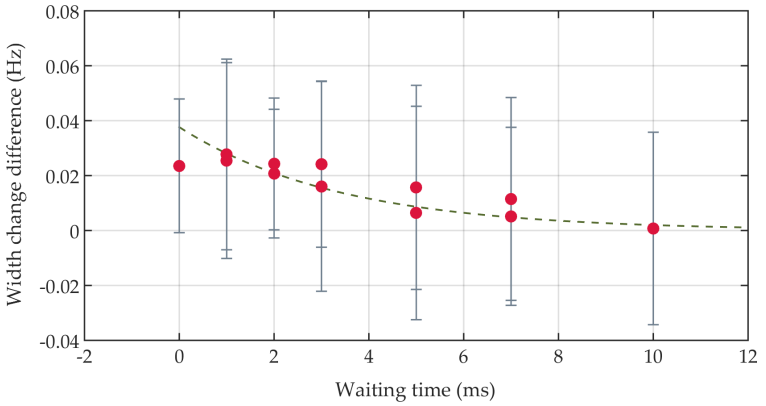

FIGURE 5.24: A difference in $\mu\mu\mu_1$ width change between the up-up and up-down signals for various waiting times. Each pulse is repeated 20 times for averaging and the error bar represents the standard deviation. The cell temperature was slowly increasing throughout this overnight measurement, ranging between 142–152 µK. An exponential curve $Ae^{-x/\tau}$ is fitted in order to extract the time constant τ of the decay.

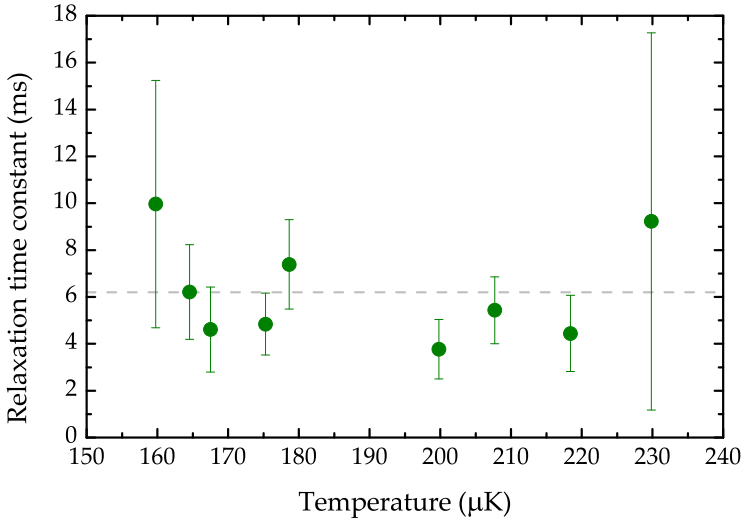

FIGURE 5.25: Temperature dependence of the surface states relaxation time constant τ. Each data point represents an exponential fit to a set of signals as show in Figure 5.24. The temperature of the data points is the average temperature during the each set. Every set is an overnight measurement with the temperature variation within 12 µK. The grey dashed line represents the mean value $\tau = 6.2$ ms.

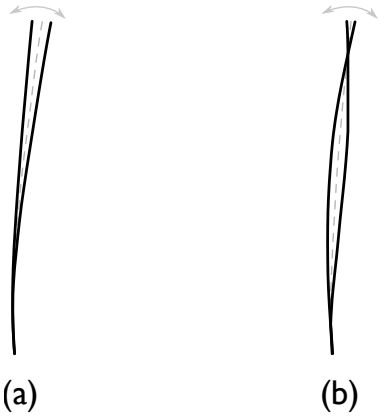

FIGURE 5.26: (a) Fundamental resonant mode and (b) the first overtone of the Floppy Wire. The lines are traced from the photographs of the dummy wire driven in air. The higher mode corresponds to the first overtone of the clamped beam with the additional mass of the crossbar at the free end.

at the fundamental mode of resonance at about 66 Hz is $\sim$ 15 ms. If we were able to drive the wire at higher frequency there should be a change in heating. At a certain point, when the time of one cycle is much shorter than 4 ms, we should observe a decrease in pair-breaking dissipation as there is not enough time to refill the surface states.

Fortunately, the normally undesirable higher modes of resonance can be used to probe this effect. It turned out that the first overtone with frequency at $f_1 \simeq 445$ Hz is suitable as the HWD parameter is almost as high as that for the fundamental mode. In order to determine the shape of this resonant mode, we built a dummy Floppy Wire identical to the one inside the experimental volume. We found a natural frequency of 66 Hz as well as the first overtone at 425 Hz. The excellent agreement in frequency ratio f_1/f_0 of the two devices gives us great confidence that we are observing the same overtone (6.75 and 6.44 respectively). The shape of both modes is shown in Figure 5.26, where the lines are traced from photographs of the dummy wire in motion. The mode corresponds to the first overtone of the clamped beam with additional mass at the free end (the mass of the crossbar). The theoretical ratio of f_1/f_0 for these two modes is 6.88 [79].

Naturally, for a given maximum velocity of the overtone the necessary force is not the same as that of the fundamental mode. In order to compare the dissipation, it is thus necessary to scale the force. We expect the same

velocity dependence of thermal Andreev dissipation before reaching v_c for both modes, so we can scale the higher velocity mode to match the low velocity dissipation.

Figure 5.27 shows the scaled amplitude sweeps for the fundamental mode as well the first overtone for two different temperatures. At 140 µK we observe a reasonable consistency in the value of v_L for both modes after the force scaling. The heating at higher frequency is lower than at the fundamental mode, consistent with the dissipation model. The different shapes of the curves for the two frequencies can be explained by parts of the wire contributing to dissipation differently in each mode as the velocity profile along the legs of the wire varies between the two modes, see Figure 5.26.

We were not however able to reproduce the promising results at higher temperature. The scaling factor of velocity surprisingly changed significantly from 13 to 2.5. We are not sure what causes such a large discrepancy, perhaps the intrinsic damping of the wire is no longer negligible as the thermal damping lowers greatly with temperature. We also observed an anomalous lack of damping just below the critical velocity, where a small increase in driving force results in a great increase in velocity. This effect has been previously observed with the Floppy Wire [80] and is believed to be due to the production of a turbulent tangle of vortices by the wire itself. This vortex tangle then screens the wire from the bulk thermal quasiparticles, lowering the dissipation.

Unfortunately, the self-screening effect and the possibility of non-negligible intrinsic damping complicate the picture significantly and we must consider the results rather inconclusive.

5.8 Conclusions

The experiments with the Floppy Wire resonator have brought new findings about dissipation above the Landau critical velocity v_L. The surprising lack

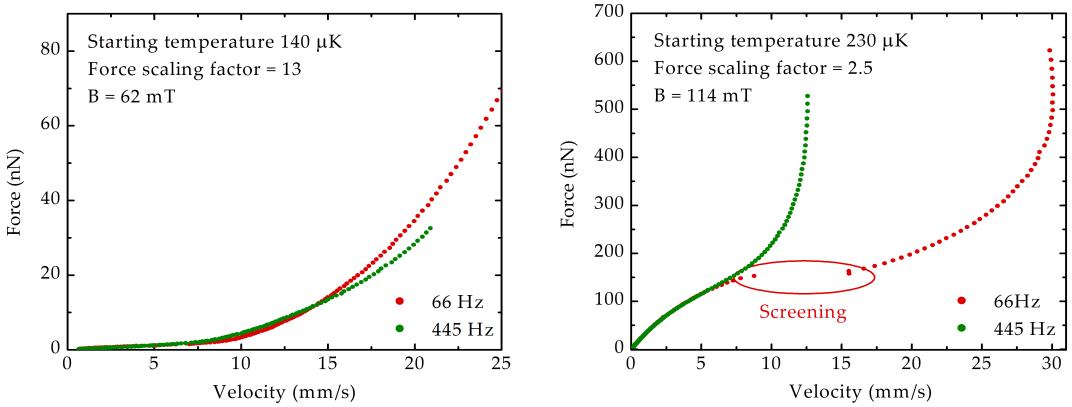

FIGURE 5.27: Comparison of the amplitude sweeps at the fundamental mode as well the first overtone with scaled force to match the thermal damping for $v < v_L$ at two different temperatures. (a) At 140 µK we observe similar values of v_L for both modes as well as decreased dissipation at higher frequency, consistent with the dissipation model. The scaling factor of the force is 13. (b) At 230 µK the situation is strikingly different. As expected, the thermal damping is much larger, but the force is scaled by only a factor of 2.5 to match the initial slope of dissipation. The critical velocity is hard to estimate as we observe a strong effect of possible turbulent screening of quasiparticles, see the text for detail.

of large heating above v_L during uniform linear motion can be explained by the proposed model of dissipation.

We attempted to measure the frequency dependence of heating during AC motion to find the frequency that marks the transition between the two distinct signatures of dissipation (oscillatory and linear motion). We observed significant heating at frequencies below about 20 Hz. We believe that this effect is not caused by the movement of the wire per se, but is caused by heating due to magnetic flux line jumps. The effect depends on both drive current and the magnetic field strength. We observe no frequency dependence in the 20–90 Hz, and below 20 Hz the results become inconclusive due to extra heating.

We studied the heating under acceleration to test the predictions of the dissipation model. We find the predictions of the model are valid for the cases tested. By these measurements we were also able to estimate the time constant of the thermalisation process - the time necessary for the states to come to new equilibrium after acceleration. We estimate the time constant

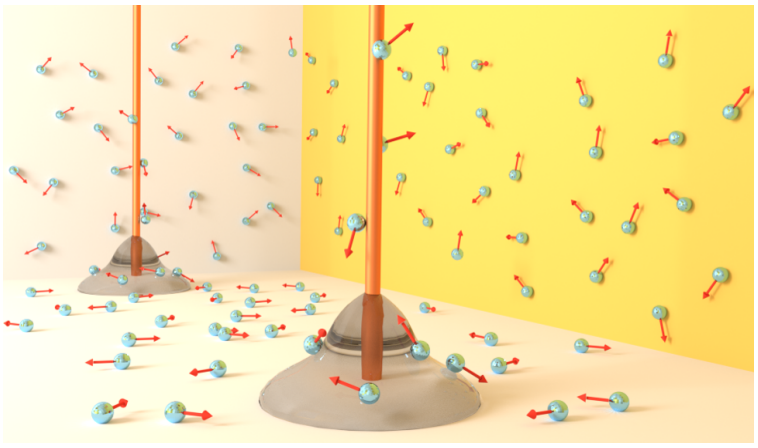

FIGURE 5.28: A representation of the surface states on the cell walls creeping up the legs of the Floppy Wire to refill the missing states after the wire acceleration.

to be approximately 6 ms.

Even though there is much scatter in the data, we observe that the time constant is only weakly, if at all, temperature dependent in the 160–230 µK range. Such a weak dependence suggests that the thermalisation process does not involve the bulk states whose density changes greatly in this temperature range (more than 20 times). We propose that the surface states might be refilled by the other surface states along the cell walls that 'creep' up along the legs of the wire as shown in Figure 5.28. One could test this theory by making a series of Floppy Wires with varying leg lengths and measuring the dissipation. However, a very similar resonant frequency of all such Floppy Wires would be required. From our experience with building the dummy Floppy Wire, we have seen that the resonant parameters do not change much as the wire is cooled down. Therefore, one could experiment with simple room temperature models to modify the resonant frequency (e. g. by adding weight to the crossbar).

There is a possibility to use the existing setup and attempt to modify the surface conditions by adding a small amount of ^{4}He into the sample ^{3}He. When ^{4}He is added into superfluid ^{3}He, it preferentially plates onto the available surfaces. It has been shown that such coatings can significantly alter the surface conditions, changing the scattering nature of the surface from diffuse to specular [81, 82]. The coverage of this layer can be well controlled

by adjusting the concentration of ^{4}He in the mixture. ^{4}He thus provides a unique chance to modify the surface conditions in situ and measure effect on the surface bound states.

Chapter 6

Aerogel Demagnetisation Experiment

This chapter describes the design of a new experimental cell exploiting demagnetisation of solid ^{3}He on aerogel. The cell design follows the standard 'Lancaster style' principles utilizing double nested cell and copper powder refrigerant, which are introduced in the beginning of this chapter. The description of the new experimental cell follows together with its cool down time calculations. The new superconducting solenoids are described as well as the NMR circuitry used. The following section addresses practical procedures for standard operation of the new cell. The last part of the chapter describes the unexpected heating problems encountered during the demagnetisation of copper and our attempts to resolve this issue. The chapter is finalized by proposing future steps necessary in order to continue with the experiment.

6.1 'Lancaster style' nuclear demagnetisation stage

In the traditional approach [50, 83], thin slabs or wires of usually Cu or $PrNi_5$ are demagnetised in a separate volume with high magnetic field away from the experimental cell. Thermal contact to the ^{3}He sample a distance away from the high field area is usually provided by high purity silver

wires with silver sintered heat exchangers. The main disadvantage of this approach is a larger heat leak into the experimental volume and the limited heat exchange area with the ^{3}He due to Kapitza resistance [9]. Even though the exact nature of this thermal resistance is rather complex, the resistance arises from the difference between the acoustic velocities in helium and practically all solids [84]. A way to address both of these problems is to use the 'Lancaster style' nested cell design with a copper powder refrigerant [10]. In this configuration, the experimental volume lies in the near vicinity or even inside the copper demagnetisation stage. As a disadvantage, such a setup does not permit using magnetic materials in the experimental volume due to the high magnetic field (typically $\sim 8\,\mathrm{T}$) necessary for copper demagnetisation.

The experimental tailpiece with the demagnetisation stage connects to the mixing chamber via a seal made of soap and glycerine solution [85]. The copper refrigerant is thermally connected to the mixing chamber via a set of annealed high purity silver wires with silver sinter to increase the surface area available for heat exchange. The thermal connection can be broken with a superconducting aluminium heat switch welded to the silver wires. Unlike the more common designs with a separate magnet to operate switching magnetic field [86], here the heat switch is operated with the fringing field of the main 8 T magnet.

The experimental cell consists of two nested volumes, each with its own copper refrigerant. The inner volume uses thin copper slabs to cool down ^{3}He, while the outer cell uses densely packed fine copper powder as a refrigerant (packing ratio of about 70 % of Cu to 30 % of ^{3}He). The main benefit of using the powder instead of using solid Cu slabs is much greater surface area, resulting in significantly better thermalisation of copper with ^{3}He. Moreover, copper in the form of powder has much stronger internal magnetic field of about 350 mT [87] compared to only 0.4 mT in the case of pure copper block [88]. This field prevents demagnetising to very low effective magnetic fields, so the outer cell ^{3}He temperature does not get below

about 1 mK. However, more importantly, the internal field also gives significant heat capacity to Cu - protecting the inner cell from parasitic heat flows for periods exceeding up to a week in some cases [10]. There is no powder refrigerant in the inner cell, so the demagnetisation is carried out down to an effective field given by the final external applied magnetic field, typically around 30 mT. The sample ^{3}He inside the inner cell thus undergoes its superfluid transition and reaches temperatures typically down to $\sim$ 130 µK, depending on the design of the individual experimental cell. The main advantage of the nested cell design is typically longer hold times at ultra-low temperatures due to minimisation of the heat leak. On the other hand, this design does not allow for quick modifications of the experimental volume, which usually requires the destruction of the outer cell at the very least.

Both inner and outer cell volumes are filled with ^{3}He and connected together with a long, high impedance capillary. The long path minimises the heat leak to the inner cell, but one must be careful to avoid large pressure gradients that could break the thin walls of the inner cell. Even though the outer cell is filled with sample ^{3}He, there is no direct thermal contact to inner cell due to very large boundary resistance between the cell walls and the fluid.

6.2 Aerogel demagnetisation cell

The design of the new experiment follows the ideas outlined in the previous section. The inner cell consists of copper plate refrigerant at the top and a long tube with aerogel at the bottom. The outer cell surrounds it, with copper powder densely packed at the top and held in place by a piece of filter paper.

A stycast-impregnated paper tube, 39 mm long and 8 mm in diameter, connects the experimental area with the inner cell copper refrigerant. A glass tube, 4.2 mm in diameter and 47 mm in length, is connected to the end of this stycast paper tube. The glass tube is made of Pyrex suitable for NMR

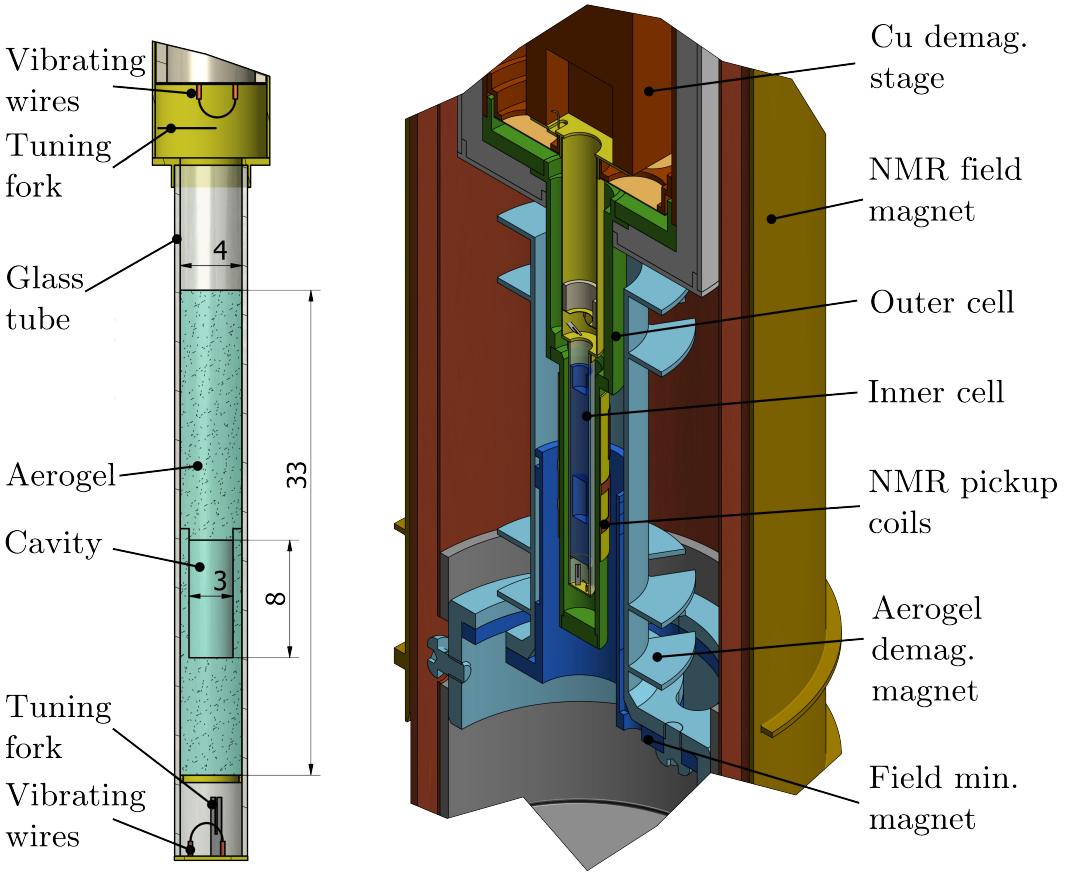

FIGURE 6.1: Isometric cut of the experimental setup with the detail of the inner cell. Given dimensions are in millimetres.

experiments and it contains the aerogel sample, see Figure 6.1. The sample is rather large: 33 mm in length and 4.2 mm in diameter and it contains a cylindrical cavity (8 mm long and 3 mm in diameter). Due to the cavity, the aerogel consists of two pieces fitting into each other, deliberately allowing no direct line of sight into the cavity. The aerogel sits on a small stycast paper ring that is glued to the inner walls of the glass tube. This glass tube is connected to the wider 8 mm stycast paper tube that leads to the copper demagnetisation stage.

Inside this wider tube just above the connection to the glass tube there is the top thermometry stage. This consists of a single 50 µm thick quartz tuning fork, named TF_{top}, with a resonant frequency of ~ 17 kHz and two vibrating wire resonators named $\mu\mu\mu_1$ and $\mu\mu\mu_2$. Both VWRs are loops of 4.5 µm diameter NbTi wire and with leg spacing of 2.45 mm and 2.29 mm

respectively. Near to the other end of the stycast paper tube, close to the sinters of the copper demagnetisation stage there is a tantalum VWR with 4 mm leg spacing and 125 µm wire diameter. This vibrating wire resonator, called ICTA (Inner Cell TAntalum), is used at higher temperatures during precool, when the regular vibrating wires are too heavily damped to be sensitive. A similar VWR to ICTA named OCTA (Outer Cell TAntalum) is situated in a free volume within the outer cell copper powder refrigerant to monitor the temperature of the ^{3}He in the outer cell.

The bottom of the glass tube is terminated with another thermometry stage. Here, there is also a 50 µm thick quartz tuning fork with resonant frequency of $\sim$ 33 kHz (named TF_{bot}) as well as two VWRs: one named $\mu\mu\mu_3$ with wire diameter of 4.5 µm and 3.32 mm leg spacing and a second, finer wire named Mμ that has a very fine 1.5 µm wire diameter and 1.20 mm leg spacing. The information about the probes inside the inner cell is summarized in Table 6.1.

The variety of the temperature sensors inside the cell is justified as follows. Mμ is the best vibrating wire thermometer in the low temperature ballistic regime due to its lowest mass and therefore highest temperature sensitivity in the less dense quasiparticle gas. However, the wire is very fragile and has a very delicate manufacturing process. ICTA and OCTA perform best at higher temperatures, especially during the precooling phase when very viscous ^{3}He creates very large damping. The wires $\mu\mu\mu$ and tuning forks are also very good temperature sensors as well as heaters in superfluid. The $\mu\mu\mu$ is slightly more sensitive at the lowest temperatures, but tuning forks can perform in the absence of an external magnetic field and are more sensitive at higher temperatures where the damping of superfluid ^{3}He is higher. The last method to determine the temperature is from the NMR signal. In bulk superfluid inside the aerogel cavity this can be done by studying the decay of the Bose-Einstein condensation of magnons as described in Section 2.5.

TABLE 6.1: Cell thermometry summary. The resonant parameters for the vibrating wires are not available as their operating temperature range has never been reached.

		Dimensions		Resonance parameters	
		Leg spacing	Wire diameter	$f_{0\text{vac}}(4\,\text{K})$	$\Delta f_{2\text{vac}}(4\,\text{K})$
Above aerogel	$\mu\mu\mu_1$	2.45 mm	4.5 µm	-	-
	$\mu\mu\mu_2$	2.29 mm	4.5 µm	-	-
	TF_{top}	-	-	16 967 Hz	0.07 Hz
Below aerogel	$\mu\mu\mu_3$	3.32 m	4.5 µmm	-	-
	Mμ	1.2 mm	1.5 µm	-	-
	TF_{bot}	-	-	33 601 Hz	0.11 Hz
Copper region	ICTA	4.0 mm	125 µm	3077.6 Hz	0.59 Hz
	OCTA	4.1 mm	125 µm	2927.7 Hz	0.38 Hz

6.3 Initial calculations

After the initial design was outlined, a feasibility study was carried out to check whether the cooldown time of the ^{3}He on the aerogel after the initial copper demagnetisation was within sensible limits and what final ^{3}He temperature might be expected. Since the aerogel sample is a long cylinder, one can not assume its temperature to be uniform. A numerical model of the cooldown was produced and the outline of the thermal model is shown in Figure 6.2.

The model was required in order to indicate if there were any limits in pre-cooling of the ^{3}He on aerogel, modelled as a series of interconnected heat capacities at various temperatures connected by thermal links. The initial conditions are that the aerogel is at a uniform temperature 800 µK with the copper at 100 µK. The question being addressed was how quickly would the solid ^{3}He on aerogel cool down. To simplify the following discussion, we will use the term 'aerogel' as shorthand for the more correct 'solid ^{3}He on aerogel'.

The aerogel sample is cooled by a copper block at temperature T_{Cu} with heat capacity C_{Cu}. The nuclear heat capacity of the copper block is related to the entropy of the system and depends on the magnetic field as $C \sim$

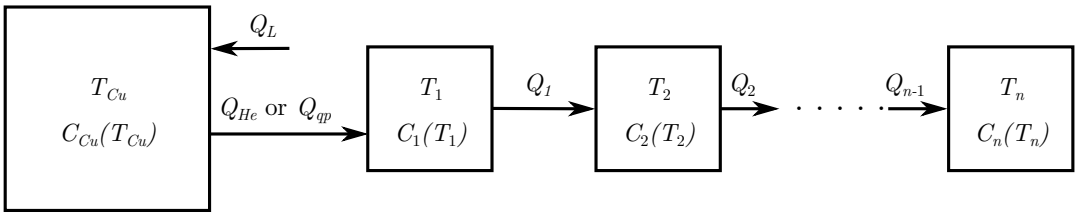

FIGURE 6.2: The block scheme of the aerogel cooldown time calculation.

B^2/T^2, as shown in (2.29). The initial temperature T_{Cui} is indeed the final temperature after demagnetisation of copper.

Since the purpose of this model is only to simply quantify the cooldown time of the whole aerogel sample, we assume that temperature of ^{3}He in copper powder is that of the copper. The real situation is indeed more complicated than that, with Kapitza resistance usually being a significant limiting factor, but for the purpose of this calculation we can neglect it.

The thermal link with the aerogel is governed by the bulk superfluid ^{3}He. In the hydrodynamic limit, the thermal conductance of superfluid ^{3}He is very difficult to estimate as it is essentially two fluid flow with effects such as thermal convection being non-negligible [89]. However, for moderate heat flows the conductance is sufficiently high to be considered near-infinite compared to superfluid ^{3}He in ballistic limit Q_{qp}, derived in Section 2.2.3. For initial temperatures around 800 µK, the exponential term in (2.15) diverges. Therefore the maximum heat flow is set to $Q_{He} = 10^5\,(T_1 - T_{Cu})\,\mathrm{W\,K^{-1}}$. This value ensures the convergence of the calculation while still being large enough to emulate thermal conduction in the hydrodynamic regime.

The aerogel sample is represented by n blocks each at temperature T_n with heat capacity C_{aero}/n connected in series through a thermal link nK_{aero}. The heat capacity C_{aero} is the magnetic field dependent heat capacity of the solid ^{3}He formed on aerogel, modelled and approximated as a two-level system, as derived in Section 2.3. In the presence of an external magnetic field (in our case around 180 mT), the solid ^{3}He heat capacity is much greater than that of the liquid ^{3}He within the aerogel pores or the aerogel itself. The heat conductivity K_{aero} is the thermal conductance of the liquid ^{3}He inside aerogel, previously measured by Fisher et al [40]. For simplicity, we

assume a constant value of $K_{aero} = 1.64 \times 10^{-7}\,\mathrm{W\,K^{-1}}$, and we neglect the conductivity of the aerogel material itself.

Moreover, in the model there is a heat leak Q_L that heats up the copper block at temperature T_{Cu}. This represents a small heat leak from the outer cell to the inner cell, gradually warming up ^{3}He and the copper refrigerant. In reality, the heat leak normally heats up the sample ^{3}He which then heats up the copper, but for our purpose the model simulating direct copper heating is sufficient.

Initially, the temperature of the copper block is set to 100 µK as expected at the end of the first demagnetisation procedure. The initial temperature of aerogel is set to 800 µK. First, all the individual heat flows are calculated using the initial set of block temperatures. Then the temperatures are adjusted according to the heat flow balance on each block. Lastly, the heat capacity of each block is calculated for the new set of temperatures. The process is repeated until the difference between the first and last block is smaller than the tolerance, usually 0.3 µK. The calculated temperature profiles at various times are plotted in Figure 6.3. The time dependence of the temperatures of the first and last block as well as that of the copper block is shown in Figure 6.4. It is clear that in the beginning when heat flow through the ^{3}He is significant, the aerogel cools down quickly and already after 5 hours there is only a slight temperature gradient across the sample. At that point, the conductance of the ^{3}He rapidly drops and the cooldown is much slower. Because the temperature of the first block changes very slowly, the sample has enough time to thermalise and the temperature across it can be considered uniform. Note that at an external magnetic field of 30 mT, the rise of the copper block temperature is minimal during the cooldown even with a heat leak of 10 pW. However, 100 pW would already start to warm up the experiment after 2 days. If such heat leak was present, demagnetisation to higher fields would be necessary to increase the heat capacity of copper and limit the warming.

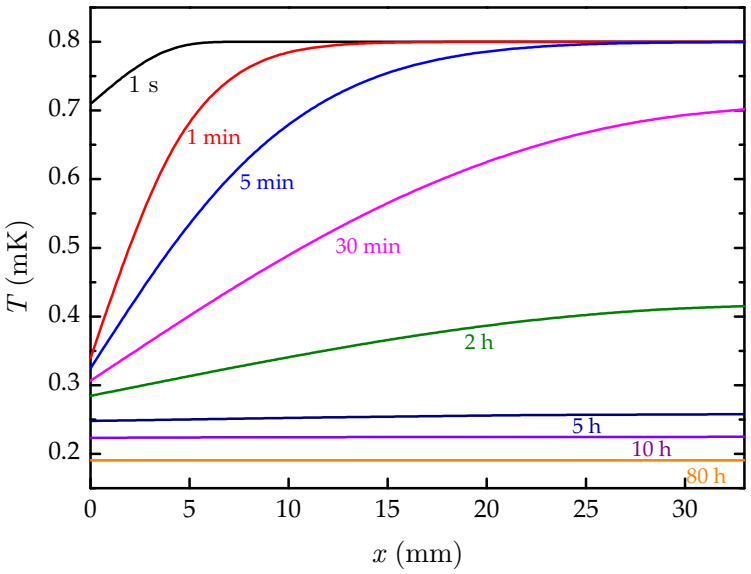

FIGURE 6.3: Temperature profiles of aerogel sample at various times of the cooldown.

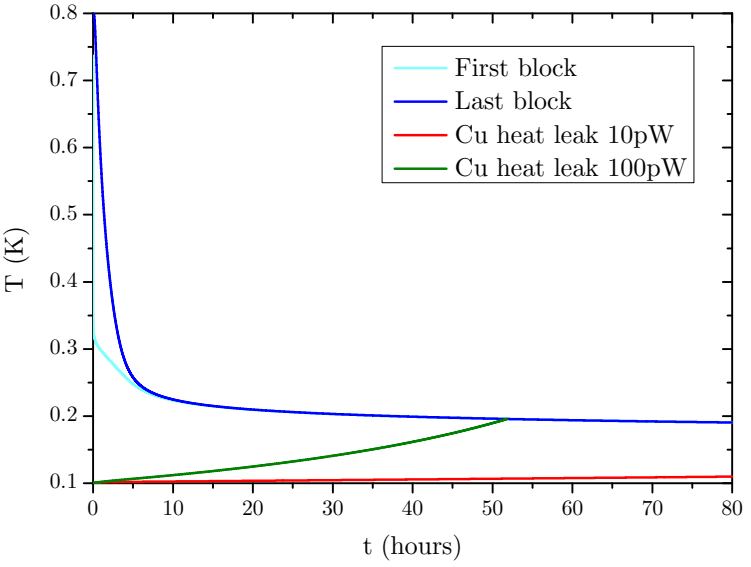

FIGURE 6.4: Temperature development in time for the first calculation block and the last block. The temperature of the copper demagnetisation stage in an external magnetic field of 30 mT for heat leak 10 pW and 100 pW is shown as well. With a heat leak of 100 pW, the experiment starts to warm up after an unacceptable 2 days.

6.4 Superconducting magnetic solenoids

Fine control of the total magnetic field over the copper refrigerant and the experimental region containing the aerogel is required for the proposed experiment. Four superconducting solenoids were designed and constructed.

All magnets were designed to create the desired magnetic field with a current on the order of 1 A, even though they are expected to withstand a few times as much. This gives us the confidence to operate them safely at 1 A and opens the possibility of using higher fields in the future.

6.4.1 Final field NMR magnet

The *NMR magnet* is required to produce a field of $\sim 30\,\mathrm{mT}$ uniformly across the aerogel sample. The same field however must extend to cover the copper area as well. Without this external magnetic field, the copper wouldn't have sufficient heat capacity (see (2.25)) and the cell would quickly warm up due to the parasitic heat leaks. The homogeneity of this magnet is very important to obtain a clear NMR signal, and the deviation across the measured volume should not exceed 0.1 %. The homogeneity was improved beyond that of a simple long solenoid by compensation coils at each end of the coil, which increase the field at the ends. The NMR magnet was inserted over the outer radiation shield (diameter 76 mm) at the temperature of the still of the dilution refrigerator.

6.4.2 Aerogel demagnetisation magnet

Next, a field of $\sim 150\,\mathrm{mT}$ is needed in the area of aerogel sample in order to carry out the second demagnetisation of solid ^{3}He. Naturally, the field should not extend to the region of the copper refrigerant. The *demagnetisation magnet* was thus wound and it slides inside the inner radiation shield attached to the nominal 50 mK shield of the refrigerator.

6.4.3 Field minimum magnet

To vertically trap a magnetic BEC inside the cavity, a sharp dip in the magnetic field intensity is required. This is created by a *field minimum magnet* that slides into the demagnetisation coil former. It is a very small coil with

only 4 layers of 16 turns of superconducting wire. At 1 A, the coil produces a field minimum 1.5 mT deep with curvature of 9 mT cm^{-2}.

6.4.4 Field gradient magnet

Lastly, there is a *gradient magnet* wound on top of the demagnetisation coil to fine tune the NMR field homogeneity and also to make sure that the field minimum is created in the centre of the cavity. It is approximately a Helmholtz coil with two parts of the coil wound in a direction to produce a linear field gradient along the axis. At 1 A the magnetic field difference across the aerogel sample is 1.9 mT.

All field profiles were calculated using a Matlab script written by Roch Schanen. All magnets were optimised to produce maximum field homogeneity and the resulting on axis field profiles are shown in Figure 6.5. Multi-filamentary superconducting wire with copper cladding was used for all the solenoids (Supercon 54S43, outer diameter 178 µm with Formvar insulation). The parameters of the solenoids are summarized in Table 6.2.

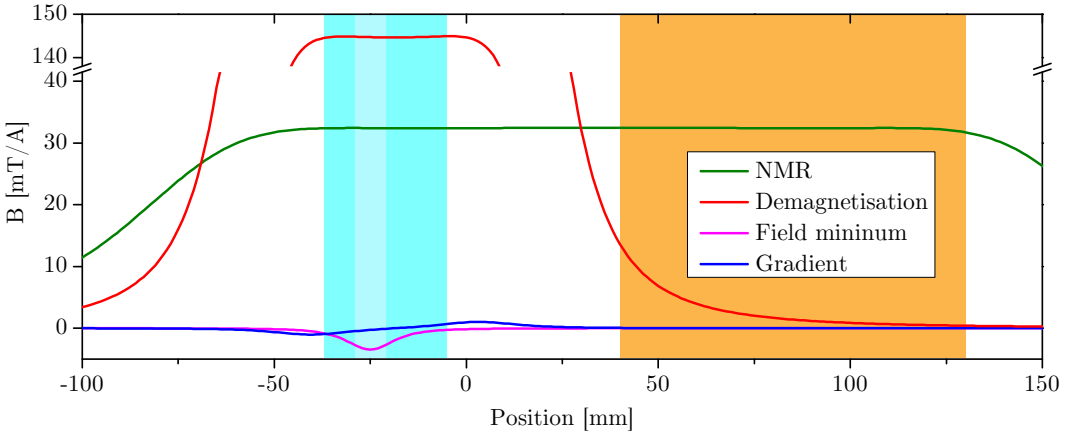

FIGURE 6.5: Calculated on axis field profiles per 1 A of the new superconducting solenoids. The region with the copper demagnetisation stag is shown with orange fill. The aerogel area is shown with blue fill, with the cavity represented by a lighter colour.

TABLE 6.2: Summary of the parameters of the four new superconducting solenoids. The compensation coils are wound at each end of the solenoid on top of the main coil to increase the on-axis field intensity at distances away from the centre of the coil.

		NMR	Demag.	Gradient	Field min.
Main coil	Diameter	78.5 mm	23 mm	30.6 mm	18 mm
	Length	185 mm	48.3 mm	48.3 mm	2.5 mm
	Turns	1299	376	-	13
	Layers	5	23	-	4
Compensation coils	Length	23.2 mm	11.1 mm	5 mm	-
	Turns	130	59	26	-
	Layers	4	14	1	-
	Wire length	1796 m	887 m	5 m	3 m

6.5 NMR setup

The configuration of the NMR measurement is shown with the circuit diagram in Figure 6.6. The circuit operates at the Larmor frequency of ^{3}He atoms: about 1 MHz in an external applied magnetic field of 30 mT. The excitation signal of at this frequency the from primary signal generator is fed through the 1 pF capacitor. The impedance of the capacitor at 1 MHz is much greater than that of the RLC circuit, ensuring constant current in the circuit. The signal then travels down the cryostat through a 1200 pF cold capacitor placed on the mixing chamber plate to the NMR coil around the cell. The other side of the coil is grounded at the mixing chamber. The ^{3}He resonance causes energy to be absorbed by the ^{3}He atoms, resulting in a very slight reduction of the circuit Q factor and the voltage across the tank circuit. As this NMR signal is very small compared to the induced voltage of the tank circuit in the absence of the NMR absorption, it is necessary to remove a large background to improve detection capability. The tank circuit voltage is amplified by a SR560 preamplifier. The amplified signal is then subtracted from the reference coming from the secondary signal generator in the differential amplifier (SR560), ideally leaving only the tiny voltage change caused by the ^{3}He energy absorption. The generators (both Agilent 32500B) are phase-locked together and the phase difference and amplitude

of the secondary signal is adjusted to minimize the sum of both signals. The resulting small signal is then detected by a SR844 high frequency lock-in amplifier.

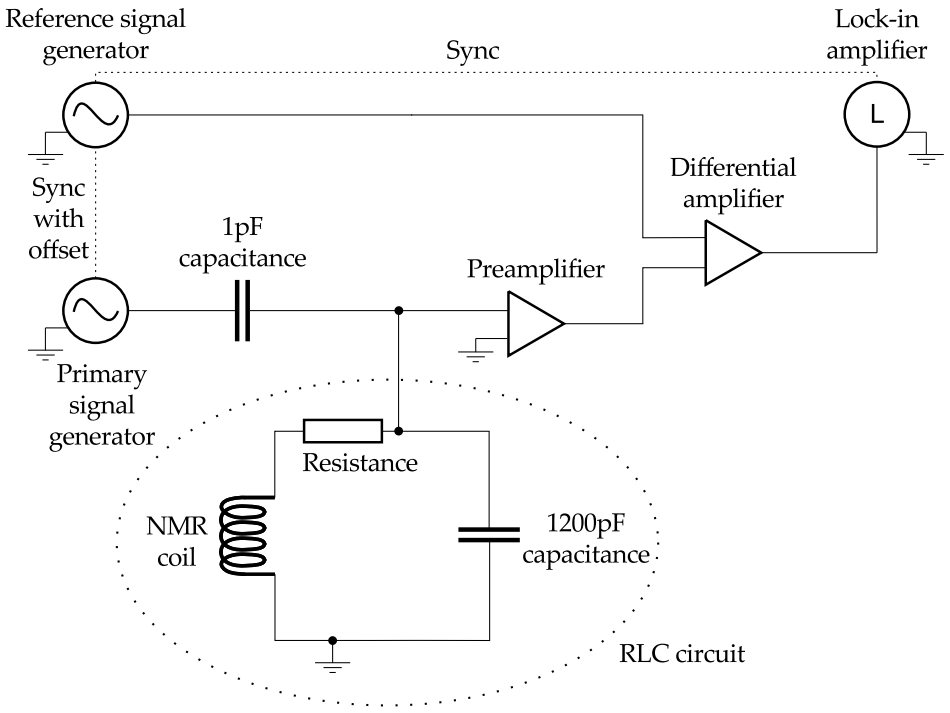

FIGURE 6.6: Electrical circuit diagram of the NMR setup. The AC signal generated by the primary signal generator is fed down the cryostat to the NMR coils. The signal is then amplified by the pre-amplifier and subtracted from the identical reference from another signal generator. The phase shift between the two signal generators is adjusted so that the resulting signal is minimised. Ideally, this subtraction leaves out only the difference between the two signals mostly caused by the ^{3}He absorption.

6.5.1 Quality factor

The *RLC* circuit behaves like a band-pass filter due to resonance - it only passes the frequencies from certain range while rejecting the rest. The bandwidth Δf of such a filter is defined as the difference between the frequencies with transmitted power half of the peak value, similarly to the width at half height Δf_2 shown in Figure 4.1. The Q factor is defined as the ratio of resonant frequency to the bandwidth

$$Q = \frac{f_0}{\Delta f} \,. \tag{6.1}$$

In a parallel RLC circuit with the inductance L and capacitance C where the main loss is the resistance R of the inductor, Q has the form

$$Q = \frac{1}{R}\sqrt{\frac{L}{C}}\,, \tag{6.2}$$

with natural frequency f_0

$$f_0 = \frac{1}{2\pi}\sqrt{\frac{1}{LC}}\,, \tag{6.3}$$

valid for high Q values.

A high Q factor is desired to increase sensitivity of the circuit thanks to greater resonance amplitude. Moreover, higher Q means more selectivity of the circuit only to the studied frequencies around Larmor frequency of solid ^{3}He.

6.5.2 Pickup coils

The design of the pickup saddle coils influences the resonance of the NMR circuit. Over time, the coils were remade to obtain a higher quality factor for the resonance. The two designs, shown in Figure 6.7, are described and compared.

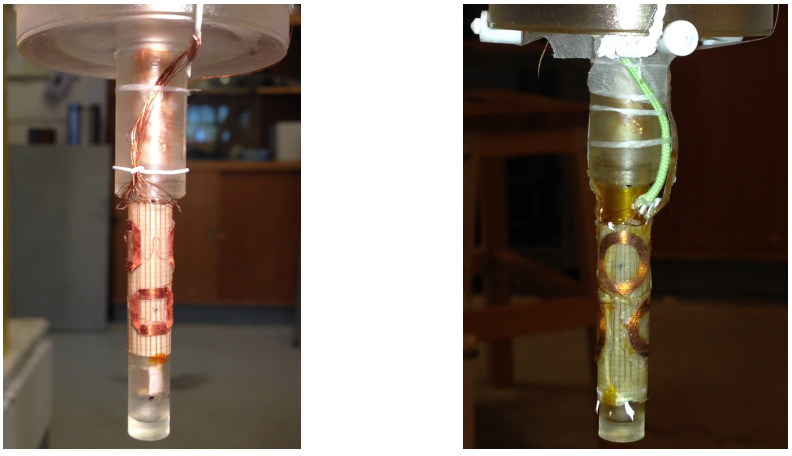

(a) (b)

FIGURE 6.7: Two designs of the NMR saddle coils. (a) initial design using folded square coils, (b) modified design with flat circular coils. The stycast paper tube with copper wires for thermalisation is also visible.

The pickup coils are glued on a cylindrical tube former made of stycast paper that slides onto the outer cell. The tube is thermalised to the mixing chamber via a set of copper wires glued to it. The wires then attach to a single annealed silver wire by crimping with high purity copper plate. The silver wire is thermally anchored to the mixing chamber.

First, the square coils were used due to their simple manufacturing process. Each saddle coil consists of 20 turns of 44 SWG copper wire wound on a teflon former with square cross-section (9 mm $\times$ 9 mm). After applying stycast, the coils were extracted from the teflon former using liquid nitrogen. The coils were then flattened by folding two opposite sides of the square inwards and the other two outwards.

Later, the coils were redesigned in the hope of achieving higher Q factor. To avoid the folds, the square coils were replaced with the circular ones. The coils are created by careful winding of the copper wire on top of double-sided scotch tape in a spiral pattern. Similar to the previous design, the inner diameter of each coil is 8 mm, with 20 turns of 44 SWG copper wire. After winding, a thin cigarette paper was glued onto the coil and once cured, the coil with the paper was carefully peeled off the scotch tape.

Due to the lack of space around the cell, the copper leads of the coils were brought up to the space just below the mixing chamber where they connect to the cryogenic coaxial cables. In the first design, the pairs of leads were twisted together in order to minimise the pickup area. In the second design the leads were glued onto cigarette paper parallel to each other with about 1 mm gap in between. This naturally increases the undesired pickup area of the coil, however it decreases stray capacitance between the wires.

The comparison of the resonances of both coil designs is shown in Figure 6.8. With the new coil design we were able to achieve a Q factor more than 3 times higher.

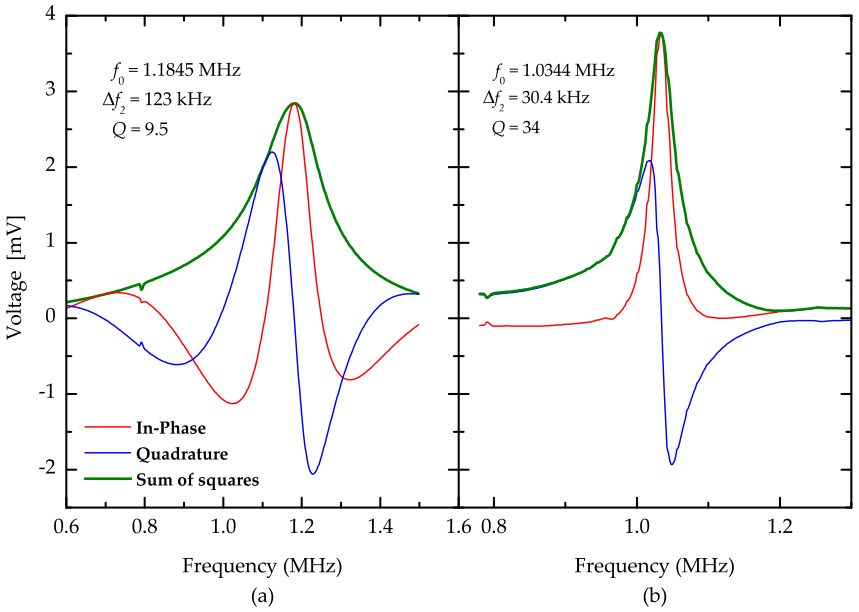

FIGURE 6.8: Frequency sweeps of the NMR coils with (a) old and (b) new design. The mixing of multiple resonances was eliminated with the new design. Moreover, the Q factor more than tripled. The improvements were similar for both of the NMR coils.

6.6 Filling of the cell

The experience of the low temperature group at Northwestern University has shown that the very fine structure of aerogel can crush under the surface tension of ^{3}He during cell filling procedure. Their suggested approach is to fill the cell supercritically, i. e. with ^{3}He safely above the critical point ($T_c = 3.32\,\mathrm{K}$ and $p_c = 1.146\,\mathrm{bar}$ [90]). Once the temperature is lower than T_c, the pressure can be lowered and liquid ^{3}He fills the cell without the creation of a vapour-liquid interface. To ensure that the cell does not explode during the procedure, pressurizing above about 5 bar should be avoided. Unfortunately, estimating the exact cell pressure is difficult. There is a gauge that monitors the cell pressure at the mixing chamber level, but the pressure drop on the thin capillary that connects it with the cell is very hard to predict, especially during cooldown. To roughly estimate the cell pressure, the dependence of resonant frequency and width on pressure was calibrated for both tuning forks inside the cell (TF_{top} and TF_{bot} respectively).

6.6.1 Tuning fork pressure calibration

Using the two-fluid model of superfluid and neglecting the acoustic damping, Blaauwgeers et. al. [59] suggest the frequency dependence on density as follows

$$\left(\frac{f_{0\mathrm{vac}}}{f_0}\right)^2 = 1 + \frac{\rho}{\rho_\mathrm{q}}\left(\beta + \mathrm{B}\frac{S}{V}\sqrt{\frac{\eta}{\pi\rho f_0}}\right) , \tag{6.4}$$

while the dependence of the width Δf_2 is described by

$$\Delta f_2 = \frac{1}{2}\sqrt{\frac{\rho\eta f_0}{\pi}}CS\frac{\left(f_0/f_{0\mathrm{vac}}\right)^2}{m_\mathrm{vac}} , \tag{6.5}$$

where $V = TWL$ and $S = 2(T+W)L$. T,W and L are fork dimensions shown in Figure 4.2. There are three more dimensionless constants β, B and C that depend on the geometry of the fork. $f_{0\mathrm{vac}}$ is the intrinsic frequency - the frequency of the resonator in vacuum without fluid damping. After measuring $f_{0\mathrm{vac}}$, f_0 and Δf_2 for several different densities or temperatures, we can minimize both equations for the parameters β, B and C. Once the parameters are estimated, equations (6.4) and (6.5) can be solved for f_0 and Δf_2 for any pressure and temperature as long as the parameters of the gas are known.

At room temperature, density as a function of pressure and temperature can be conveniently approximated with very good precision by the ideal gas equation

$$\rho = \frac{pM}{TR_\mathrm{spec}} , \tag{6.6}$$

where R_spec is the ideal gas constant and M is the molar mass. However, for the measurements at temperatures around T_c, fitting the data based on literature values is necessary ([91] for ^{4}He and [92, 93] for ^{3}He). The temperature dependence of viscosity can be found in [94, 95].

To find the parameters β, B and C for the tuning forks inside the experimental cell, the cell was cooled down to 4 K and pressurized with ^{3}He to various pressures between 0 and 1.5 bar. The pressure was measured using a capacitance gauge mounted on the mixing chamber plate. To minimise

the pressure gradient in the filling capillary between the cell and the distant gauge, data points were taken after allowing the pressure to equalize overnight.

Since at 4 K it is difficult pump out all ^{3}He after filling the cell, $f_{0\mathrm{vac}}$ was estimated by linear interpolation to 0 bar. Coefficients β, B and C were found and the predicted frequency and width of both tuning forks for a set of pressures in the critical temperature range are shown in Figure 6.9. These plots can then be used a rough guide when estimating the cell pressure during cooldown.

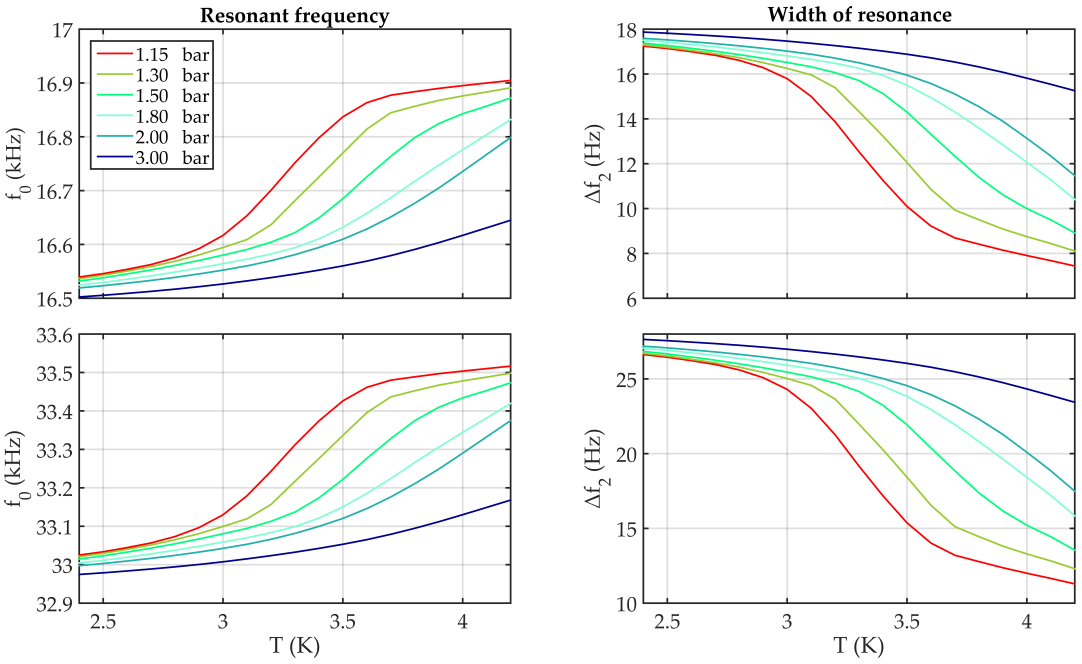

FIGURE 6.9: Calculated f_0 and Δf_2 dependence on temperature for various pressures. f_0 and Δf_2 along the saturated vapour pressure and at fixed density passing the critical point are also shown.

6.6.2 Practical realisation

Standard procedure involves pressurising the cell to around 1.8 bar and keeping the pressure constant as the ^{3}He-^{4}He mixture condenses. The critical point is just above 3 K, so it's important to have the cell pressurized prior to the start-up of the dilution refrigerator. Unfortunately, it turned out that the pressure as measured by the pressure gauge at the mixing chamber

became highly unstable. During multiple cooldowns we encountered numerous situations when the seemingly stable pressure suddenly dropped at astonishing speed, see Figure 6.10. We suspect that the ^{3}He condenses somewhere in the vicinity of the pressure gauge volume which is one of the coldest parts of the refrigerator at the time. The cell with the aerogel sample is indeed warmer than the mixing chamber at this time, but since the exact pressure in the cell is unknown, sudden pressure changes should be avoided nevertheless.

It was thus very important to stay alert during the condensation of the mixture and take immediate action when the cell pressure starts dropping. During condensing one should always keep the high pressure volume full of ^{3}He and immersed in liquid ^{4}He - ready to increase the cell inlet pressure when needed. Often a simple increase in inlet pressure was not sufficient and one had to heat the mixing chamber with the built-in resistor. Using the mixing chamber heater has proven to be the most efficient and sensitive method of raising the ^{3}He pressure, but it slows down the mixture condensation process.

We tried other more desperate ways to increase the ^{3}He pressure as well. For instance one can stop the condensation and fill the 1 K pot with warm ^{4}He gas. Even this quite violent action was sometimes not enough and one had to introduce warm mixture into the still of the dilution fridge. It proved useful to keep the still pressure below about 15 mbar during the condensing process and raise it up to 100 mbar or more only when really needed. The introduction of warm mixture into the still results in immediate warm up and increase in cell pressure, but it slows down the condensation process. It can take more than an hour to pump the still back to 15 mbar in order to start condensing again.

The volume of the cell requires about 50 l of 1 bar room temperature ^{3}He to be condensed. Once the cell was full, no sudden pressure drops would occur and the refrigerator was safe to leave without supervision - condensing the remains of the ^{3}He-^{4}He mixture overnight.

The warmup procedure was similar to the cooldown. One dangerous moment in particular is just after the last remains of the fluid in the mixing chamber boil off. Once all fluid is boiled off, it was necessary to quickly turn off the heater to avoid sudden heating of the evaporated gas. Otherwise the mixing chamber would heat up too quickly and the cell would follow, resulting in a sudden increase in the cell pressure.

Since cooldowns and warmups must be performed with overpressure, it proved to be particularly useful to flush the cell multiple times before every run, decreasing the risk of blocking the filling lines. Partially closed filled lines significantly prolong the warmup procedure which once started must be finished in one session.

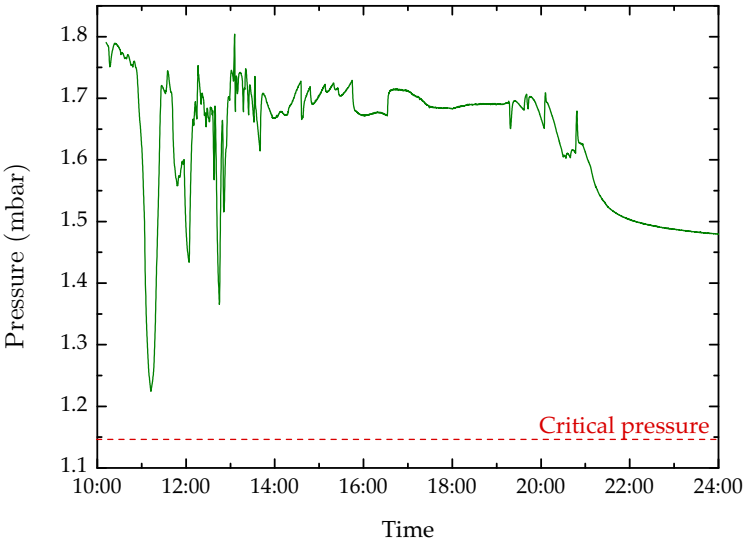

FIGURE 6.10: Cell pressure during the start of the dilution refrigerator as measured by the pressure gauge thermalised at the mixing chamber plate. Sudden drops in the pressure are probably caused by condensation of ^{3}He in the vicinity of the pressure gauge.

6.7 Cooldown problems

6.7.1 Leaks

We encountered numerous leaks in our refrigerator, some more serious than others. First, we discovered a leak to the inner vacuum space of the dewar.

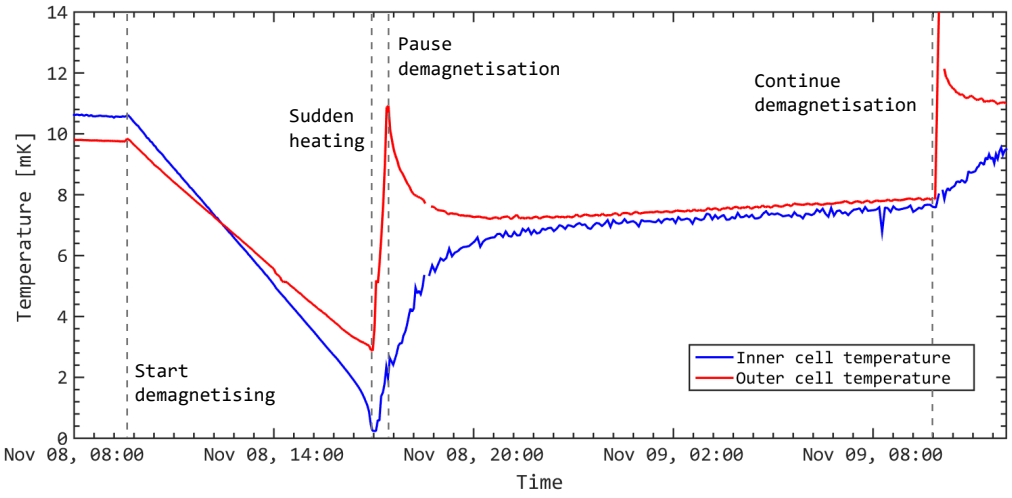

FIGURE 6.11: Temperatures of the inner and outer cell during a typical demagnetisation. Note the sudden onset of temperature rise in the outer cell as well the lack of heating during the pause of the demagnetisation.

The leak was localised on the joint between the plastic neck and the nitrogen shield of the dewar. After a few unsuccessful attempts to repair the leak a new dewar was purchased. Next, a leak into inner vacuum space of the refrigerator was found. The leak was only present at temperatures below around 100 K and was localized at one of the stycast feedthroughs for the coaxial cable (white and black line). The leak was fixed by applying a thin layer of extra Stycast 2850 FT on the feedthrough.

6.7.2 Heating during copper demagnetisation

Unfortunately, during the first attempt to cool down the experimental cell we discovered a large amount of heating into the cell during the copper demagnetisation. The heating is large enough to prevent any attempts for even sustaining superfluid in the inner cell for more than a brief time period. This section summarizes the efforts to diagnose this heating.

A typical demagnetisation procedure is shown in Figure 6.11. In this case, the inner cell was precooled to $\sim$ 11 mK and $B/T_{in} = 0.75\,\mathrm{T\,mK^{-1}}$ before demagnetising. In the beginning it might seem that it all goes well as the temperatures decrease linearly with the magnetic field. The situation changes in a field of about 500 mT when we observe a sudden onset of

heating in the outer cell with the inner cell immediately following. If we pause the demagnetisation, the heating stops and the temperatures relax to a new equilibrium. However, the heating instantly reappears when the demagnetisation is carried on further. Even though this might indicate that the heating appears suddenly at this very specific moment, it seems very unlikely. The heating does not seem to appear at the exactly same magnetic field every time, though it is difficult to judge that. The heating appears at around the superfluid transition where the viscosity of the fluid is very large. The width of resonance of the tantalum vibrating wires is thus very large, resulting in a great uncertainty in the temperature estimation.

Rather than plotting temperatures, it can be more informative to plot the ratio of the magnetic field intensity to temperature as in Figure 6.12. As was shown in Section 3.2, for an ideal adiabatic process with no heat leak the ratio remains constant during demagnetisation and any heat leak into the system causes B/T to decrease. The heat capacity of copper depends on magnetic field as $\propto B^2$, so the heat leak is not very apparent in the initial stages of demagnetisation. As the magnetic field decreases, so does the copper heat capacity and the heat load begins to manifest itself on a significant reduction of B/T ratio, especially in the outer cell.

6.7.3 Possibility of a touch

One of the obvious candidates for causing heating in the outer cell is a touch to the still radiation shield. Due to the necessity of having a small field minimum magnet bore diameter, the radial clearance between the outer cell tail piece and aerogel demagnetisation solenoid is only 2.5 mm. Considering the anchoring points of the two parts are more than 450 mm apart and both parts undergo thermal contractions during cooldown, careful radial alignment of the still shield is necessary. Even then the touch is still a possibility.

We intentionally overheated the still up to 240 mK and observed no change of temperature in the cell. To ensure that the heating warms up the entire magnet former placed at the bottom of the still shield, we glued

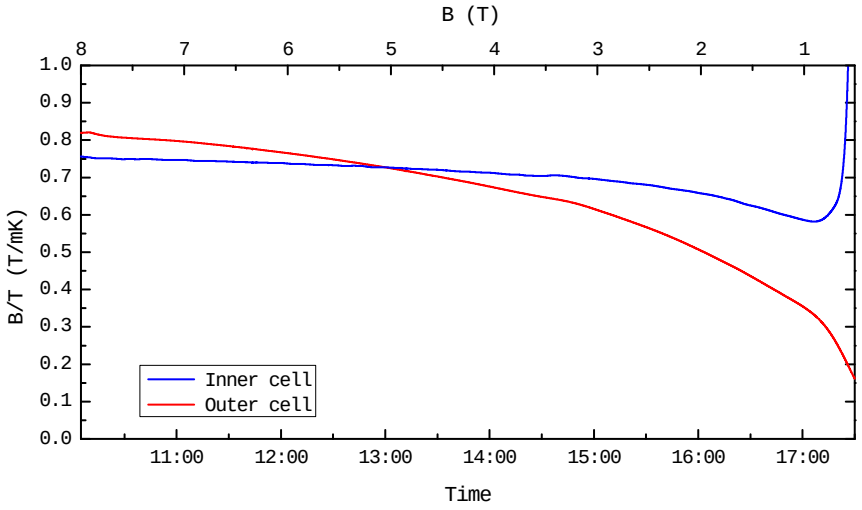

FIGURE 6.12: B/T ratio during demagnetisation. A steady drop in B/T is more pronounced for the outer cell, even though the inner cell eventually follows. The sudden divergence of the ratio is due to reaching the superfluid transition where thermometry is not reliable due to the very large width of the thermometer resonance.

a RuO_2 thermometer on it and observed an increase in temperature during heating.

Moreover, we painted a thin layer of conductive epoxy on the place on the outer cell that would touch first and observed no electric short to the ground of the refrigerator and thus the still shield.

6.7.4 Heat switch emf coil

Another cause of possible heating problems could be incorrect magnetic field in the heat switch region, causing the heat switch to allow a thermal link to the mixing chamber. We wrapped 100 turns of copper wire around the still shield at the height of the heat switch to probe the emf voltage generated by the main magnet field change. One can integrate the emf voltage signal over the entire demagnetisation and obtain a rough estimate of the magnetic field in the region of the coil. By this method we obtained $\sim 88\,\mathrm{mT}$. The magnetic field in the heat switch region should be about 10 % of the full field value, which roughly corresponds to our findings.

6.7.5 Heat switch temperature probes

To learn more about the possible source of heating, three RuO_2 thermometers were glued onto the silver wires leaving the heat switch towards the mixing chamber, the inner and the outer cell. The sensitivity of RuO_2 thermometers at our desired temperature range is very poor and the measurements were thus very crude. In fact, the inner cell thermometer actually turned out to be completely insensitive to any temperature change. Figure 6.13 shows the resistance of the outer cell and mixing chamber resistors together with the resonant width of MCTA vibrating wire. It seems as though the heat switch region experiences the heating immediately when starting the demagnetisation, and the temperature of ^{3}He in mixing chamber eventually follows but this is most likely due to a different process. Heating of the mixing chamber during demagnetisation was always present in many previous experiments at Lancaster and its origin is not clear. One explanation might be that the heat exchangers are slightly magnetic and heat up the incoming ^{3}He to the mixing chamber.

Unfortunately, since the heat switch operates with the fringing field of the main magnet, so it does not allow for switching on and off in arbitrary field. Moreover, there is no clear sign on the tantalum VWR's temperature dependence when the switch closes. For these reasons we tried to test if there is any heat flow through an open heat switch by overheating the mixing chamber at low magnetic field. From Figure 6.14 it is apparent that the temperature of the outer cell follows the mixing chamber temperature immediately - suggesting a leaky heat switch. However, in order to see the temperature change on the RuO_2 thermometers one needs to overheat the mixing chamber significantly (in this case up to 70 mK was measured with MCTA). It is very likely that this overheats the heat switch which causes the heat leak. Under normal conditions, heating to the mixing chamber is much smaller and overheating the heat switch would not be an issue.

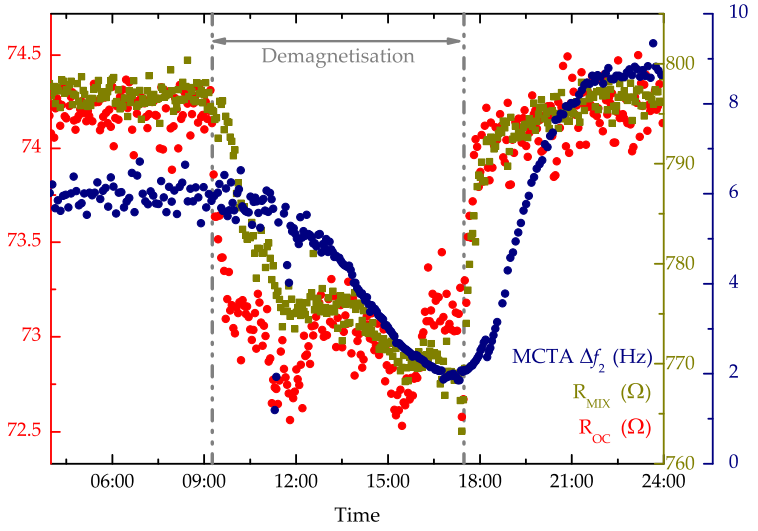

FIGURE 6.13: The response of the RuO_2 thermometers during demagnetisation. The immediate heating of the outer cell thermometer is surprising. Slow heating of the mixing chamber during demagnetisation was typically present with all previous Lancaster demagnetisation experiments, probably due to the heat exchangers being slightly magnetic.

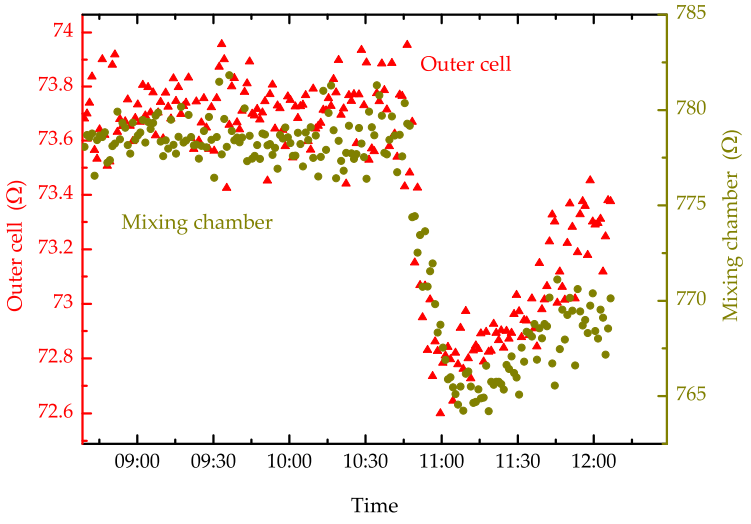

FIGURE 6.14: The response of the RuO_2 thermometers when heating the mixing chamber. The outer cell temperature clearly follows the mixing chamber temperature, suggesting a leaky heat switch. However, this is most likely caused by overheating the heat switch in order to see a temperature change in the mixing chamber with poorly sensitive RuO_2 sensors.

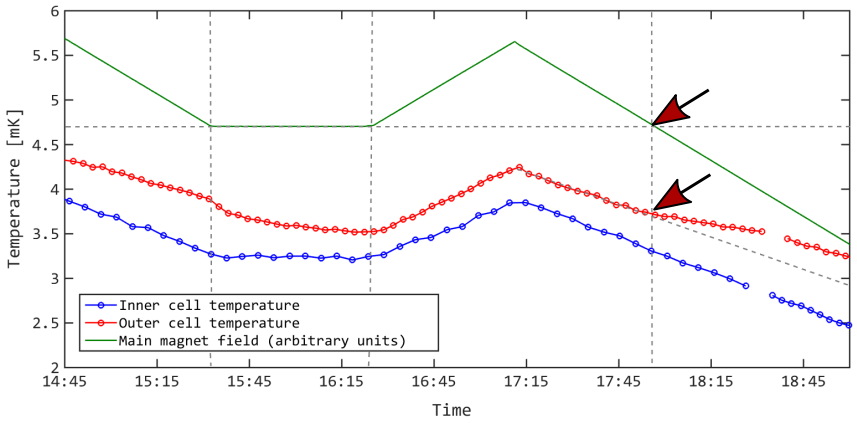

FIGURE 6.15: Temperatures of the inner and outer cell during a typical demagnetisation. Note the sudden change of slope of outer cell temperature when entering a new magnetic field region as well the lack of heating during the pause of demagnetisation.

6.7.6 Hysteretic behaviour

To our surprise, the nature of heating in the outer cell is hysteretic. The heating only occurs when demagnetising to new fields that haven't been previously visited during the demagnetisation procedure. This is illustrated in Figure 6.15. When the cell is demagnetised after slight remagnetisation, no heating is present until entering a new field. Here the slope of the outer cell temperature dependence changes immediately, suggesting heating. The effect of hysteresis remains unexplained and is very likely the cause of our inability to cool the inner cell below 500 µK. A possible explanation for this effect is a magnetic ordering of some material inside the cell. However, this remains a mystery since all materials inside it were used previously in similar designs without any issues.

6.7.7 Leak between inner and outer cell

After many attempts of cooldown, the cell was finally disconnected from the dilution refrigerator and cut open. As we were starting to suspect, we have found a leak between the inner and outer cell at the connection of glass tube to the paper tube, see Figure 6.16. The leak most likely was caused by the large differential contraction between the glass tube and an araldite piece connecting it to the stycast paper tube above it. A solution

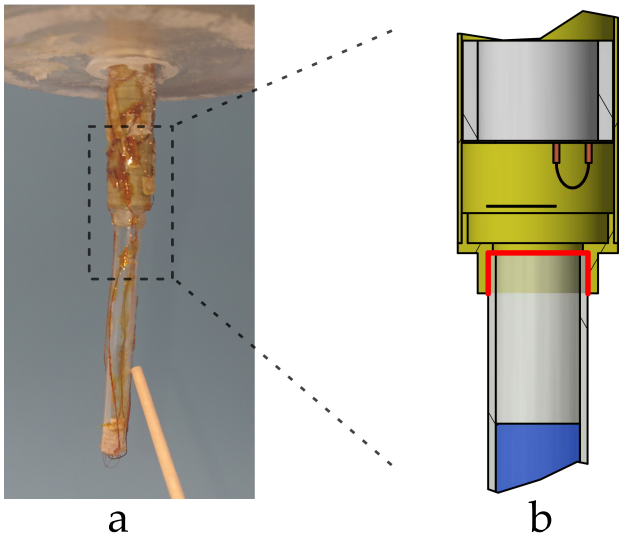

FIGURE 6.16: (a) A broken link between the glass tube and the inner cell is apparent after applying small pressure on the glass tube. (b) Highlighted critical region prone to breaking.

to avoid this in the future work would be to use a connecting piece made of thin stycast paper - a flexible material that can withstand the difference in thermal contraction. The design with an araldite connector was chosen in order to ensure centring and verticality of the glass tube due to tight tolerances and small spacing to the outer cell.

A leak in between the cells is a big problem that would prevent the inner cell from reaching ultra-low temperatures and indeed must be dealt with. However, this issue still does not explain all the symptoms. A leak explains well the quick (within a few hours) equalisation of inner and outer cell temperatures after the demagnetisation is stopped, see Figure 6.11, but the heating during demagnetisation must be caused by another process that is still not clear to us.

6.7.8 Future efforts

The first future step to resolve this issue would probably be to cut away the inner cell, attempt the demagnetisation with just the copper powder and see if the symptoms persist. In the most likely scenario the heating will still be observed, hinting towards unsuitable copper powder or another perhaps ferromagnetic material contaminating the inside of the outer cell. In

such a case then construction of a whole new tailpiece would be inevitable. Unfortunately, recycling the experimental volume of the inner cell would not be feasible due to the tight constraints on the concentricity of the inner and outer cells. In order to meet the required precision, jigging the cell at various parts of the build is necessary. The same building approach would not possible with an already fully finished inner cell.

It is also possible that the problem lies within the inner cell. If the copper demagnetisation stage alone cools down without any issues, the rebuilding of only the experimental volume would be sufficient. Again, we can only speculate what might be the cause of the heating - perhaps an unfortunate choice of the glass tube material?

This chapter has detailed the search effort for the reason for the failure of the demagnetisation stage. As disappointing as the outcome of this search appears to be, the process of building this cell is well documented, making re-building of the apparatus a fairly straightforward procedure. The experiment is still as intriguing as it was in the beginning of this project and the research questions still remain unanswered. There is no doubt that another attempt at solid ^{3}He demagnetisation will follow in the near future.

Chapter 7

Summary

This thesis has presented the latest work on two experiments with superfluid ^{3}He as a medium of interest, at temperatures well below 200 µK in a regime where the thermal excitations are in the ballistic transport limit.

First, the latest developments and results from an experiment utilising a macroscopic superconducting NbTi wire inside the superfluid were described and discussed. This wire, called the Floppy Wire, can be moved through the condensate in oscillatory (AC) as well as, for the very first time within superfluid ^{3}He, in uniform linear motion (DC). The range of velocities covered allows for measurements at speeds exceeding the Landau critical velocity v_L - the velocity at which the the excitation spectrum becomes gapless and quasiparticles can be created at no energy cost. The position of the wire can be monitored and the dissipation caused by the Floppy Wire movement inferred from nearby vibrating wire and quartz tuning fork thermometers. In AC motion the dissipation footprint of the wire movement is in agreement with all other mechanical oscillators studied to date, with a sudden onset of large dissipation when $v_L/3$ is exceeded. However, the situation is very different in the case of DC motion. Here, no large onset of dissipation has been observed up to the highest reachable velocity, more than four times v_L.

We attempted to measure the frequency dependence of dissipation away

from the resonance at 66 Hz and found no difference in the 20–90 Hz frequency range. Below 20 Hz the results are inconclusive, most likely due to strong heating caused by the movement of magnetic flux lines through the superconducting wire. We also studied the dissipation arising from drive pulses with various protocols for the control of wire acceleration. We were able to infer the time constant for the relaxation of surface states - the time required to refill the states that were emptied during acceleration. This time constant is approximately 6 ms and is very weakly temperature dependent in the measured temperature range of 160–230 µK. This weak temperature dependence suggests that the surface states are not refilled from bulk excitations as the number density of these changes greatly across the temperature range. Instead, we posit that the states are refilled via surface flow along the legs of the Floppy Wire from the reservoir of the cell walls.

This finding opens the question of whether the time constant would change for a Floppy Wire with identical resonant frequency but different leg length, and we suggest this as an avenue for future study. Another way to shed more light into the nature of the surface states may be by modifying the surface conditions of the wire, perhaps by using ^{4}He which preferentially plates all the surfaces when introduced into ^{3}He in small quantities. Preplating the Floppy Wire with ^{4}He would change the nature of scattering processes from diffuse to specular and one can speculate how would that influence the surface states relaxation process.

Next, the thesis described our efforts to design, construct and test a new experiment where we attempted to demagnetise the solid ^{3}He layers formed on the surfaces of aerogel. The experiment should allow for reaching sub-100 µK temperatures in superfluid ^{3}He. The experimental setup was built, but unfortunately a large currently unexplained heat leak was discovered during the initial testing. The heating occurs during the demagnetisation of the copper which serves as a precooling stage for the experiment. The thesis described the design of the new experiment, the initial cooldown calculations and the extensive testing undertaken in order to determine the

source of heating. Despite all these efforts, the cause of the heating was not discovered, even after an irreversible post-mortem of the setup. For future work a re-build of the cell is required. The process of construction is well documented, making it a fairly straightforward procedure. The motivation for the experiment remains unchanged and it is anticipated that another attempt will be made shortly.

Bibliography

[1] L.D. Landau. The theory of superfluidity of Helium II. *J. Phys. (USSR)*, **5**:71–90, 1941.

[2] T. Ellis and P. V. E. McClintock. The breakdown of superfluidity in liquid ^{4}He: V. Measurement of the Landau critical velocity for roton creation. *Phil. Trans. R. Soc. (Lond.) A*, **315**(1532):259–300, 1985. doi:10.1098/rsta.1985.0041.

[3] A. I. Ahonen, J. Kokko, O. V. Lounasmaa, M. A. Paalanen, R. C. Richardson, W. Schoepe, and Y. Takano. Mobility of negative ions in superfluid ^{3}He. *Phys. Rev. Lett.*, **37**:511–515, 1976. doi:10.1103/PhysRevLett.37.511.

[4] C. A. M. Castelijns, K. F. Coates, A. M. Guénault, S. G. Mussett, and G.R. Pickett. Landau critical velocity for a macroscopic object moving in superfluid ^{3}He: Evidence for gap suppression at a moving surface. *Phys. Rev. Lett.*, **56**(1):69, 1986. doi:10.1103/PhysRevLett.56.69.

[5] D. I. Bradley, P. Crookston, S. N. Fisher, A. Ganshin, A. M. Guénault, R. P. Haley, M. J. Jackson, G. R. Pickett, R. Schanen, and V. Tsepelin. The damping of a quartz tuning fork in superfluid ^{3}He-B at low temperatures. *J. Low. Temp. Phys.*, **157**(5):476–501, 2009. doi:10.1007/s10909-009-9982-z.

[6] C. J. Lambert. Theory of pair breaking by vibrating macroscopic objects in superfluid ^{3}He. *Physica B*, **178**(1-4):294, 1992. doi:10.1016/0921-4526(92)90208-A.

[7] D. I. Bradley, S. N. Fisher, A. M. Guénault, R. P. Haley, C. R. Lawson, G. R. Pickett, R. Schanen, M. Skyba, V. Tsepelin, and D. E. Zmeev. Breaking the superfluid speed limit in a fermionic condensate. *Nature Physics*, **12**(11):1017–1021, 2016. doi:doi:10.1038/nphys3813.

[8] Y. Okuda and R. Nomura. Surface Andreev bound states of superfluid ^{3}He and Majorana fermions. *J. Phys. Condens. Matter*, **24**(34):343201, 2012. doi:10.1088/0953-8984/24/34/343201.

[9] G. L. Pollack. Kapitza resistance. *Rev. Mod. Phys.*, **41**:48–81, 1969. doi:10.1103/RevModPhys.41.48.

[10] D. I. Bradley. *Copper powder nuclear refrigeration of ^{3}He-^{3}He mixtures*. PhD thesis, Lancaster university, 1983.

[11] F. Pobell. *Matter and Methods at Low Temperatures*. Springer, 2007. ISBN 9783540463603.

[12] D. I. Bradley, S. N. Fisher, A. M. Guénault, R. P. Haley, N. Mulders, G. R. Pickett, D. Potts, P. Skyba, J. Smith, V. Tsepelin, and R. C. V. Whitehead. Magnetic phase transition in a nanonetwork of solid ^{3}He in aerogel. *Phys. Rev. Lett.*, **105**(12):125303, 2010. doi:10.1103/PhysRevLett.105.125303.

[13] K.H. Bennemann and J.B. Ketterson. *Novel Superfluids*, Volume 1 of *International Series of Monographs on Physics*. OUP Oxford, 2013. ISBN 9780191650192.

[14] Gordon Baym and Christopher Pethick. *Landau Fermi-liquid theory: concepts and applications*. John Wiley & Sons, 2008. ISBN 9780471824183.

[15] E. R. Dobbs. *Helium Three*. Oxford University Press, Oxford, 2001. ISBN 9780198506409.

[16] P. W. Anderson and P. Morel. Generalized Bardeen-Cooper-Schrieffer states and the proposed low-temperature phase of liquid ^{3}He. *Phys. Rev.*, **123**:1911–1934, 1961. doi:10.1103/PhysRev.123.1911.

[17] J.R. Schrieffer. *Theory of Superconductivity*. Advanced Book Program Series. Advanced Book Program, Perseus Books, 1983. ISBN 9780738201207.

[18] D. Vollhardt and P. Woelfle. *The Superfluid Phases Of Helium 3*. Taylor & Francis, 1990. ISBN 9780850664126.

[19] T. Guénault. *Basic Superfluids*. Master's Series in Physics and Astronomy. CRC Press, 2003. ISBN 9780203212332.

[20] L. P. Pitaevskii and W. P. Halperin. *Helium Three*. Modern Problems in Condensed Matter Sciences. Elsevier Science, 2012. ISBN 9780444598288.

[21] A.M. Guénault and G.R. Pickett. Liquid ^{3}He at ultralow temperatures: The long mean free path limit. *Physica B+C*, **126**(1):260–266, 1984. doi:10.1016/0378-4363(84)90173-6.

[22] D. Einzel, P. Wölfle, H. Højgaard Jensen, and H. Smith. Quantum-slip effect on the viscosity of superfluid ^{3}He-*B* at very low temperatures. *Phys. Rev. Lett.*, **52**:1705–1708, 1984. doi:10.1103/PhysRevLett.52.1705.

[23] S. N. Fisher, A. M. Guénault, C. J. Kennedy, and G. R. Pickett. Blackbody source and detector of ballistic quasiparticles in ^{3}He-*B*: Emission angle from a wire moving at supercritical velocity. *Phys. Rev. Lett.*, **69**: 1073–1076, 1992. doi:10.1103/PhysRevLett.69.1073.

[24] C. Kittel. *Introduction to Solid State Physics*. Wiley, 2004. ISBN 9780471415268.

[25] A. M. Guénault. *Statistical Physics*, 2nd edition. Springer, 2007. ISBN 9781402059742.

[26] D. T. Sprague, T. M. Haard, J. B. Kycia, M. R. Rand, Y. Lee, P. J. Hamot, and W. P. Halperin. Homogeneous equal-spin pairing superfluid state of ^{3}He in aerogel. *Phys. Rev. Lett.*, **75**(4):661–664, 1995. doi:10.1103/PhysRevLett.75.661.

[27] P. J. Heikkinen. *Magnon Bose-Einstein Condensate as a Probe of Topological Superfluid*. PhD thesis, Aalto University, 2016.

[28] S. N. Fisher, A. M. Guénault, G. R. Pickett, and P. Skyba. A spin laser? The persistent precessing domain in superfluid ^{3}He-B at ultralow temperatures. *Physica B: Condensed Matter*, **329**:80–81, 2003. doi:10.1016/S0921-4526(02)01886-0.

[29] P. J. Heikkinen, S. Autti, V. B. Eltsov, R. P. Haley, and V. V. Zavjalov. Microkelvin thermometry with Bose–Einstein condensates of magnons and applications to studies of the ab interface in superfluid ^{3}he. *J. Low Temp. Phys.*, **175**(5-6):681–705, 2014. doi:10.1007/s10909-014-1173-x.

[30] J. Pollanen, K.R. Shirer, S. Blinstein, J.P. Davis, H. Choi, T.M. Lippman, W.P. Halperin, and L.B. Lurio. Globally anisotropic high porosity silica aerogels. *J. Non-Crystalline Sol.*, **354**(40-41):4668–4674, 2008. doi:10.1016/j.jnoncrysol.2008.05.047.

[31] H. C. Choi, A. J. Gray, C. L. Vicente, J. S. Xia, G. Gervais, W. P. Halperin, N. Mulders, and Y. Lee. A_1 and A_2 transitions in superfluid ^{3}He in 98% porosity aerogel. *Phys. Rev. Lett.*, **93**:145302, 2004. doi:10.1103/PhysRevLett.93.145302.

[32] D.A. Geller, A. Golov, N. Mulders, M.H.W. Chan, and J.M. Parpia. Sound modes of superfluid ^{3}He in aerogel. *J. Low Temp. Phys.*, **113**(3):339–344, 1998. doi:10.1023/A:1022563019975.

[33] B. I. Barker, Y. Lee, L. Polukhina, D. D. Osheroff, L. W. Hrubesh, and J. F. Poco. Observation of a superfluid ^{3}he a-b phase transition in silica aerogel. *Phys. Rev. Lett.*, **85**:2148–2151, 2000. doi:10.1103/PhysRevLett.85.2148.

[34] J. V. Porto and J. M. Parpia. Superfluid ^{3}He in aerogel. *Phys. Rev. Lett.*, **74**(23):4667–4670, 1995. doi:10.1103/PhysRevLett.74.4667.

[35] A. Hasmy, E. Anglaret, M. Foret, J. Pelous, and R. Jullien. Small-angle neutron-scattering investigation of long-range correlations in silica aerogels: Simulations and experiments. *Phys. Rev. B*, **50**:6006–6016, 1994. doi:10.1103/PhysRevB.50.6006.

[36] J. V. Porto and J. M. Parpia. Correlated disorder in a *p*-wave superfluid. *Phys. Rev. B*, **59**(22):14583–14592, 1999. doi:10.1103/PhysRevB.59.14583.

[37] K. Matsumoto, J. V. Porto, L. Pollack, E. N. Smith, T. L. Ho, and J. M. Parpia. Quantum phase transition of ^{3}He in aerogel at a nonzero pressure. *Phys. Rev. Lett.*, **79**:253–256, 1997. doi:10.1103/PhysRevLett.79.253.

[38] E. Nazaretski, G. Lawes, D. M. Lee, N. Mulders, D. Ponarin, and J. M. Parpia. Acoustic spectroscopy of superfluid ^{3}He in aerogel in the presence of a magnetic field. *J. Low. Temp. Phys.*, **126**(1):685–690, 2002. doi:10.1023/A:1013756210150.

[39] H. C. Choi, N. Masuhara, B. H. Moon, P. Bhupathi, M. W. Meisel, Y. Lee, N. Mulders, S. Higashitani, M. Miura, and K. Nagai. Ultrasound attenuation of superfluid ^{3}He in aerogel. *Phys. Rev. Lett.*, **98**:225301, 2007. doi:10.1103/PhysRevLett.98.225301.

[40] S. N. Fisher, A. M. Guénault, N. Mulders, and G. R. Pickett. Thermal conductivity of liquid ^{3}He in aerogel: A gapless superfluid. *Phys. Rev. Lett.*, **91**(10):105303, 2003. doi:10.1103/PhysRevLett.91.105303.

[41] A. Golov, J. V. Porto, and J. M. Parpia. Superfluidity of ^{3}He in aerogel covered with a thick ^{4}He film. *Phys. Rev. Lett.*, **80**(20):4486–4489, 1998. doi:10.1103/PhysRevLett.80.4486.

[42] E. Collin, S. Triqueneaux, Yu. M. Bunkov, and H. Godfrin. Fast-exchange model visualized with ^{3}He confined in aerogel: A fermi liquid in contact with a ferromagnetic solid. *Phys. Rev. B*, **80**(9):094422, 2009. doi:10.1103/PhysRevB.80.094422.

[43] W. P. Halperin, C. N. Archie, F. B. Rasmussen, R. A. Buhrman, and R. C. Richardson. Observation of nuclear magnetic order in solid ^{3}He. *Phys. Rev. Lett.*, **32**:927–930, 1974. doi:10.1103/PhysRevLett.32.927.

[44] N. Gov and E. Polturak. Correlated atomic motion and spin-ordering in bcc ^{3}He. *J. Low Temp. Phys.*, **128**(3):55–85, 2002. doi:10.1023/A:1016347425877.

[45] S. Tasaki. Theory of surface-induced magnetism in adsorbed ^{3}He films. *Prog. Theor. Phys.*, **82**(6):1032, 1989. doi:10.1143/PTP.82.1032.

[46] D. T. Sprague, T. M. Haard, J. B. Kycia, M. R. Rand, Y. Lee, P. J. Hamot, and W. P. Halperin. Homogeneous equal-spin pairing superfluid state of ^{3}He in aerogel. *Phys. Rev. Lett.*, **75**:661–664, 1995. doi:10.1103/PhysRevLett.75.661.

[47] J. Pollanen. *Transverse Pulsed NMR of Superfluid ^{3}He in Aerogel: Unconventional Pairing in the Presence of Quenched Disorder*. PhD thesis, Northwestern University, 2012.

[48] O.V. Lounasmaa. *Experimental Principles and Methods Below 1K*. Academic Press, 1974. ISBN 9780124559509.

[49] G. R. Pickett. Microkelvin physics. *Reports on Progress in Physics*, **51**(10): 1295, 1988. doi:10.1088/0034-4885/51/10/001.

[50] R. H. Salmelin, J. M. Kyynäräinen, M. P. Berglund, and J. P. Pekola. A cryopump-operated rotating nuclear demagnetization cryostat for research on superfluid ^{3}He. *J. Low Temp. Phys.*, **76**(1):83–106, 1989. doi:10.1007/BF00682269.

[51] D.I. Bradley, M.R. Follows, I.E. Miller, R. Oswald, and M. Ward. Simple design for dilution refrigerator with base temperature of 2.3mK. *Cryogenics*, **34**(6):549–550, 1994. doi:10.1016/0011-2275(94)90217-8.

[52] S. A. J. Wiegers, T. Hata, C. C. Kranenburg, P. G. van de Haar, R. Jochemsen, and G. Frossati. Compact $PrNi_5$ nuclear demagnetization cryostat. *Cryogenics*, **30**(9):770–774, 1990. doi:10.1016/0011-2275(90)90274-G.

[53] K. Gloos, P. Smeibidl, C. Kennedy, A. Singsaas, P. Sekowski, R. M. Mueller, and F. Pobell. The Bayreuth nuclear demagnetization refrigerator. *J. Low Temp. Phys.*, **73**(1):101–136, 1988. doi:10.1007/BF00681746.

[54] C. Bäuerle, Yu. M. Bunkov, S. N. Fisher, and H. Godfrin. Temperature scale and heat capacity of superfluid ^{3}He-B in the 100μK range. *Phys. Rev. B*, **57**:14381–14386, 1998. doi:10.1103/PhysRevB.57.14381.

[55] D. I. Bradley, S. N. Fisher, A. Ganshin, A. M. Guénault, R. P. Haley, M. J. Jackson, G. R. Pickett, and V. Tsepelin. The onset of vortex production by a vibrating wire in superfluid ^{3}He-B. *J. Low Temp. Phys.*, **171**(3/4): 582–588, 2013. doi:10.1007/s10909-012-0690-8.

[56] D. I. Bradley, S. N. Fisher, A. M. Guénault, R. P. Haley, G. R. Pickett, D. Potts, and V. Tsepelin. Direct measurement of the energy dissipated by quantum turbulence. *Nature Physics*, **7**:473, 2011. doi:10.1038/nphys1963.

[57] D. I. Bradley, M. Človečko, E. Gažo, and P. Skyba. Probing andreev reflection in superfluid ^{3}He-B using a quartz tuning fork. *J. Low Temp. Phys.*, **152**(5):147–155, 2008. doi:10.1007/s10909-008-9815-5.

[58] M. Človečko, E. Gažo, M. Kupka, M. Skyba, and P. Skyba. High quality tuning forks in superfluid ^{3}He-B below 200μK. *J. Low Temp Phys.*, **162**: 669–677, 2010. doi:10.1007/s10909-010-0330-0.

[59] R. Blaauwgeers, M. Blazkova, M. Clovecko, V. B. Eltsov, R. de Graaf, J. Hosio, M. Krusius, D. Schmoranzer, W. Schoepe, L. Skrbek, P. Skyba, R. E. Solntsev, and D. E. Zmeev. Quartz tuning fork: Thermometer, pressure- and viscometer for helium liquids. *J. Low Temp. Phys.*, **146** (5/6):537–562, 2007. doi:10.1007/s10909-006-9279-4.

[60] R. M. Bowley and J. R. Owers-Bradley. Slip corrections for vibrating wire resonators. *J. Low Temp. Phys.*, **136**(1):15–38, 2004. doi:10.1023/B:JOLT.0000035369.99254.72.

[61] D. I. Bradley, M. Človečko, S. N. Fisher, D. Garg, E. Guise, R. P. Haley, O. Kolosov, G. R. Pickett, V. Tsepelin, D. Schmoranzer, and L. Skrbek. Crossover from hydrodynamic to acoustic drag on quartz tuning forks in normal and superfluid ^{4}He. *Phys. Rev. B*, **85**:014501, 2012. doi:10.1103/PhysRevB.85.014501.

[62] L. D. Landau and E. M. Lifshitz. *Fluid Mechanics*. Pergamon Press, Oxford, 1959. ISBN 9780750627672.

[63] S. N. Fisher, A. M. Guénault, C. J. Kennedy, and G. R. Pickett. Beyond the 2-fluid model - transition from linear behavior to a velocity-independent force on a moving object in ^{3}He-B. *Phys. Rev. Lett.*, **63**: 2566, 1989. doi:10.1103/PhysRevLett.63.2566.

[64] C. Bäuerle, Yu. M. Bunkov, S. N. Fisher, and H. Godfrin. Temperature scale and heat capacity of superfluid ^{3}He-B in the 100μK range. *Phys. Rev. B*, **57**(22):14381–14386, 1998. doi:10.1103/PhysRevB.57.14381.

[65] S. N. Fisher and G. R. Pickett. Quantum turbulence in superfluid ^{3}He at very low temperatures. *Progress in Low Temperature Physics*, **16**:147 – 194, 2009. doi:10.1016/S0079-6417(08)00003-6.

[66] R.W. Johnson. *The Handbook of Fluid Dynamics*. Mechanical engineering. Springer Berlin Heidelberg, 1998. ISBN 9783540646129.

[67] J. P. Carney, A. M. Guénault, G. R. Pickett, and G. F. Spencer. Extreme nonlinear damping by the quasiparticle gas in superfluid ^{3}He-B in the low-temperature limit. *Phys. Rev. Lett.*, **62**:3042–3045, 1989. doi:10.1103/PhysRevLett.62.3042.

[68] A. M. Guénault, V. Keith, C. J. Kennedy, S. G. Mussett, and G. R. Pickett. The mechanical behavior of a vibrating wire in superfluid

^{3}He-B in the ballistic limit. *J. Low Temp. Phys.*, **62**(5):511–523, 1986. doi:10.1007/BF00683408.

[69] I. Berent and E. Polturak. Critical behavior of the shear resistance of solid ^{4}He near a structural phase transition. *Phys. Rev. Lett.*, **81**:846–849, 1998. doi:10.1103/PhysRevLett.81.846.

[70] C. R. Lawson. *A novel measurement device for use in multiphase ^{3}He and ^{4}He at ultra-low temperatures*. PhD thesis, Lancaster university, 2013.

[71] D. I. Bradley, M. Človečko, M. J. Fear, S. N. Fisher, A. M. Guénault, R. P. Haley, C. R. Lawson, G. R. Pickett, R. Schanen, V. Tsepelin, and P. Williams. A new device for studying low or zero frequency mechanical motion at very low temperatures. *J. Low Temp. Phys.*, **165**:114, 2011.

[72] M. Človečko, M. Kupka, P. Skyba, and F. Vavrek. Vacuum properties of high quality value tuning fork in high magnetic field up to 8 Tesla and at mk temperatures. *JPCS*, **568**(3):032006, 2014.

[73] D. E. Zmeev. A method for driving an oscillator at a quasi-uniform velocity. *J. Low Temp. Phys.*, **175**(1):480–485, 2014. doi:10.1007/s10909-013-0942-2.

[74] D. I. Bradley, M. Človecko, M. J. Fear, S. N. Fisher, A. M. Guénault, R. P. Haley, C. R. Lawson, G. R. Pickett, R. Schanen, V. Tsepelin, and P. Williams. A new device for studying low or zero frequency mechanical motion at very low temperatures. *J. Low Temp. Phys.*, **165**(3):114, 2011. doi:10.1007/s10909-011-0388-3.

[75] M. Skyba. *Critical Flow Velocity in Superfluid ^{3}He-B*. PhD thesis, Lancaster university, 2016.

[76] H. Choi, K. Yawata, T. M. Haard, J. P. Davis, G. Gervais, N. Mulders, P. Sharma, J. A. Sauls, and W. P. Halperin. Specific heat

of disordered superfluid ^{3}He. *Phys. Rev. Lett.*, **93**:145301, 2004. doi:10.1103/PhysRevLett.93.145301.

[77] M. Tinkham. *Introduction to Superconductivity: Second Edition*. Dover Books on Physics. Dover Publications, 2004. ISBN 9780486435039.

[78] W. Ruesink, J. P. Harrison, and A. Sachrajda. The vibrating wire viscometer as a magnetic field-independent ^{3}He thermometer. *J. Low Temp. Phys.*, **70**(3):393–411, 1988. doi:10.1007/BF00682788.

[79] M. S. Allen, H. Sumali, and P. C. Penegor. DMCMN: Experimental/analytical evaluation of the effect of tip mass on atomic force microscope cantilever calibration. *J. Dyn. Syst. Meas. Control*, **131**(6):064501, 2009. doi:10.1115/1.4000160.

[80] C. R. Lawson. *A Novel Measurement Device for use in Multiphase Helium-3 and 4 at Ultra-Low Temperatures*. PhD thesis, Lancaster university, 2013.

[81] S. M. Tholen and J. M. Parpia. Hysteretic solidification of surface ^{4}He measured by the modification of the specularity of ^{3}He. *Phys. Rev. Lett.*, **68**:2810–2813, 1992. doi:10.1103/PhysRevLett.68.2810.

[82] D. Kim, M. Nakagawa, O. Ishikawa, T. Hata, T. Kodama, and H. Kojima. Boundary condition on superfluid ^{3}He as altered by ^{4}He interfacial layer. *Phys. Rev. Lett.*, **71**:1581–1584, 1993. doi:10.1103/PhysRevLett.71.1581.

[83] W. Yao, T. A. Knuuttila, K. K. Nummila, J. E. Martikainen, A. S. Oja, and O. V. Lounasmaa. A versatile nuclear demagnetization cryostat for ultralow temperature research. *J. Low Temp. Phys.*, **120**(1):121–150, 2000. doi:10.1023/A:1004665020659.

[84] W. A. Little. Kapitza resistance between helium and metals in the normal and superconducting states. *Phys. Rev.*, **123**:435–441, 1961.

[85] A. C. Mota. A convenient and reliable demountable seal for low temperature work. *Rev. Sci. Instr.*, **42**(10):1541–1542, 1971. doi:10.1063/1.1684935.

[86] D. I. Bradley, S. N. Fisher, A. M. Guénault, R. P. Haley, and G. R. Pickett. Superfluid ^{3}He in the zero-temperature limit. *J. Low Temp. Phys.*, **135** (5):385–397, 2004. doi:10.1023/B:JOLT.0000029503.23955.5f.

[87] D. I. Bradley, A. M. Guénault, V. Keith, C. J. Kennedy, I. E. Miller, S. G. Mussett, G. R. Pickett, and Jr. Pratt, W. P. New methods for nuclear cooling into the microkelvin regime. *J. Low. Temp. Phys.*, **57**(3-4):359–390, 1984. doi:10.1007/BF00681199.

[88] S. Abe and K. Matsumoto. Nuclear demagnetization for ultra-low temperatures. *Cryogenics*, **62**:213 – 220, 2014. doi:10.1016/j.cryogenics.2014.04.004.

[89] J. C. Wheatley. Experimental properties of superfluid ^{3}He. *Rev. Mod. Phys.*, **47**:415–470, 1975. doi:10.1103/RevModPhys.47.415.

[90] S. Velasco, F. L. Román, and J. A. White. ^{3}He vapor pressure near its critical point. *J. Low Temp. Phys.*, **152**(5-6):177–185, 2008. doi:10.1007/s10909-008-9814-6.

[91] A. van Itterbeek, F.W. Schapink, G.J. van den Berg, and H.J.M. van Beek. Measurements of the viscosity of He-gas at liquid helium temperatures as a function of temperature and pressure. *Physica*, **19**(1-12): 1158–1162, 1953. doi:10.1016/S0031-8914(53)80132-1.

[92] Y. Huang, G. Chen, S. Wang, and V. Arp. Equation of state for normal liquid ^{3}He from 0.1 to 3.3 k. *J. Low Temp. Phys.*, **143**(1):1–29, 2006. doi:10.1007/s10909-006-9208-6.

[93] E. R. Grilly. Pressure-volume-temperature relations in liquid and solid ^{3}He. *J. Low Temp. Phys.*, **4**(6):615–635, 1971. doi:10.1007/BF00628297.

[94] P. J. Nacher. Viscosity of gaseous ^{3}He and ^{4}He at low temperatures. *J. Chem. Phys.*, **101**(7):6367–6368, 1994. doi:10.1063/1.468393.

[95] Y. Huang, Q. Yu, Q. Chen, and R. Wang. Viscosity of liquid and gaseous ^{3}He from 3mK to 500K. *Cryogenics*, **52**(10):538–543, 2012. doi:10.1016/j.cryogenics.2012.06.011.